ABSTRACT

DESIGN, ANALYSIS AND OPTIMIZATION OF VISIBLE LIGHT COMMUNICATIONS BASED INDOOR ACCESS SYSTEMS FOR MOBILE AND INTERNET OF THINGS APPLICATIONS

by
Sihua Shao

Demands for indoor broadband wireless access services are expected to outstrip the spectrum capacity in the near-term "spectrum crunch". Deploying additional femtocells to address "spectrum crunch" is cost-inefficient due to the "backhaul challenge" and the exorbitant system maintenance. According to an Alcatel-Lucent report, most mobile Internet access traffic happens indoors. To alleviate the "spectrum crunch" and the "backhaul challenge" problems, visible light communication (VLC) emerges as an attractive candidate for indoor wireless access in the 5G architecture. In particular, VLC utilizes LED or fluorescent lamps to send out imperceptible flickering light that can be captured by a smart phone camera or photodetector. Leveraging power line communication and the available indoor infrastructure, VLC can be utilized with a small one-time cost. VLC also facilitates the great advantage of being able to jointly perform illumination and communications. Integration of VLC into the existing indoor wireless access networks embraces many challenges, such as lack of uplink infrastructure, excessive delay caused by blockage in heterogeneous networks, and overhead of power consumption. In addition, applying VLC to Internet-of-Things (IoT) applications, such as communication and localization, faces the challenges including ultra-low power requirement, limited modulation bandwidth, and heavy computation and sensing at the device end. In this dissertation, to overcome the challenges of VLC, a VLC enhanced

WiFi system is designed by incorporating VLC downlink and WiFi uplink to connect mobile devices to the Internet. To further enhance robustness and throughput, WiFi and VLC are aggregated in parallel by leveraging the bonding technique in Linux operating system. Based on dynamic resource allocation, the delay performance of heterogeneous RF-VLC network is analyzed and evaluated for two different configurations - aggregation and non-aggregation. To mitigate the power consumption overhead of VLC, a problem of minimizing the total power consumption of a general multi-user VLC indoor network while satisfying users traffic demands and maintaining an acceptable level of illumination is formulated. The optimization problem is solved by the efficient column generation algorithm. With ultra-low power consumption, VLC backscatter harvests energy from indoor light sources and transmits optical signals by modulating the reflected light from a reflector. A novel pixelated VLC backscatter is proposed and prototyped to address the limited modulation bandwidth by enabling more advanced modulation scheme than the state-of-the-art on-off keying (OOK) scheme and allowing for the first time orthogonal multiple access. VLC-based indoor access system is also suitable for indoor localization due to its unique properties, such as utilization of existing ubiquitous lighting infrastructure, high location and orientation accuracy, and no interruption to RF-based devices. A novel retroreflector-based visible light localization system is proposed and prototyped to establish an almost zero-delay backward channel using a retroreflector to reflect light back to its source. This system can localize passive IoT devices without requiring computation and heavy sensing (e.g., camera) at the device end.

DESIGN, ANALYSIS AND OPTIMIZATION OF VISIBLE LIGHT COMMUNICATIONS BASED INDOOR ACCESS SYSTEMS FOR MOBILE AND INTERNET OF THINGS APPLICATIONS

by
Sihua Shao

A Dissertation
Submitted to the Faculty of
New Jersey Institute of Technology
in Partial Fulfillment of the Requirements for the Degree of
Doctor of Philosophy in Computer Engineering

Helen and John C. Hartmann Department of
Electrical and Computer Engineering

May 2018

APPROVAL PAGE

DESIGN, ANALYSIS AND OPTIMIZATION OF VISIBLE LIGHT COMMUNICATIONS BASED INDOOR ACCESS SYSTEMS FOR MOBILE AND INTERNET OF THINGS APPLICATIONS

Sihua Shao

Dr. Abdallah Khreishah, Dissertation Advisor — Date
Associate Professor of Electrical and Computer Engineering, NJIT

Dr. Nirwan Ansari, Committee Member — Date
Distinguished Professor of Electrical and Computer Engineering, NJIT

Dr. Roberto Rojas-Cessa, Committee Member — Date
Professor of Electrical and Computer Engineering, NJIT

Dr. Hieu Pham Trung Nguyen, Committee Member — Date
Assistant Professor of Electrical and Computer Engineering, NJIT

Dr. Hany Elgala, Committee Member — Date
Assistant Professor of Electrical and Computer Engineering, SUNY Albany

BIOGRAPHICAL SKETCH

Author: Sihua Shao

Degree: Doctor of Philosophy

Date: May 2018

Undergraduate and Graduate Education:

- Doctor of Philosophy in Computer Engineering,
  New Jersey Institute of Technology, Newark, NJ, 2018
- Master of Science in Electrical Engineering,
  Hong Kong Polytechnic University, Hongkong, China, 2012
- Bachelor of Science in Electrical Engineering,
  South China University of Technology, Guangzhou, China, 2011

Major: Computer Engineering

Presentations and Publications:

S. Shao, A. Khreishah and I. Khalil, "RETRO: Retroreflector based Visible Light Indoor Localization for Real-time Tracking of IoT Devices," *IEEE International Conference on Computer Communications (INFOCOM)*, Honolulu, HI, 2018.

S. Shao, H. Zhang, D. Koutsonikolas and A. Khreishah, "Two-dimensional Reduction of Beam Training Overhead in Crowded 802.11ad based Networks," *IEEE Workshop on Millimeter-Wave Networked Systems (mmSys), co-located with IEEE INFOCOM 2018*, Honolulu, HI, 2018.

Z. Li, S. Shao, A. Khreishah, M. Ayyash, I. Abdalla, H. Elgala, M. B. Rahaim and T. D.C. Little, "Design and Implementation of a Hybrid RF-VLC System with Bandwidth Aggregation," *IEEE International Wireless Communication and Mobile Computing Conference (IWCMC)*, Limassol, Cyprus, 2018.

S. Shao, A. Khreishah and H. Elgala, "Pixelated VLC-backscattering for Self-charging Indoor IoT Devices," *IEEE Photonics Technology Letters*, vol. 29, no. 2, pp. 177-180, 2017.

X. Guo, S. Shao, N. Ansari and A. Khreishah, "Indoor Localization Using Visible Light via Fusion of Multiple Classifiers," *IEEE Photonics Journal*, vol. 9, no. 6, pp. 1-16, 2017.

S. Shao and A. Khreishah, "Delay Analysis of Unsaturated Heterogeneous Omnidirectional-Directional Small Cell Wireless Networks: The Case of RF-VLC Coexistence," *IEEE Transactions on Wireless Communications*, vol. 15, no. 12, pp. 8406-8421, 2016.

S. Shao, A. Khreishah and I. Khalil, "Joint Link Scheduling and Brightness Control for Greening VLC-based Indoor Access Networks," *IEEE/OSA Journal of Optical Communications and Networking (JOCN)*, vol. 8, no. 3, pp. 148-161, 2016.

M. Ayyash, H. Elgala, A. Khreishah, V. Jungnickel, T. D.C. Little, S. Shao, M. Rahaim, D. Schultz, H. Jonas, and F. Ronald, "Coexistence of WiFi and LiFi toward 5G: Concepts, Opportunities, and Challenges," *IEEE Communications Magazine*, vol. 54, no. 2, pp. 64-71, 2016.

S. Shao, A. Khreishah, M. Ayyash, M. B. Rahaim, H. Elgala, V. Jungnickel, D. Schulz and T. D.C. Little, "Design and Analysis of a Visible-light-communication Enhanced WiFi System," *IEEE/OSA Journal of Optical Communications and Networking (JOCN)*, vol. 7, no. 10, pp. 960-973, 2015.

S. Shao, A. Khreishah, M. B. Rahaim, H. Elgala, M. Ayyash, T. D.C. Little, and J. Wu, "An Indoor Hybrid WiFi-VLC Internet Access System," *IEEE International Conference on Mobile Ad Hoc and Sensor Systems (MASS)*, Philadelphia, PA, 2014.

F. Fang, X. Li, S. Li, D. Shen and S. Shao, "Based on Improved PVI Objective Evaluation System of English Sentences," *IEEE International Conference on International Conference on Fuzzy Systems and Knowledge Discovery (FSKD)*, Chongqing, China, 2012.

To my parents, Guoliang Shao and Qingrong Yu; my wife Yu Yang; my aunt Qingzhu Yu; my uncle Xiaohei Wang who always loved me, believed in me, encouraged me, and supported me through everything.

ACKNOWLEDGMENT

First of all, I thank my advisor, Dr. Abdallah Khreishah for his guidance and patience in the last four years. It is been a pleasure working under such a great professor.

I also want to thank Dr. Nirwan Ansari, Dr. Roberto Rojas-Cessa, Dr. Hieu Nguyen and Dr. Hany Elgala for honoring me as members of my dissertation committee. I also thank them for their feedback on this research.

I would also like to thank all the professors who I have collaborated with to realize this research. I would especially like to thank Dr. Michael Rahaim, Dr. Moussa Ayyash and Dr. Thomas Little for the useful discussions I had with them. These discussions opened my eyes on some important things both in life and this research.

Finally, I thank my parents, my wife, my aunt and my uncle for their support and faith in me.

TABLE OF CONTENTS

TABLE OF CONTENTS
(Continued)

Chapter **Page**

TABLE OF CONTENTS
(Continued)

Chapter **Page**

TABLE OF CONTENTS
(Continued)

Chapter **Page**

LIST OF TABLES

LIST OF FIGURES

LIST OF FIGURES
(Continued)

Figure **Page**

LIST OF FIGURES
(Continued)

Figure **Page**

LIST OF FIGURES
(Continued)

Figure **Page**

CHAPTER 1

INTRODUCTION

1.1 VLC-based Indoor Access System for Mobile Device

The continuous growth in the adoption of mobile devices including smart phones, tablets, laptops is driving an insatiable demand for data access to indoor wireless networks. This overwhelming demand is rarely met today – one never complains about having "too much bandwidth" or "too fast service" to the Internet, especially when considering wireless access. Although wireless providers are deploying additional access infrastructure by means of new cells and WiFi end points, the limitation is becoming overuse of existing radio frequency (RF) spectrum. This manifests as contention and interference and results in an increase in latency and a decrease in network throughput – a "spectrum crunch" [1]. To alleviate this problem, new approaches to realize larger potential capacity at the wireless link are needed and optical technologies including visible light communication (VLC) are excellent candidates.

VLC utilizes a light source to send out imperceptible flickering light that can be captured and decoded by a smart phone camera or a photodetector. VLC technology provided with light-emitting diode (LED) devices is characterized by high area spectral efficiency, unlicensed wide bandwidth, high security and dual-use nature [2]. For example, Figure 1.1 shows how VLC can reuse spectrum efficiently in a small area. Case a) shows a WiFi channel in which three users share a 30Mb/s bandwidth, compared to Case b), a VLC-enabled environment, in which three users utilize individual 10Mb/s VLC channels. Although the total bandwidth allocated to the three users are the same in two cases, the

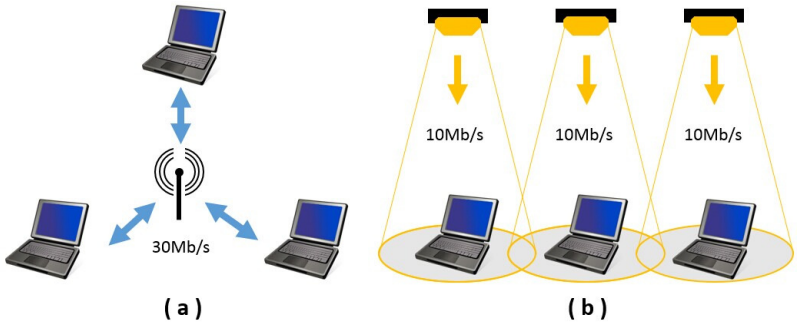

Figure 1.1 Bandwidth density of (a) RF and (b) VLC.

outcome aggregated throughput of Case b) could be better than that of Case a), due to the contention effect on RF channel as we will see later. As a complementary approach to the existing wireless RF solutions, VLC is poised to overcome the crowded radio spectrum in highly-localized systems and become a promising indoor broadband wireless access candidate to resolve the "spectrum crunch".

LED-based indoor VLC has attracted great attention in recent years due to its innate physical properties including energy efficiency and lower operational cost compared to conventional incandescent and fluorescent lighting [3]. Current research on VLC focuses mainly on physical (PHY) layer techniques such as dimming support, flicker mitigation, and advanced modulation schemes [4]. These efforts seek to achieve the possible highest data rates. However, higher-level networking challenges must be addressed to enable interoperability in any practical network deployment [5–8].

Under a dual-use model, VLC is realized by overhead lighting – lights serve to provide lighting and also data access. However, providing an uplink in such a system is challenging due to potential energy limitations of mobile devices (that do not need to produce light for illumination) and potential glare from the produced light. In RF-sensitive and high-security applications, an optical uplink is possible with relatively

high transmission speed [9]. However, in most RF-insensitive places such as homes, schools, offices, and supermarkets, an optical uplink is more difficult to be justified. Mobile devices (e.g., labtops, smart phones, tablets) are energy-constrained. Equipping these devices with a power-hungry light source is impractical. To be efficient, VLC uplinks will need to use narrow beam widths which lead to challenges due to device motion and orientation with respect to fixed uplink receivers. Finally, VLC uplinks can produce glare which is uncomfortable to and undesirable for human users. Thus VLC remains a strong contender for the downlink channel but is better if complemented with an alternative uplink technology.

Alternative heterogeneous schemes, such as VLC and infrared [10], have been investigated by researchers in order to resolve the VLC uplink problem at the PHY layer. However, to make these approaches practical for networking, we still need to address challenges in realizing upper layer protocols when such an asymmetric model is adopted. Moreover, the ubiquitous nature of WiFi with its omnidirectional characteristic can be readily exploited as an uplink, especially if the use of VLC reduces congestion on the RF downlink as a heterogeneous network. Therefore, we propose and implement a hybrid system utilizing VLC as downlink while RF as uplink. This hybrid system can not only alleviate the congestion in conventional RF-based network, but also enable a reliable uplink for VLC system. To further exploit the available bandwidth, we aggregate the WiFi and the VLC channels by implementing an aggregated system. The aggregated system is realized by Linux bonding driver. Experimental results show that the aggregated bandwidth can achieve the addition of WiFi and VLC channels (Chapter 2).

Regarding the bandwidth aggregation, a thorough survey of approaches in heterogeneous wireless networks has been presented in [11]. The challenges and open research issues in the design of bandwidth aggregation system, ranging from MAC layer to application layer, have been investigated in detail. The benefits of bandwidth aggregation includes increased throughput, improved packet delivery, load balancing and seamless connectivity. Considering a system utilizing bandwidth aggregation, *system delay* is a critical quality-of-service (QoS) metric especially for multimedia applications [5]. Here, system delay is defined as the amount of the time from the instant the request arrives at the access point (AP) to the instant that it successfully departs from the access point (AP). We investigate the system delay (Chapter 3) of a heterogeneous system coexisting omnidirectional small cells (OSCs), such as RF femtocells and WiFi WLANs, and directional small cells (DSCs), such as microwave [12], mmwave [13] and optical wireless [14]. Extensive simulations are conducted to indicate that under certain conditions, the system without bandwidth aggregation outperforms the system with bandwidth aggregation in terms of minimum average system delay.

For indoors environment, whenever communication is needed, *lighting is also needed most of the time*. According to [15], energy consumption of lighting represents about 15% of the worlds total energy consumption. Therefore, by jointly performing lighting and Internet access, VLC can operate on a very small energy budget. Optical modulation is performed by varying the forward current of the light source. When a light source is utilized for communication, the increase in total power consumption (including the power consumed by modulator) is mainly due to the switching loss in the driver circuitry at high speed (AC current for modulation). Taking the facts of VLC power

consumption into account, we investigate an optimization problem of minimizing the total power consumption of an indoor multi-user VLC network while satisfying the traffic demands and the illumination requirement (Chapter 4).

1.2 VLC-based Indoor Access System for IoT Devices

It is expected that by 2020, the Internet will consist of 50 billion devices [16], which leads to imperative design of the Internet of Things (IoT). The IoT should be able to link every small object to the Internet and to enable an exchange of data never available before. Compared to the VLC-based indoor access system for mobile devices, several additional challenges need to be resolved to braze the trail for IoT devices. Connecting all these IoT devices to the Internet through wire cable is impractical due to the deployment of wires, complexity added to the small IoT devices, and mobility of the devices. Thus the IoT devices are expected to be connected to Internet via wireless medium. Nevertheless, with the increase in the extremely large amount of wireless access devices, these IoT devices will compete with the users' devices on allocating the spectrum and the "spectrum crunch" [17] problem will be exacerbated if there is no innovative solution to significantly enhance the spectral efficiency. Furthermore, since it is impractical and cost-inefficient to replace the batteries of all these devices or powering them through power cables, self-sustained operation enabled by energy harvesting needs to be tackled. The energy harvested from external sources (e.g., solar power, thermal energy and kinetic energy) is sufficient for the signal generation of the IoT devices [18]. However, what can be harvested by IoT devices (in the order of 100 μWatts) restricts the distance that transmitted signals can travel. Therefore, connecting to cellular networks or even WiFi is not usually a viable

option. This distance constraint results in the requirement of huge infrastructure support, like access points and backhaul links, in order to achieve a small distance reuse factor. Also, trying to achieve such a small reuse factor causes the so-called "backhaul challenge" [19].

One proposed solution to the above challenges is to use RF-backscattering [20, 21]. Small IoT devices harvest energy from the ambient RF signals broadcasted by TV towers [22] or WiFi signals generated by wireless routers, and modulate the reflected RF signals by varying the antenna's impedance, which affects the amount of signal that is reflected by the RF backscatter. While RF-backscattering provides an option for the Internet access of IoT devices, it has several inherent drawbacks. First, the uplink data rate depends on the amount of downlink traffic. For instance, in [20], in order to achieve an uplink data rate of 1 kbps, the WiFi router has to send at a data rate of more than 1.5 Mbps. In [21], it needs the downlink traffic at 24 Mbps in a range of 5 meters, to support the uplink data rate of 1 Mbps. Also, due to the omnidirectional propagation of the RF backscatter signals, interference among the RF backscatters and the uplink data traffic from the users' devices will be inevitable and destructive, especially when the number of IoT devices is large. Furthermore, since the maximum communication distance is short (e.g., 2-5 meters reported in [20, 21]), at least one access point needs to exist within this distance. This fact leads to the expensive infrastructure construction cost. One solution to this problem could be placing a reader [20], such as a mobile phone, within the maximum communication distance, which performs a signal relaying functionality between the access point and the IoT devices. However, this creates additional traffic from the reader, which competes with the mobile traffic and exacerbates the "spectrum crunch". Also, these readers might not

exist all of the time and using mobile phones as readers might cause privacy problem. Another limitation of the RF-backscattering is that we might not be able to use it in a limited RF environment, such as hospital.

Due to the above-mentioned problems, another solution is introduced as the visible light communication (VLC) backscattering [23–26]. The VLC backscatter harvests energy from the existing indoor lighting infrastructure and performs modulation on the reflected light beam as long as the illumination is available. This is motivated by the fact that whenever communication is needed illumination is also needed most of the time. Compared to RF backscatter, VLC backscatter solves the backhaul challenge by utilizing the existing infrastructure with slight modification (i.e., adding driver and photodetector to the light source and utilizing the power line communication or power over Ethernet). Backscattering light beam is also directional, which mitigate the interference problem. VLC backscatter also does not require a reader to relay the uplink data transmission. A shutter modulating the reflected light is proposed in [23] and the corner cube reflector maintaining the directionality of reflected beam is presented in [24, 25]. The state-of-the-art practical work that brings VLC backscatter into the IoT field is [26]. In [26], a VLC backscatter prototype is presented, which uses a solar cell to harvest the optical energy from indoor light sources and modulate the reflected light by a liquid crystal display (LCD) shutter. Nevertheless, no VLC backscatter system can leverage a modulation scheme that is more advanced than on-off keying (OOK). This is because the nonlinearity polarization of LCD shutters. Three types of LCD shutters from Liquid Crystal Technologies [27], named conventional, video and Pi shutters, are evaluated by measuring the transparency with variable input direct current (DC) voltage. As shown in

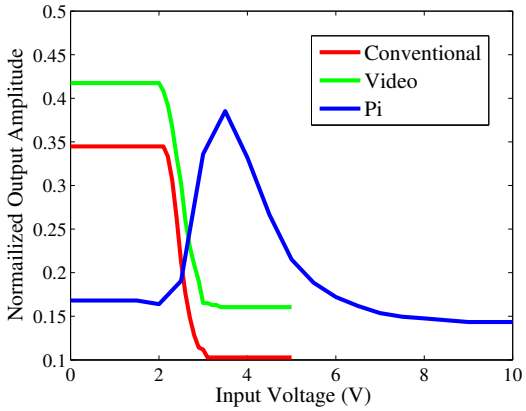

Figure 1.2 The IO curves for three different types of LCD shutters.

Figure 1.2, the output amplitude drops suddenly when the input voltage reaches a certain level. Therefore, applying advanced modulation schemes, such as phase shift keying (PSK), pulse amplitude modulation (PAM), or orthogonal frequency division multiplexing (OFDM), is not available when only one VLC backscatter is used, which is different from the impedance matching approach applied in RF backscatter [21].

To overcome the bandwidth limitation imposed by the non-linearity of LCD shutter, we propose and prototype a novel VLC backscatter, called pixelated VLC backscatter (Chapter 5), which uses multiple smaller reflectors and LCD shutters to form numbers of pixels. Each pixel can switch on or off independently in order to produce multi-level signals. The multi-level signals enable advanced modulation schemes, such as PAM and OFDM. Based on experiments, it is observed that the energy consumption of the pixelated design causes negligible overhead. Based on our testbed, the throughput achieved by the pixelated VLC backscatter is 600 bps at 2 meters, which is highly restricted by the response time of the off-the-shelf LCD shutters (5 ms).

Indoor localization is an important field of application for Internet-of-Things (IoT), for example in warehouses, airports, railway stations, shopping centers, trade fairs,

hospitals, offices and factories. Server-based indoor localization, which is suitable for asset and personal tracking, requires the device to send unique identity information to specific hardware, which can capture the information and forward them to a server to calculate the device's position. Real-time locating system (RTLS) [28] is a typical field of application of server-based indoor localization. RTLS is used to automatically identify and track the location of objects or people in real time.

Visible light communication (VLC) or LiFi can be used as a localization technology [29–34]. LED or fluorescent lamps send out imperceptible flickering light that can be captured by a smart phone camera or photodetector. The information of received optical signal strength, angle-of-arrival, polarization and light distribution patterns can be leveraged for locating light sensing enabled devices. Relying on extensively and homogeneously deployed lighting infrastructure, VLC-based localization approaches only require low-cost additional light source driver [29, 30, 34], or even do not need additional hardware [32, 33]. Thanks to the dominant line-of-sight (LOS) signal and incidence angle sensitive propagation path loss property, VLC-based localization can easily achieve sub-meter accuracy and also detect the orientation of devices [30]. Although VLC-based localization embraces many advantages, the absence of a real-time backward channel from devices to APs restricts the VLC methods to client-based indoor localization, which leads to impractical requirement of computation or heavy sensing (e.g., camera) on small IoT devices. In order to send location and orientation information to the server, additional technology needs to be applied, which results in inevitable latency to real-time tracking as well as unnecessary burden on IoT devices.

To address the above problems, which make conventional VLC-based approaches unsuitable for RTLS of passive IoT devices, we propose and prototype a retroreflector-based visible light localization system (Chapter 6). The novel localization system establishes an almost zero-delay backward channel using a retroreflector to reflect light back to its source. It can locate passive IoT devices without requiring computation and heavy sensing (e.g., camera) at the devices. Multiple photodiodes (i.e., landmarks) are mounted on *any single unmodified* light source to sense the retroreflected optical signal (i.e., location signature). We theoretically derive a closed-form expression for the reflected optical power related to the location and orientation of the retroreflector, and validate the theory by experiments. The characterization of received optical power is applied to a received signal strength indicator and trilateration based localization algorithm. Extensive experiments demonstrate centimeter-level location accuracy and single-digit angular error.

1.3 Dissertation Outline

In this dissertation, we demonstrate the hybrid WiFi-VLC systems design in Chapter 2. The asymmetric hybrid WiFi-VLC system utilize WiFi channel as uplink to resolve the uplink issues of full duplex VLC system. The aggregated hybrid WiFi-VLC system activates both WiFi and VLC duplex channels simultaneously to boost the available bandwidth. In Chapter 3, we further study the system delay of aggregated system and non-aggregated system of heterogeneous RF-VLC system. The simulation results indicate that aggregation might not always be beneficial in terms of the performance of system delay. In Chapter 4, we investigate the power consumption of VLC network by optimizing the power consumption of a multi-user indoor VLC network while satisfying user traffic

demands and illumination requirement. The optimization problem is resolved by the efficient column generation method. We propose a novel pixelated VLC backscatter in Chapter 5, which enables advanced modulation scheme, such as PAM and OFDM, and allows the first time orthogonal multiple access. We also present our designed prototype of the novel pixelated VLC backscatter based on M-PAM and its performance in terms of throughput and power consumption evaluated by experiments. In Chapter 6, we propose and prototype a novel retroreflector-based visible light localization system, which can locate passive IoT device using any unmodified light infrastructure without requiring computation and heavy sensing (e.g., camera) at the devices. The dissertation is finally summarized in Chapter 7.

CHAPTER 2

DESIGN AND ANALYSIS OF A VLC ENHANCED WIFI SYSTEM

2.1 Introduction

In this chapter[1], we propose and implement a practical hybrid system comprised of typical IEEE 802.11 a/b/g/n technology and a VLC link, in which the unidirectional VLC channel is exploited to supplement the conventional downlink RF channel. Such a system was proposed and theoretically examined in [5]. Figure 2.1 shows the basic configuration of this heterogeneous network. Such a system not only alleviates congestion caused by WiFi access contention, but also resolves the potential problems of uplink transmission in VLC networking. For more information and also the videos of experiments, please refer to our website[2].

To further exploit the potential available resources of WiFi and VLC, we extend our investigation to the aggregation of multiple wireless interfaces. Although the hybrid solution alleviates congestion at the WiFi access point, the maximum achievable download data rate of this system is still limited by the single VLC link. In environments where VLC hotspots are deployed pervasively, we aim to utilize any available RF resources to supplement VLC links and provide additional capacity to devices requiring higher throughput. Referring to [11], we can benefit from the bandwidth aggregation for not only the improved throughput, but also the reliable packet delivery, load balancing and low cost capacity increase. It is also shown that many efforts have been spent on the

[1]The work of this chapter has been published in [35]
[2]http://web.njit.edu/∼abdallah/VLC/ (accessed 1-May-2014).

bandwidth aggregation at different layers of the network protocol stack. Since our main objective is to implement the aggregation with modification to the clients only without affecting the server part, we focus our attention on the data link layer aggregation.

We utilize link aggregation through the use of two full-duplex wireless connections. Both the bi-directional WiFi and VLC links are fully utilized to improve the achievable throughput and provide a more robust network connectivity. Figure 2.2 depicts the aggregated network. With combining multiple wireless access technologies, the system takes the advantages of both communication techniques. We mathematically prove the superiority of aggregated system with respect to the minimum average system delay. With optimal traffic allocation between WiFi and VLC, the aggregated system provides a lower minimum average system delay than another system that allocates each request to either WiFi or VLC.

The main contributions are the following:

- The design and implementation of an asymmetric system comprised of WiFi uplink and VLC downlink to increase overall network capacity with multiple users.
- The design and implementation of an aggregated system that simultaneously activates both WiFi and VLC connections providing high throughput and more reliable data transmission.
- Theoretical analysis that prove the superiority of the aggregated system over the non-aggregated system in terms of minimum average system delay.
- Analysis and real experimentation on our testbed to evaluate the network performance of two different systems under interactive web browser traffic and TCP throughput with different levels of congestion.

2.2 System Model

In this section, we illustrate the models of two heterogeneous systems: i) Hybrid WiFi-VLC system (Figure 2.3); ii) Aggregated WiFi-VLC system (Figure 2.4).

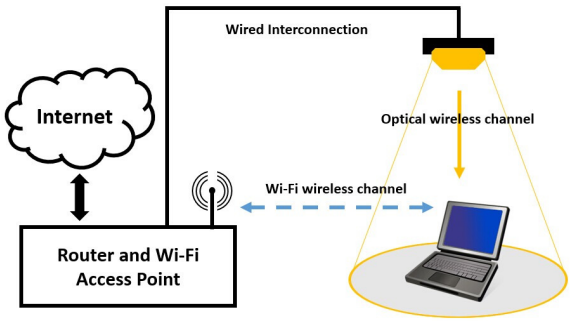

Figure 2.1 Proposed hybrid WiFi and VLC network model.

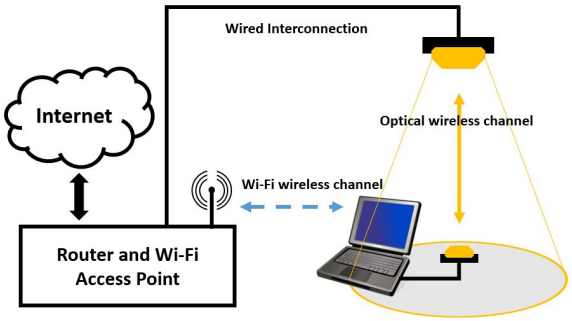

Figure 2.2 Proposed aggregated WiFi and VLC network model.

2.2.1 Hybrid System

Challenges: The primary challenges of designing an asymmetric system are as follows:

1) Typically, uplink and downlink data streams based on WiFi connection between the client and the server flow through the same routing path. In order to redirect the data flow downloaded from the server to the client to the VLC hotspot, an intermediate coordinator is needed to break the conventional downlink data delivery and forward the data packets to the VLC hotspot. However, this process may generate inevitable redundancy due to the need of extra devices to perform data redirection. In Figure 2.3, we aim to assign the infrastructural router as the redirecting node, forwarding downlink traffic to PC I and simultaneously providing PC II with an uplink wireless access point.

2) A typical small office home office (SOHO) wireless router has one wide area network (WAN) port and multiple local network (LAN) Ethernet ports. Terminals

Table 2.1 An Example of Static Routing Table

Dst IP	Subnet Mask	Next hop	Metric
192.168.1.100	255.255.255.255	192.168.1.200	2

connected to the router through either wired or wireless links belong to the same sub-network. This router serves as an edge router with a gateway IP address. Intuitively, we might be able to activate the routing function on PC I in Figure 2.3, in order to directly forward the data packets from the router to PC II. However, due to the OS kernel built-redirecting function, the simple forwarding method based on the routing function may not be useful. Since the destination IP address of the data packets that arrive at the network interface card (NIC) A-1 is actually the IP address of NIC B-1, the packets will be redirected back to PC II through the router instead of the VLC link, if the forwarding function of PC I is activated.

3) In a typical TCP connection, the client initiates a three-phase handshake process with the server. According to the OSI model, the client first generates a SYN data segment at the application layer. After that, the data segment is encapsulated with IP headers at the network layer before being sent out through the NIC. Since the client starts listening to the socket with the same TCP port and IP address as that used during encapsulation, the following problem occurs. If the packets from the server are received from a different NIC with different socket information, they may not be selected by the application that initiated the TCP connection. In Figure 2.3, the requests are transmitted through NIC B-1 while the responses are received from NIC B-2. The above problem is encountered in the asymmetric system in Figure 2.3.

System Design: Figure 2.3 demonstrates the hybrid system model for indoor Internet access. The system consists of a downlink VLC channel and an uplink WiFi

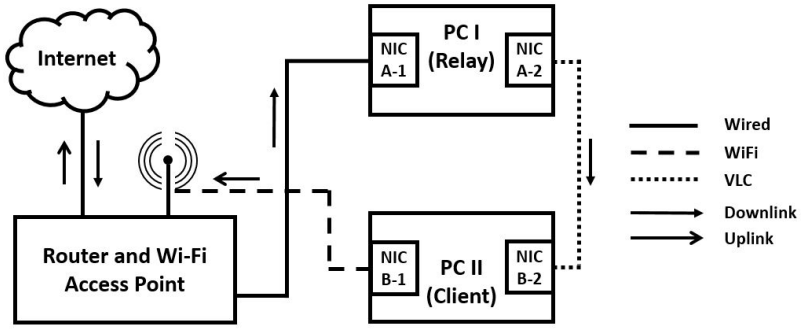

Figure 2.3 Hybrid system architecture.

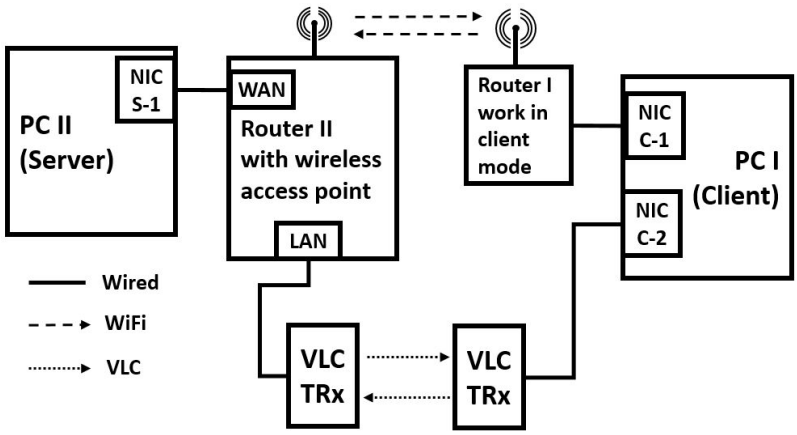

Figure 2.4 Aggregated system architecture.

channel. To resolve the challenges mentioned earlier, three procedures (each one of these procedures corresponds to one of the above challenges) need to be performed as follows:

1) To address the problem mentioned in the first challenge, a static routing table is enabled at the router. Rather than dynamically forwarding IP packets as normal, the router follows a manually-configured routing entry with three items: i) destination IP address, ii) subnet mask, and iii) next-hop router IP address. Table 2.1 shows an example of routing IP traffic destined for the 192.168.1.100/24 via the next-hop router with the IPv4 address of 192.168.1.200/24. In the proposed hybrid system, one active static routing rule redirects IP packets destined for NIC B-1 to NIC A-1 instead.

Algorithm 1 Pseudo Code of Socket Program

```
Require:
    Define BufferSize MTU;
    Set socket s for frames capture;
    Set socket d for frames retransmission;
    Bind socket s to NIC A-1;
    Bind socket d to NIC A-2;
Ensure:
 1: while 1 do
 2:    Receive frames from socket s and store into buffer msg[BufferSize];
 3:    if frame length > MTU then
 4:       Continue;
 5:    if frame desitination IP addr = IP B-1 then
 6:       Change dest MAC addr to MAC B-2;
 7:       Change src MAC addr to MAC A-2;
 8:       Change dest IP addr to IP B-2;
 9:       Compute IP checksum;
10:       Compute TCP checksum;
11:       Compute UDP checksum;
12:       Send modified frames to socket d;
```

2) After successfully arriving at the relay node (PC I), server IP packets need to be further forwarded to the client through NIC A-2. In the Linux OS, the IP packet forwarding function is enabled by changing the value of *ip_forward* under the path "/proc/sys/net/ipv4/ip_forward" from 0 to 1. As mentioned in the challenge (2) earlier, if we activate the forwarding function on PC I, the arrived IP packets will be redirected back to PC II through NIC A-1 instead of NIC A-2. Therefore, we must set the value of *ip_forward* to 0. Rather than relying on the forwarding function, we utilize the socket programming based on $SOCK\_PACKET$ type [36].

The $SOCK\_PACKET$ mechanism in Linux is used to take complete control of the Ethernet interfaces. Due to the capability of capturing frames from the data link layer and placing a pointer which points to the first byte of each frame (the first byte of MAC header), $SOCK\_PACKET$ is suitable for MAC frames capturing and retransmission. Algorithm 1 represents the relaying functionality. In the algorithm, we first define the buffer size according to the maximum transmission unit (MTU) which is a default value

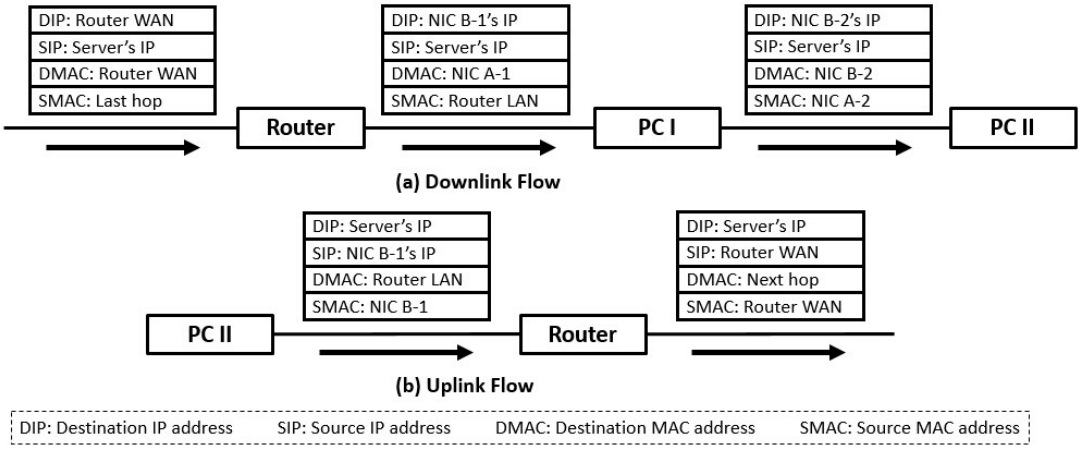

Figure 2.5 Flow of MAC and IP headers of packets between server and client, a) downlink flow and b) uplink flow.

in the router. Then two sockets of the $SOCK\_PACKET$ type are created and bound to NIC A-1 and NIC A-2. After the initialization phase of key parameters, the iteration phase, which includes receiving, processing and retransmission, is started. To avoid the alert of no buffer space available for the sending function, the received frame length needs to be checked. If the length is larger than the defined MTU, the frame must be discarded. Also, the destination IP address of the captured frames for efficient relaying is checked. If it is the same as the IP address of NIC B-1, we manually modify packet's MAC and destination IP address. To realize the Internet access, the checksums of IP, TCP and UDP need to be recomputed before sending the packets to the client. This is because the checksum computation includes the destination IP address.

3) As it is mentioned in challenge (3) earlier, the application that initiates the TCP connection to the server will listen to the socket with the IP address of NIC B-1 but not NIC B-2. The OS kernel will not do any action on the packets although they are not filtered by the NIC. A possible solution is changing the destination IP of the packets to the IP address of NIC B-1. However, due to the fact that the destination IP address of

the packets is not that of the port they are received from, the packets should be forwarded based on the routing table. To overcome this difficulty, an approach called "operating system spoofing" is proposed.

Operating System Spoofing: The basic idea of this approach is to manually make the OS listen to NIC B-2 while transmitting out the packets through NIC B-1. Assume that the IP addresses of NIC B-2 is 192.168.2.100/24 and the default gateway of PC II is 192.168.1.1/24. The default gateway is deleted and a new one within the subnet 192.168.2.0/24 (e.g., 192.168.2.1/24) is added. In addition, an entry in the ARP table on PC II (e.g., arp -s 192.168.2.1 ab:ab:ab:ab:ab:ab) is added. When these two steps are completed, PC II will believe that there is a next-hop gateway connected to NIC B-2 even though this gateway does not exist. With the ARP spoofing, all packets generated at the application layer on PC II are forwarded to NIC B-2 and stop there because of the physical layer blocking. The most significant point at this moment is that the applications are listening to the socket with the IP address of NIC B-2.

After the configuration of the routing and ARP tables, a socket program, that implements packets copying, headers modification and retransmission, is run. Similar to the program run on PC I, the socket of type $SOCK\_PACKET$ is used to capture the packets flowing through the device driver layer of NIC B-2. With the returned pointer, the source IP and MAC addresses of the copied packets to the IP and MAC addresses of NIC A-1 are altered. Also, we change the destination MAC address to router's LAN MAC address. The checksums of IP, TCP and UDP need to be recomputed. After all the modifications of the IP and MAC headers are completed, the packets are sent to the router through NIC B-1. From the router's point of view, the client's IP is the IP address

of NIC B-1. However, from the client's point of view, it connects to the Internet with the IP address of NIC B-2. Figure 2.5 reveals the variation of IP and MAC headers.

Note that, compared to the previously published work [37], the achievable network throughput of the proposed hybrid system has been enhanced. For the packets captured on PC II, a selective condition before sending them to the router is added. Only the packets with a source IP same as the IP address of NIC B-2 are processed by the program. Since the capture function returns the packets not only in the transmitting buffer of NIC B-2 but also in the receiving buffer, the added condition saves half of the redundant processing time in the unmodified program.

2.2.2 Aggregated System

Figure 2.4 demonstrates the link aggregation system model including the full-duplex WiFi and VLC connections. Since the bonding driver provided by Linux operating system is only capable of aggregating Ethernet interfaces, both NIC C-1 and NIC C-2 of PC I (client) are Ethernet cards. The wireless Router I working in client mode, is connected to PC I through Ethernet cable and connected to Router II through bi-directional WiFi link. The other network connection between the PC I and the Router II is a bi-directional VLC link, which is established by two VLC transceivers. The bi-directional VLC link will be described in Section 2.4. The two NICs on PC I are in the same subnet and the IP address of Router II LAN is used as the IP address of the gateway of PC I, when the aggregation configuration is not enabled. On the right side, PC II (server) is connected to the WAN port of Router II. Thus Router II acts as an intermediate node between two different networks.

To implement the data link layer aggregation, we utilize the Linux Ethernet bond driver [38]. The driver provides a method to aggregate multiple Ethernet interfaces into a single logical "bond" interface. The behavior of the artificial interface depends on the selected mode. There are seven modes in bonding configuration: 0) Balance-rr; 1) Active-backup; 2) Balance-xor; 3) Broadcast; 4) 802.3ad; 5) Balance-tlb; 6) Balance-alb. Modes 0, 2 and 4 require extra switch support, which conflict with our objective of not having extra devices. Under Mode 1, only one slave in the bond is active. The other slave becomes active if and only if the active slave fails. Thus, the maximum throughput that can be achieved in this mode can not exceed the highest one of the slaves. In Mode 3, the same packets are sent through all slave interfaces, in order to provide fault tolerance. Therefore, only Mode 5 and Mode 6 are left to choose from. For the goal of achieving higher aggregated throughput without any modification to the server side or even to the next hop of the client, Mode 6 is the best option.

Mode 6 (adaptive load balancing) contains Mode 5 (adaptive transmit load balancing). Also, Mode 6 integrates the receive load balancing for the IPv4 traffic and does not require any switch support. Load balancing at the receiver is achieved by ARP negotiation. The bond driver intercepts the ARP response sent from the host and changes the source MAC address to the unique MAC address of one of the slaves. It enables the peers to use a different MAC address for communication. Typically, all the slave ports will receive the broadcast ARP requests from the router. The bond driver module intercepts all the ARP responses sent from the client, and computes the corresponding port that the client expects to receive data from. Then the driver modifies the source MAC address of the ARP response to the MAC address of the corresponding port. The destination MAC address is

kept the same as the MAC address of the router LAN. Note that each port can send the ARP response not only with its own MAC address but also with the MAC address of the other slave port. The received data traffic can be load balanced in either way. When the client sends the ARP request, bonding driver copies and saves the IP information of the router. When the ARP reply from the router arrives, the bond driver extracts the MAC address of the router and sends an ARP response to one of the slave ports (this process is the same as the received load balancing process mentioned above). One potential problem in ARP negotiation is that when the client sends out the ARP request, it uses the MAC address of the logic bonding interface. Thus, after the router learns this MAC address, the downlink traffic from the server flows through the corresponding slave port which may not be the intended one. This problem can be addressed by sending the updated ARP response. The client sends the ARP responses to all slave ports and each response contains the unique MAC address of each slave port. Thus, the downlink traffic from the server are redistributed. The receive load [38] is allocated orderly from the slave with widest bandwidth.

In Figure 2.4, when Router II broadcasts the ARP request to PC I, PC I typically sends back an ARP response with the bonding MAC address and the bonding IP address. However, under the adaptive load balancing mode, the bonding driver intercepts the APR response and changes the source MAC address to that of one of the slaves (e.g., NIC C-1). Thus, when the router receives the ARP response, it refreshes its ARP cache with a new entry (Bond IP: NIC C-1 MAC). To increase the total bandwidth of the client, PC I sends back the ARP response with the NIC C-2 MAC address when the capacity of NIC C-1

is exhausted. After receiving the new ARP response, the router updates its ARP cache (Bond IP: NIC C-2 MAC).

2.2.3 Analysis

"Spectrum crunch" [1] is a challenging problem in WiFi networks. Due to the limited bandwidth, although the efficiency of the spectrum utilization has been highly improved, the degradation of network throughput caused by the growing number of WiFi users and other devices operating in the 2.4 and 5 GHz bands is still inevitable. Also, the network delay could be much larger when the number of users in the same WiFi access point increases. Because of the CSMA/CA mechanism defined in 802.11 standards [39], the average back-off time is unavoidably increased when there exists more mobile users located in the same WiFi coverage. To circumvent these unexpected user experiences, the hybrid WiFi-VLC system is presented. Although the uplink WiFi may be in contention with other WiFi users, the downlink VLC is an independent data communication channel from the WiFi channels. In our daily life, downloading happens much more frequently than uploading; hence having an undisturbed VLC download channel may provide a satisfactory Internet surfing experience. Regarding the increasing demand for downlink bandwidth, the hybrid VLC user does not need to compete with other WiFi users for the RF spectrum. Therefore, the network delay will be reduced.

In some specific scenarios where the uplink VLC is allowable, aggregating both bi-directional WiFi and VLC links can provide more available bandwidth. Taking the shortages of VLC into account, the aggregated system is more robust than the hybrid one. As the distance between the front-ends of WiFi and VLC is increasing or the channel

blocking duration is increasing, the performance of VLC channel may drop quickly. However, these two factors are not influential in WiFi communication when considering the short distance for indoor links. Aggregation may not only achieve higher average throughput, but also maintain the advantages of both WiFi and VLC.

2.3 System Delay Analysis

In this section, we show the benefits of the aggregated system theoretically. This is done by comparing the delay performance of this system to another system that assigns each request to either the VLC channel or the WiFi channel. In the aggregated system, any request is divided into two and the resulting two pieces of the request are forwarded to the WiFi and VLC channels, respectively. We also derive the optimal requests splitting ratio. In the second system, the request is forwarded to either WiFi or VLC channel. The optimal ratios of the requests to be forwarded to either WiFi or VLC are also derived for this system. The major result we get in this section is that the minimum average delay of the aggregated system is always lower than that of non-aggregated system. We realize that the effect of lower delay will be less drastic as the number of VLC hotspots increases.

In our system model, we have one WiFi AP and one VLC hotspot. Requests arrive to the system according to a Poisson process with rate λ. The size of the request follows an exponential distribution with an average value of μ. The bandwidth of the WiFi channel and the VLC channel are B_1 and B_2, respectively. We assume that $B_1 < B_2$.

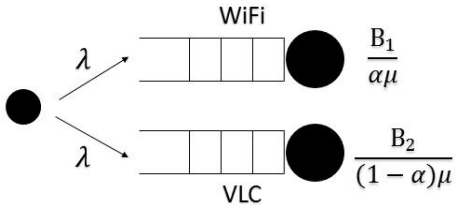

Figure 2.6 Queuing model representing the aggregated system model.

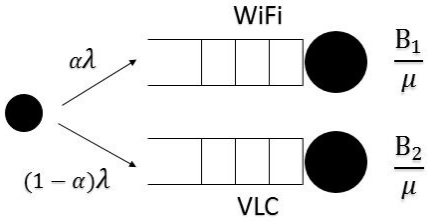

Figure 2.7 Queuing model representing the Non-aggregated system model.

2.3.1 Aggregated System Analysis

Let α represent the percentage of the request's size that is sent to the WiFi channel. Based on the above discussion, the aggregated system can be represented by the queuing system in Figure 2.6. Since one request is split into two and forwarded to each channel, the average requests arrival rates for WiFi and VLC are both λ. Since μ represents the average request size, the average serving rates of WiFi and VLC are $B_1/\alpha\mu$ and $B_2/(1-\alpha)\mu$, respectively.

Lemma 1. *In the aggregated system model, the minimum average system delay is* $\frac{\mu}{B_1+B_2-\lambda\mu}$.

Proof. The optimization problem can be written as follows:

$$\text{Objective: } \min \; E[\max(D_{WiFi}, D_{VLC})] \tag{2.1}$$

$$s.t.\ 0 \leq \alpha \leq 1$$

$$\lambda < B_1/\alpha\mu$$

$$\lambda < B_2/(1-\alpha)\mu$$

$$B_1 < B_2$$

Based on M/M/1 queuing model, the average system delay of WiFi and VLC are exponentially distributed with average rates $D_{WiFi} = \frac{1}{[B_1/\alpha\mu]-\lambda}$ and $D_{VLC} = \frac{1}{[B_2/(1-\alpha)\mu]-\lambda}$, respectively. In the aggregated system model, when one request comes, it is separated into two. One part of the request is sent to the WiFi channel and the other part is sent to the VLC channel at exactly the same time. Also, the sizes of the two parts of the request are dependent. Therefore, minimizing the maximum delay of WiFi and VLC, given in equation (1), is equivalent to $D_{WiFi} = D_{VLC}$. According to the above discussion, we can conclude that the optimal α and the minimum average system delay are

$$\alpha_{opt\_agg} = \frac{B_1}{B_1 + B_2}$$

$$D_{min\_agg} = \frac{\mu}{B_1 + B_2 - \lambda\mu}$$

□

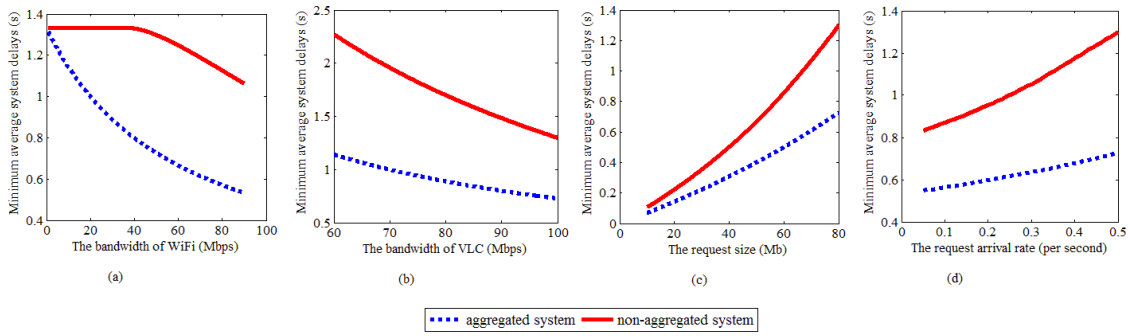

Figure 2.8 Minimum average system delays in terms of (a) B_1; (b) B_2; (c) μ; (d) λ.

2.3.2 Non-aggregated System Analysis

Let α denote the percentage of the requests that is sent to the WiFi channel. The non-aggregated system is equivalent to the queuing system in Figure 2.7. We assume that the requests are randomly allocated to each channel. Hence, the requests arrival for each queue is still Poisson process. The average requests arrival rates in WiFi and VLC are $\alpha\lambda$ and $(1-\alpha)\lambda$, respectively. Since there is no request splitting in this model, the average serving rates of WiFi and VLC are B_1/μ and B_2/μ, respectively.

Lemma 2. *In the non-aggregated system model, the minimum average system delay is*

$$D_{min\_non\_agg} = \begin{cases} \frac{2\lambda\mu - B_2(1-\sqrt{\beta})^2}{\lambda[B_2(\beta+1)-\lambda\mu]}, & \textit{if } \frac{B_2}{\lambda\mu}(1-\sqrt{\beta}) < 1 \\ \frac{\mu}{B_2-\lambda\mu}, & \textit{otherwise} \end{cases}$$

Proof. The optimization problem can be presented as follows:

$$\text{Objective: } \min \ \alpha D_{WiFi} + (1-\alpha) D_{VLC}$$

$$s.t.\ 0 \leq \alpha \leq 1$$

$$\alpha\lambda < B_1/\mu \tag{2.2}$$

$$(1-\alpha)\lambda < B_2/\mu \tag{2.3}$$

$$B_1 < B_2$$

In order to find the candidate minimum point, we describe the average delay of non-aggregated system as a function

$$\begin{aligned} D(\alpha) &= \alpha D_{WiFi} + (1-\alpha) D_{VLC} \\ &= \frac{\alpha}{B_1/\mu - \alpha\lambda} + \frac{1-\alpha}{B_2/\mu - (1-\alpha)\lambda} \end{aligned}$$

We can observe that $D(\alpha)$ is continuous in $(1 - B_2/\lambda\mu, B_1/\lambda\mu)$. Based on constraints (2) and (3), we have $1 - B_2/\lambda\mu < 0$ and $B_1/\lambda\mu > 1$. Hence, $D(\alpha)$ is continuous in [0,1]. To find the extreme points, the derivative of $D(\alpha)$ is calculated

$$D'(\alpha) = \frac{a\alpha^2 + b\alpha + c}{f^2(\alpha)},$$

$where$

$$a = \lambda^2(B_1 - B_2),$$

$$b = 2\lambda B_1(-\lambda\mu + 2B_2)/\mu,$$

$$c = B_1(B_2^2 - 2\lambda\mu B_2 + \lambda^2\mu^2 - B_1B_2)/\mu^2,$$

$$f(\alpha) = \sqrt{\mu}(-\lambda\alpha + B_1/\mu)(\lambda\alpha + B_2/\mu - \lambda).$$

Here, $f^2(\alpha) \neq 0$ when α is in [0,1]. Since $a < 0$ and $b^2 - 4ac > 0$, $D'(\alpha)$ has two zero points α_1 and α_2. We observe that

$$\alpha_1 = \frac{\lambda\mu\sqrt{\beta}/B_2 + \sqrt{\beta}(\sqrt{\beta} - 1)}{\lambda\mu(\sqrt{\beta} + 1)/B_2} \tag{2.4}$$

$$\alpha_2 = \frac{\sqrt{\beta}[1 - B_2(\sqrt{\beta} + 1)/(\lambda\mu)]}{\sqrt{\beta} - 1} \tag{2.5}$$

$$\alpha_2 - \alpha_1 = \frac{2\sqrt{\beta}[1 - B_2(\beta + 1)/(\lambda\mu)]}{\beta - 1} \tag{2.6}$$

where $\beta = B_1/B_2$ and $\beta < 1$. In equation (4), the numerator is greater than $\lambda\mu/B_2$ and the denominator is less than $\lambda\mu/B_2$. Thus, we prove that $\alpha_1 < 1$. In equation (5), the numerator and the denominator are both less than zero. Hence, we also prove that $\alpha_2 > 0$. In equation (6), since the numerator and denominator are both less than zero, α_2 is greater than α_1. According to the above discussion, we can observe that i) $D'(\alpha) < 0$ when $\alpha < \alpha_1$ or $\alpha > \alpha_2$; ii) $D'(\alpha) > 0$ when $\alpha_1 < \alpha < \alpha_2$.

Since $\alpha_1 < 1$ and $\alpha_2 > 0$, we consider four cases: i) $0 < \alpha_1 < 1$ and $0 < \alpha_2 < 1$; ii) $\alpha_1 \leq 0$ and $0 < \alpha_2 < 1$; iii) $0 < \alpha_1 < 1$ and $\alpha_2 \leq 0$; iv) $\alpha_1 \leq 0$ and $\alpha_2 \leq 0$. In case i)

and iii), $D_{min}(\alpha) = D(\alpha_1)$. In case ii) and iv), $D_{min}(\alpha) = D(0)$ because $D(0) < D(1)$. After substituting $\alpha = 0$ and $\alpha = \alpha_1$ into $D(\alpha)$, we get

$$D(0) = \frac{\mu}{B_2 - \lambda\mu}$$
$$D(\alpha_1) = \frac{2\lambda\mu - B_2(1-\sqrt{\beta})^2}{\lambda[B_2(\beta+1) - \lambda\mu]}$$

Note that $D_{min\_non\_agg} = D(\alpha_1)$ iff $\alpha_1 > 0$. It means that $\frac{B_2}{\lambda\mu}(1-\sqrt{\beta}) < 1$. □

2.3.3 Comparison

Theorem 1. *Aggregated system has a lower minimum average system delay than the non-aggregated system.*

Proof. Compared to the minimum average system delay of aggregated, $D(0)$ is obviously less than D_{min_agg}. Since $D(\alpha_1) - D_{min\_agg} = \frac{1-B_2(1-\sqrt{\beta})^2/(\lambda\mu)}{\lambda[B_2(\beta+1)/(\lambda\mu)-1]}$, and $B_2(1-\sqrt{\beta}/(\lambda\mu) < 1$, $D(\alpha_1)$ is greater than D_{min_agg}. □

Figure 2.8 represents the simulation results of the delay for the above two systems. The values of the λ, μ, B_1, B_2 are set as 0.5/s, 80 Mb, 50 Mpbs, 100 Mbps, respectively. In each plot, we vary one of these four parameters while keeping the other three as the above values. In Figure 2.8 (a), the minimum average delay of the non-aggregated system only depends on the bandwidth of VLC channel until the bandwidth of WiFi channel increase to 36 Mbps. When B_1 = 50 Mbps, the minimum average delay of aggregated system is around 50% of that of non-aggregated system. In Figure 2.8 (b), as the bandwidth of VLC channel increases, more requests are allocated to VLC channel in the non-aggregated system. Therefore, the delay difference between two systems is decreasing. In Figure 2.8

(c), we can observe that when the request size becomes extremely small, the delays of two systems converge to the same value. The reason for this convergence behavior is that reducing the request size will reduce the benefits obtained from splitting the requests in the aggregated system. In Figure 2.8 (d), increasing the arrival rate has more impact on the minimum average delay of the non-aggregated system than on that of the aggregated system. The analytical results revealed in these four figures also coincide with our theoretical analysis.

This analysis shows how data aggregation can improve system performance, specifically in scenarios where the WiFi and VLC channels are on the same order of magnitude. It is expected that aggregation will provide diminishing gains over the non-aggregated system as the number of VLC channels increases and the ratio of WiFi capacity to aggregate VLC capacity goes towards 0. This is due to the additional WiFi capacity having a decreasing effect per VLC channel; however, aggregation can provide performance improvements when a small subset of the VLC channels have high traffic demands. This coincides with our results in Section 2.4 when considering scenarios where a single VLC channel uses data aggregation to improve performance for devices associated with it.

2.4 Experiments

2.4.1 VLC Front-ends and Performance of the Single VLC Link

VLC front-ends Similar to RF communication, the capabilities of VLC strongly depend on the analog front-ends such as power amplifiers and antennas. Also, the optical source and photodetector have a great effect on the performance of VLC. Our proposed

systems, coexisting WiFi and VLC, require high-speed front-ends with PHY and MAC layer implementation. The PC-LED contains a blue light source and enveloped by a yellow phosphor to produce white light. This low-cost LED provides only narrow modulation bandwidth caused by slow response time of the phosphorescent material. Our collaborators in Fraunhofer-HHI have recently developed a small form factor current driver using an off-the shelf high power white LED. The VLC receiver consists of a transimpedance amplifier (TIA) and a commercially available high-speed Si-PIN photodiode (PD). It is reported that the modulation bandwidth has been improved from 3-7 MHz to 20 MHz. This enhancement is realized by reducing the effect of phosphorescent portion in the optical spectrum with the aid of a blue filter at the receiver end. The new VLC transceivers shown in Figure 2.9 has significantly increased the modulation bandwidth to above 100 MHz by means of precise impedance matching between the LED and the high-power analog driver as well as between the PD and the low-noise amplifier followed by. Fraunhofer-HHI has currently implemented an available bi-directional VLC link with a 150 MHz analog transmitter, a 100 MHz analog receiver and a 70 MHz orthogonal frequency-division multiplexing (OFDM) baseband processor. As shown in Fig 2.9, each device comprises an external power supply and a 1 Gbps Ethernet port using RJ45 standard. Two modules (transceivers) are operating like an Ethernet bridge allowing the transfer of all kinds of data. Altogether, a gross and net data rate of 500 and 260 Mbps are possible with one-way latency of around 10 ms.

Performance of indoor and outdoor VLC links Based on the VLC front-ends developed by our collaborators at Fraunhofer-HHI, we conduct experiments indoor and outdoor to evaluate the average throughput of the VLC link. For indoor experiment, we

Figure 2.9 VLC front-ends.

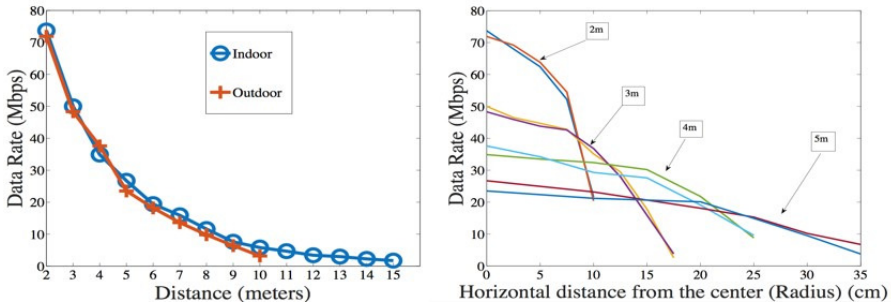

Figure 2.10 Throughput vs. vertical and horizontal distance between VLC transceivers.

measure the throughput within the range of 2-15 meters while the range is 2-10 meters for outdoor experiment. Note that the distance here represents the vertical distance between two transceivers and the horizontal distance is equal to 0. We also measure the throughput at various horizontal distance within the coverage of the VLC source. All the measurement results are averaged over 100 runs. Each run is a throughput test and spends 5 seconds. Figure 2.10 (left) represents the average throughput vs. the vertical distance. We achieve around 74 Mbps at 2 meters and the throughput drops to about 25 Mbps at 5 meters. Note that the vertical distance for most indoor applications is in this range. Also note that the throughput results here with short vertical distance are higher than the typical throughput that can be achieved by using WiFi with 2.4 GHz channel conformed to standard 802.11 b/g/n. As we can observe, the throughput results for the outdoor experiment are very similar to those for indoor experiment. Note that the outdoor environment can represent the extreme condition that happens indoor, with windows open and extensive lighting. The

results prove that the VLC front-ends are suitable for the extreme indoor case. Figure 2.10 (right) shows the average throughput when we vary the horizontal distance within the vertical distance from 2m to 5m.

Note that the data rates measured here are associated with both, a customized configuration of the VLC front-ends and a different metric used, compared to [40] and [41]. In particular, different LEDs are used (downlink is white LED while uplink is infrared, instead of red and blue, respectively). Red LED power is higher in the downlink and the PD is more sensitive to reddish colors. Due to eye safety, infrared power is more limited in the uplink than for blue light. Finally, the results in the present paper represent the net data rate measured on the application layer in the OSI model while our previously published data refer to the gross data rate at the physical layer, as it is measured at the baseband processing chipset.

2.4.2 Testbed of the Hybrid System

In the testbed of our proposed hybrid system, we have two PCs with Linux OSs (Ubuntu 12.0.4 LTS), a NETGEAR Wireless Dual band Gigabit Router WNDR4500, and two VLC transceivers provided by Fraunhofer-HHI. The PC which performs relaying functions is equipped with two Ethernet cards: Inter Corporation 82579LM and 82574L Gigabit Ethernet Controllers. The client PC is equipped with one wireless card and one Ethernet card: a Boradcom 802.11n Network Adapter and a Broadcom NetXtreme Gigabit Ethernet controller respectively. All the NICs support 10/100/1000M speed.

Regarding the network configuration, router's LAN IP address is set to 192.168.1.1/24 as default. Referring to Figure 2.3, the IP addresses of NIC A-1, NIC B-1, NIC

A-2 and NIC B-2 are manually configured as 192.168.1.200/24, 192.168.1.100/24, 192.168.2.200/24 and 192.168.2.100/24 respectively. The IPv4 routing table in client PC is shown in Table 2.2. And an additional entry in client's ARP table is added by typing "arp -s 192.168.2.1 ab:ab:ab:ab:ab:ab" in command window with root privilege.

For the VLC unidirectional link setup, since the VLC devices provided by Fraunhofer-HHI are both transceivers, we manually turn off the forwarding function in PC I (relay), in order to construct a network-level unidirectional VLC channel. Regarding the VLC connection establishment, there are Ethernet ports on the VLC transceivers, therefore, simply connecting the transceivers to the PCs with Ethernet cable constructs the wireless VLC link.

2.4.3 Testbed of the Aggregated System

To implement the aggregation of two wireless links, we use one PC with Linux OSs (Ubuntu 12.0.4 LTS), a NETGEAR Wireless Dual band Gigabit Router WNDR4500, a client mode TP-LINK wireless router 150 Mbps TL-WR702N, and also the two VLC transceivers. The client PC is equipped with two Ethernet cards: Inter Corporation 82579LM and 82574L Gigabit Ethernet Controllers. Both the NICs support 10/100/1000M speed. Regarding the network configuration, in order to construct the aggregated system, we add one line to /etc/modules: "bonding mode=6". After that, we modify the /etc/network/interfaces. We change the eth0 and eth1 to auto DHCP and also add the static logic bond0. The detailed commands are shown in Figure 2.11.

```
auto lo
iface lo inet loopback

iface eth0 inet dhcp
iface eth1 inet dhcp

auto bond0
iface bond0 inet static
address 192.168.1.88
netmask 255.255.255.0
gateway 192.168.1.1
up ifenslave bond0 eth0 eth1
down ifenslave -d bond0 eth0 eth1
```

Figure 2.11 Bonding configuration.

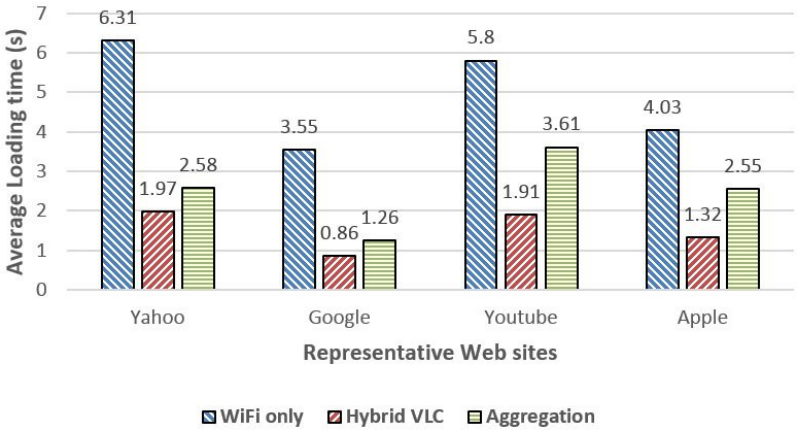

Figure 2.12 Loading time in web browsing.

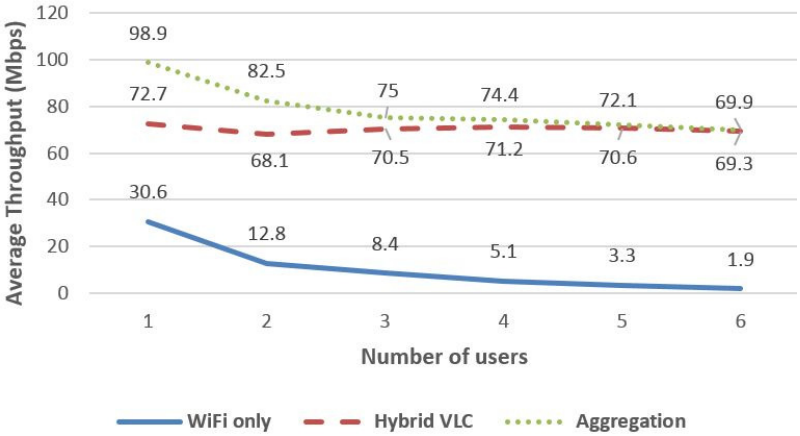

Figure 2.13 Throughput vs. Number of contenders.

Table 2.2 Routing Table of Client

Destination	Gateway	Genmask	Flags	Metric	Interface
0.0.0.0	192.168.2.1	0.0.0.0	UG	0	eth0
169.254.0.0	0.0.0.0	255.255.0.0	U	1000	eth1
192.168.2.0	0.0.0.0	255.255.255.0	U	2	eth0

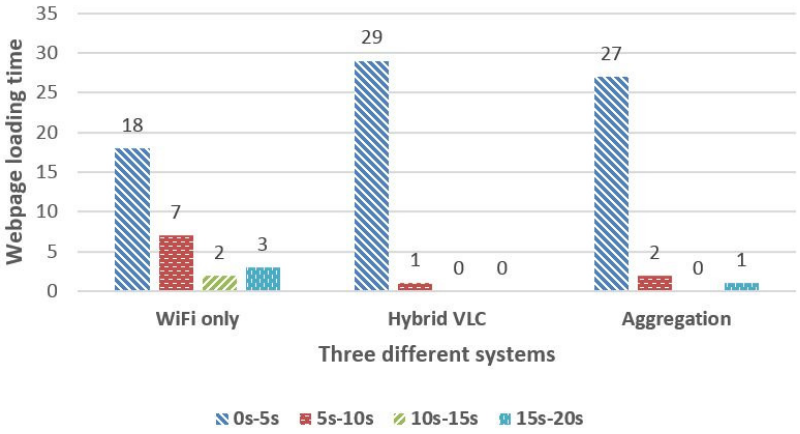

Figure 2.14 Statistic of yahoo homepage loading time.

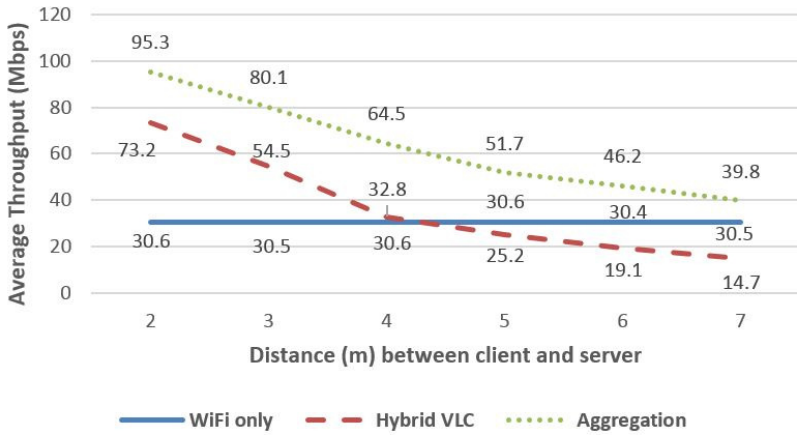

Figure 2.15 Throughput vs. Distance between tx and rx.

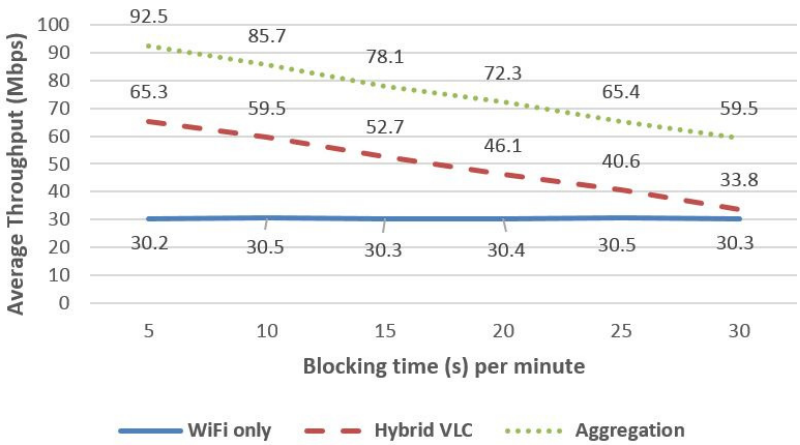

Figure 2.16 Throughput vs. Block duration.

2.4.4 Results and Analysis

Iperf [42] is a pervasively used tool to measure the network performance. Due the limited bandwidth allocated by the ISP, we setup an internal network with a client, a server and a router, for the purpose of measuring the achievable bandwidth of system. We install iperf on both the client and the server to test the average TCP throughput in all the experiments except the test of web page loading time. All throughput results are averaged over 100 runs. Each run spends 5 seconds.

In Figure 2.13, we show the average of TCP throughput achieved by the three different systems(the two systems described in Section 2.2 in addition to a system that uses WiFi only). The distance between the transmitter and the receiver is 2m for both WiFi and VLC. As the number of contending WiFi users is increasing, we test the average TCP throughput obtained by a selected user who uses the three different systems. We set the wireless mode of the router to "up to 54 Mbps", hence the TCP throughput achieved by the single WiFi user is around 30 Mbps. As the number of users is increasing, the performance of WiFi declines sharply. In contrast, since the contending WiFi users only contend with the uplink wireless channel of hybrid VLC, the throughput of the hybrid VLC user is around 70 Mbps, regardless of the number of users, which is 5 times higher than the WiFi only users when the number of users increases to 6. Also, we can observe that the higher throughput achieved by the aggregated system, which is represented by the dot line, is almost the aggregated value of the throughput of WiFi only and hybrid VLC. To satisfy the specific users who need extremely high downloading data rate, the aggregated system can be utilized. Note that compared to our previously published work [37], the

average throughput is enhanced from 150 Kbps (limited by the software-defined-VLC) to 70 Mbps, which is increased by around 477 times.

In addition to the throughput measurement, we also evaluate the loading time of web browsing by selecting several representative web sites. Pingdom[3] online website speed test is used to estimate the loading time of the webpages. As shown in Figure 2.12, we investigate the completion time of the home webpages of yahoo, google, youtube and apple on one client located in a network comprised of 10 clients (the other 9 WiFi users are downloading a 1GB file through the same access point). We can observe that the shortest loading time occurs when the selected user chooses the hybrid VLC system. Theoretically speaking, only the WiFi channel could be congested by the other WiFi users, it is reasonable that the loading time of aggregated system is shorter than the WiFi only but longer than the hybrid VLC. Therefore, based on our implementation, the network performance of the aggregated system is not always better than the hybrid system. This is because the condition in Section 2.3 are not always satisfied. Our final results of loading time are averaged over 30 runs. Each run is a web page loading time test via Pingdom website. The statistics of the yahoo's homepage loading time are shown in Figure 2.14. Most of the loading time in hybrid and aggregated systems are distributed within the range of 0s-5s. However, three test results are distributed in the range of 15s-20s in WiFi only system. With the WiFi access point congested, the level of network delay may be highly degraded due to the increased back-off penalty.

The short range factor of VLC is inevitable, hence we vary the distance between the transmitter and the receiver for both WiFi and VLC, to measure the average TCP

[3]http://tools.pingdom.com/fpt/ (accessed 1-May-2014).

throughput. The experiments results are shown in Figure 2.15. As the distance is increasing, the achievable throughput of hybrid VLC user is decreasing quickly. However, the WiFi only system has a stable network performance. The throughput of the WiFi only exceeds the hybrid VLC when the distance is increased to 4.1m. To some extent, the aggregated system is capable of providing a throughput with the lowest bound that is higher than the WiFi only. Therefore, the aggregation technique improves the integrated data rate and offers users with more reliable communication.

Due to the particularly small wavelength of the visible light, VLC channel can be easily blocked by tiny objects. Regarding the irregular movement of mobile devices, the channel blockage duration becomes a considerable factor when we evaluate the network performance of VLC. We vary the blocking time from 5s to 30s per minute and test the average TCP throughput achieved by the three systems. Figure 2.16 demonstrates the experiments results. Even if the blocking time in VLC channel is increased up to 30s per minute, the achievable TCP throughput is still higher than the WiFi only system. Therefore, compared to the distance, the blocking duration may be less influential. Additionally, although the throughput of aggregated system is also decreased, it would not be lower than that of the WiFi only system. The blockage duration experiment further proves the robustness of the aggregated system.

2.5 Related Work

Early work on hybrid systems integrating RF and VLC are based on simulation and analysis [5–8]. To the best of our knowledge, none of these hybrid systems were able

to develop practical system implementation yielding functional IP-based communication supporting web browsing or other Internet access functionalities.

A model for integrating WiFi and VLC has previously been proposed but not implemented [5]. In this model, downlink VLC channels are proposed to supplement an existing RF channel. Handover techniques are defined for resolving discontinuities due to mobility and specifically to transfer between a symmetric RF link and the asymmetric VLC-RF link as a device transits an indoor space. In this prior work, the primary contributions are simulation and analysis of the downlink channel under the assumption of a reliable RF uplink.

Device cost and energy consumption relative to data throughput have been investigated for a hybrid VLC system [6]. The authors show advantages for an RF uplink compared to a VLC uplink, but primarily as related to energy cost for transmission. This work motivates us to study the hybrid system that replaces the energy-expensive uplink with RF.

Energy-efficient connectivity for a hybrid radio-optical wireless systems has also been investigated in [7]. In this work the authors show via simulation that connectivity and energy consumption depend on user device density, coverage range ratio between single-hop and multi-hop, relay probabilities, and mobility of the user. Although the proposed WLAN-VLC network model shows the positive impact of a hybrid system, the approach they used relies on an ideal scenario that entails prior assumptions.

Room division multiplexing (RDM) has been demonstrated under a hybrid VLC network model [8]. The core component of this hybrid system is the VLC network coordinator, which is responsible for RDM-based service division and distribution as well

as for providing bidirectional interfaces between the outdoor and indoor communication infrastructure, especially the indoor interfaces for uplink WiFi access and downlink LED lamps. This work, however, does not appear to extend to full implementation of the network protocol stack nor implementation in the system kernel. Finally, the work is evaluated by waveform measurement without the signal processing and demodulation required for practical use.

Each of the aforementioned works focuses on simulation analysis without implementation of the full end-to-end system required to provide evaluation at the application layer. In contrast, we implement a practical hybrid WiFi-VLC wireless system, which enables the typical Internet access connection between client and server *without any reconfiguration at the server side*. Data packets generated by user applications are transmitted through WiFi and requested data from the server is received via the VLC interface.

Early efforts on the data link layer aggregation were also based on the simulations [43–48]. To the best of our knowledge, none of the above work evaluates the performance of their presented policy based on real experiments.

The concept of generic link layer (GLL) that aggregates multiple radio access at the radio level is introduced in [43]. The GLL enables multi-radio transmission diversity (MRTD), which transmits a traffic flow sequentially or parallel over aggregated radio access technologies. The significant functions in GLL include access selection schedule, performance monitoring and flow error control. GLL blindly assigns the traffic to different interfaces. Based on the GLL concept, the authors further study the switched MRTD in [44]. Based on the measured throughput of each radio access technology, the work

sorts the interfaces in descending order of their available throughput. The traffic flows are distributed to the interfaces in the descending order. In [45], another factor, round trip time (RTT) is utilized to schedule the traffic through the interfaces. In [44] and [45], the switched MRTD is presented as an adaptive mode of the original MRTD. However, with similar available throughput over the interfaces, the proposed scheme produces inevitable redundant switching overheads.

A cognitive convergence layer (CCL), which is similar to GLL is introduced in [46]. The authors propose a logic link layer interface for managing the traffic flows through real link layer interfaces. A traffic distribution policy is implemented at the sender and a reorder buffer is added at the receiver. A function of link transmission time (LTT) is used to estimate the links capacities. The CCL-based data link aggregation is further investigated in [47]. The authors use the link delay as a criterion to determine the data traffic distribution over tightly-coupled WiMAX and WiFi network. In [48], the measurement of channel occupancy time for a single packet transmission is used as the decision metric. The air-time cost based scheme is reported as a more adaptive link aggregation schedule than the RTT-based policy.

All of the above-mentioned data link layer aggregation works focus on the network parameters, which are used for determining the link selection. None of them provided implementation of their proposed schemes or experimental analysis. In our work, we set up the testbed based on the bonding driver of Linux OS and evaluate the TCP throughput as well as the user experience for web browsing. We also provide a rigorous mathematical analysis of our implemented system.

2.6 Conclusion

In this chapter, we evaluate two heterogeneous systems incorporating WiFi and VLC. Our goal is to provide a proof of concept for the coexistence between these two communication bands. Within a short distance between the transmitter and the receiver, the hybrid VLC could perform much better than the WiFi system in the crowded wireless environment. As a complementary technique, VLC deserves further investigation. However, on the one hand, WiFi infrastructures are prevalent and highly acceptable by most consumers; on the other hand, WiFi may outperform VLC in the case of long-distance data transmission or the existence of obstacles. We have also proven through theoretical analysis that the aggregated system is capable of providing better network performance than that of the non-aggregated system for most delay-sensitive applications. Therefore, we conclude that the aggregation between WiFi and VLC is worthy of further study, to effectively utilize the aggregated bandwidth and to lower the network delay.

CHAPTER 3

DELAY ANALYSIS OF HETEROGENEOUS RF-VLC NETWORKS

3.1 Introduction

Heterogeneous wireless network, as a method to incorporate different access technologies, contains the potential capabilities of improving the efficiency of spectral resource utilization. Traffic offloading to omnidirectional small cells (OSCs), such as RF femtocells and WiFi WLANs, has already become an established technique for adding capacity to dense environments where macrocells are overloaded. Ultra-dense distributed directional small cells (DSCs), deployed in indoor environments, can supplement OSCs in areas like apartment complexes, coffee shops, and office spaces where device density and data demand are at their highest. These DSCs can be implemented by technologies like microwave [12], mmwave [13] and optical wireless. Optical wireless (OW) communication - specifically visible light communication (VLC) or LiFi [14] - is a directional communication technology that has gained interest within the research community in recent years. As an excellent candidate for 5G wireless communication, VLC provides ultra wide bandwidth and efficient energy utilization [49]. Weaknesses of VLC is manifested as the vulnerability to obstacles.

In this chapter [1], we consider two cases of heterogeneous OSC-DSC networks. One case is the coexistence of OSCs without contention (OSCNCs) and DSCs with negligible blockage rate (DSCNBs). A typical application of OSCNC is the RF femtocells, which are owned/controlled by a global entity (i.e., service provider). Therefore, interference can

[1]The work of this chapter has been published in [50]

be mitigated in the provisioning process and multiple adjacent RF femtocells can perform downlink data transmission simultaneously without contention. This non-contention issue will be further discussed in Section 3.3. The other case is the heterogeneous network incorporating OSCs with contention (OSCCs) and DSCs with considerable blockage rate (DSCBs). In contrast to OSCNC, OSCC, such as WiFi AP, is purchased by local entities (i.e., home/business owners) and deployed in an ad-hoc manner such that interference is not planned. Particularly, WiFi networks employs the Carrier Sense Multiple Access with Collision Avoidance (CSMA/CA) protocols to schedule the contention process. DSCs have a large reuse factor such that the spectrum reuse can be easily implemented even in an indoor environment. Compared to the ideal DSCNBs, one of the difference of DSCBs is the line-of-sight blockage issue, which is an inevitable problem in VLC. Without the loss of generality, we use OSC and DSC notations instead of RF and VLC in the following description.

This chapter characterizes the system delay (here system delay is defined as the amount of the time from the instant the request arrives at the AP to the instant that it successfully departs from the AP) of two cases of heterogeneous OSC-DSC wireless networks: (i) OSCNC-DSCNB; (ii) OSCC-DSCB. For each case, two schemes are taken into consideration. One of them is based on bandwidth aggregation and the other is not. The potential gain in terms of the minimum average system delay through aggregating the bandwidth of OSC and DSC is also evaluated. The main contributions include the following: (i) for the heterogeneous OSCNC-DSCNB wireless network, a generalized characterization of the system without bandwidth aggregation is derived in terms of the optimal ratio of traffic allocation and the minimum average system delay, and a

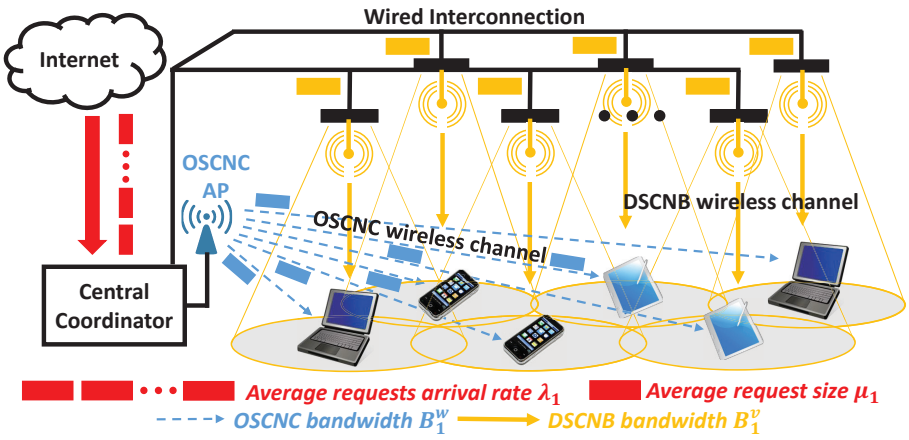

Figure 3.1 Heterogeneous OSCNC-DSCNB network architecture.

near-optimal characterization of the minimum average system delay of the system that utilizes bandwidth aggregation is proposed; (ii) for the heterogeneous OSCNC-DSCNB wireless network, it is also theoretically proved that the minimum average system delay of the system based on bandwidth aggregation is lower, when compared to that of the system without bandwidth aggregation; (iii) for the heterogeneous OSCC-DSCB wireless network, the average system delay is derived for both the system without bandwidth aggregation and the system with bandwidth aggregation; (iv) for the heterogeneous OSCC-DSCB wireless network, extensive simulations are also conducted to indicate that under certain conditions, the system without bandwidth aggregation outperforms the system with bandwidth aggregation in terms of minimum average system delay.

3.2 System Model

A recent measurement study [51] on traces of 3785 smart phone users from 145 countries over a four-month period shows that the ratio of download traffic to its upload traffic is 20:1. Therefore, in this chapter, we investigate the downlink system delay of two cases of heterogeneous OSC-DSC wireless access networks:

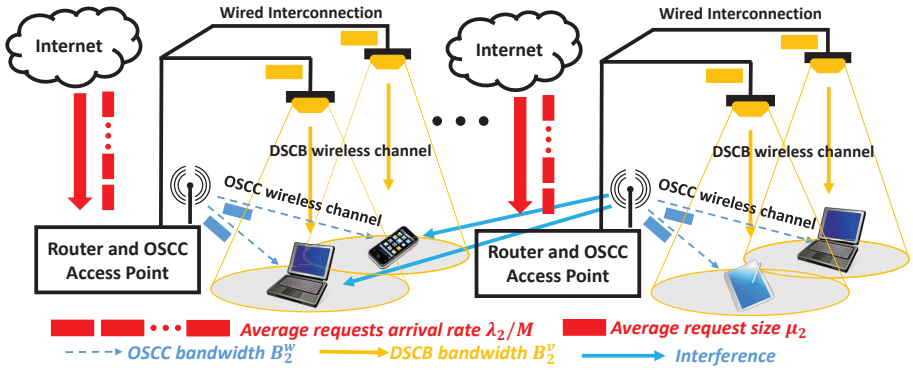

Figure 3.2 Heterogeneous OSCC-DSCB network architecture.

- Case 1: heterogeneous OSCNC-DSCNB network,
- Case 2: heterogeneous OSCC-DSCB network.

Figure 3.1 illustrates the network architecture for case 1. In the system model suggested, there are one OSCNC AP and N_1 DSCNB APs. Since no contention is considered among the OSC APs, under homogeneous traffic distribution, the delay analysis of a single OSCNC AP can be easily extended to that of multiple OSCNC APs. Due to the fact that the DSCs have a large reuse factor, it is rational to assume that all the DSC links can be active simultaneously with negligible interference among them. Under the homogeneous traffic assumption, the traffic assigned to different DSC APs is evenly distributed. The process of requests arrival to the central coordinator is a Poisson process with rate λ_1. The size of each request is exponentially distributed with mean μ_1. The downlink capacities of the OSCNC and the DSCNB are B_1^w and B_1^v, respectively, where $B_1^w < B_1^v$.

Figure 3.2 illustrates the network architecture for case 2. In this case, there are M OSCC APs and N_2 DSCB APs, where $N_2 > M$. All of the M OSCC APs are located in a single contention domain. The MAC scheme considered is IEEE 802.11 [52], which is implemented by using a Distributed Coordination Function based on the CSMA/CA

protocol. The RTS/CTS exchange scheme, which is utilized to address the "hidden node" problem, is also taken into account. The 802.11 configurations will be described in details in Section 3.5. The difference between DSCB here and the DSCNB discussed in case 1 is manifested as the vulnerability to line-of-sight blockage. This property of DSCB is modeled as a successful transmission probability P_{succ} for each request. The whole request will be retransmitted once the transmission fails. The Ack-enabled mechanism [53] for DSCB is considered. Under the homogeneous traffic assumption, the traffic assigned to different OSCC and DSCB APs are evenly distributed. The process of requests arrival to each router is a Poisson process with rate λ_2/M. The size of each request is exponentially distributed with mean μ_2. The downlink capacities of the OSCC and the DSCB are B_2^w and B_2^v, respectively.

For two cases of heterogeneous OSC-DSC wireless access networks, the system delay D performance is studied for two schemes: i) non-aggregated scheme and ii) aggregated scheme. In the non-aggregated scheme, any request is either allocated to the OSCNC/OSCC or the DSCNB/DSCB. In the aggregated scheme, each request is split into two pieces. One of them is forwarded to the OSCNC/OSCC while the other is forwarded to one of the DSCNB/DSCB APs. As a result, the system delay of each request is the maximum time spent in the system of the two pieces. New metrics $\alpha_1(\alpha_2)$ and $\beta_1(\beta_2)$ are defined for two cases, to represent the traffic allocation ratio and request splitting ratio for non-aggregated and aggregated schemes, respectively. These four factors will be discussed in detail in Section 3.4 and Section 3.5. The main notations are summarized in Table 3.1.

Table 3.1 Symbol Definition

$\lambda_1(\lambda_2)$	Total request arrival rate for the heterogeneous OSCNC-DSCNB network(the heterogeneous OSCC-DSCB network)
$\mu_1(\mu_2)$	Mean size of request for the heterogeneous OSCNC-DSCNB network(the heterogeneous OSCC-DSCB network)
$B_1^w(B_2^w)$	OSCNC(OSCC) bandwidth
$B_1^v(B_2^v)$	DSCNB(DSCB) bandwidth
M	The number of OSCC APs
$N_1(N_2)$	The number of DSCNB(DSCB) APs
P_{succ}	The successful transmission rate for DSCB links
$\alpha_1(\alpha_2)$	The percentage of traffic allocated to OSCNC(OSCC)
$\beta_1(\beta_2)$	The proportion of the size of each request assigned to OSCNC(OSCC)

3.3 Overview of Typical Omnidirectional Non-Contention and Contention Wireless Networks

As we discussed earlier, a typical omnidirectional non-contention wireless network is the RF femtocell network. RF femtocell is a small and low-power cellular base station, typically designed for coverage and capacity improvement. One of the most critical effect from deploying RF femtocells is the potential interference between femtocells and macrocells [54]. However, femtocells can incorporate interference mitigation techniques-detecting macrocells, adjusting power and scrambling codes accordingly [55] to cause the potential interference negligible. The interference management between neighboring femtocells and between femtocells and macrocells are also investigated in [56]. Clustering of femtocells [57,58], fractional frequency reuse (FFR) and resource partitioning [59,60], and cognitive approach [61] can be employed to mitigate the inter-femtocells interference. Since femtocells are deployed by service provider, which causes the above-mentioned interference mitigation techniques practicable. With interference issue solved, the neighboring RF femtocells can perform downlink data transmission at the same time without worrying about the contention process even at the cell edge.

For omnidirectional contention wireless network, a commonly used application is WiFi network. Since each WiFi AP is normally deployed personally without coordination with the neighboring WiFi APs, the interference among WiFi APs will inevitably trigger the contention process when the adjacent WiFi APs perform the downlink data transmission simultaneously. The CSMA/CA based MAC protocol of IEEE 802.11 [52] is designed to mitigate the collisions due to multiple WiFi APs transmitting on a shared channel. In a WiFi network employing CSMA/CA MAC protocol, each WiFi AP with a packet to transmit will first sense the channel during a Distributed Inter-frame Space (DIFS) to decide whether it is idle or busy. If the channel is idle, the WiFi AP proceeds the transmission. If the channel is busy, the WiFi AP defers the transmission until the channel becomes idle. The WiFi AP then initializes its backoff timer with a randomly chosen backoff period and decrements this timer every time it senses the channel to be idle. The timer stops decreasing once the channel becomes busy and the decrementing process will be restarted again after DIFS idle sensing. The WiFi AP attempts to transmit once the timer reaches zero. The backoff mechanism and the definition of contention window will be discussed later in Section 3.5.

3.4 System Delay Analysis for Heterogeneous OSCNC-DSCNB Network

This section presents how to mathematically derive the minimum average system delay of the non-aggregated scheme for heterogeneous OSCNC-DSCNB networks. It provides a theoretical proof that the performance of the aggregated scheme is always better than that of the non-aggregated scheme in terms of the minimum average system delay. For the evaluation of the minimum average system delay of the aggregated scheme, an efficient

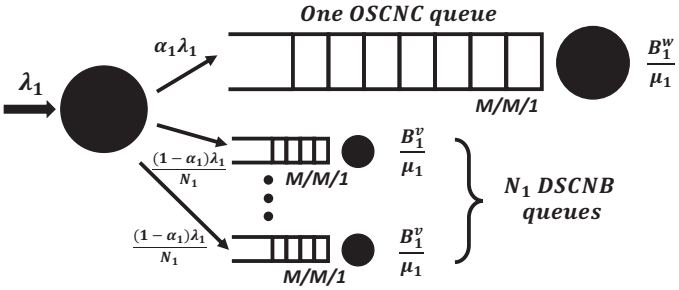

Figure 3.3 Queuing model representing the non-aggregated system model for heterogenous OSCNC-DSCNB networks.

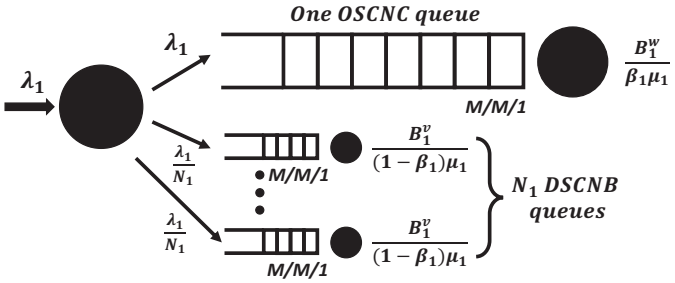

Figure 3.4 Queuing model representing the aggregated system model for heterogeneous OSCNC-DSCNB networks.

solution is proposed to empirically incur a delay penalty (less than 3%) over the optimal result and the comparison between the empirical results of the aggregated scheme and the delay performance of the non-aggregated scheme is also presented.

3.4.1 The Non-aggregated Scheme

Let α_1 denote the percentage of requests allocated to OSCNC. The non-aggregated scheme can be represented by the queuing model shown in Figure 3.3. Due to the assumption that requests are randomly forwarded to OSCNC and DSCNB, the requests arrival to each queue is still a Poisson process. Requests arrive to OSCNC and DSCNB queues with mean rates $\alpha_1\lambda_1$ and $(1-\alpha_1)\lambda_1/N_1$, respectively. The average service time of OSCNC and DSCNB queue are exponentially distributed with means B_1^w/μ_1 and B_1^v/μ_1, respectively. Thus, each OSCNC and DSCNB queue is characterized by the M/M/1 queuing model.

Theorem 2. *In the non-aggregated system model, the minimum average system delay is*

$$D_{min\_non\_agg} = \begin{cases} \frac{\mu_1 N_1}{B_1^v N_1 - \lambda_1 \mu_1}, \textit{ if } \frac{B_1^v N_1}{\lambda_1 \mu_1}(1 - \sqrt{\gamma N_1}) \geq 1 \\ \frac{\lambda_1 \mu_1 (1+N_1) - B_1^v N_1 (1-\sqrt{\gamma N_1})^2}{\lambda_1 [B_1^v N_1 (\gamma+1) - \lambda_1 \mu_1]}, \textit{ otherwise} \end{cases}$$

Proof. The optimization problem for minimizing the average system delay is formulated as follows:

$$\text{Objective: } \min \ \alpha_1 D_{OSCNC} + (1-\alpha_1) D_{DSCNB}$$

$$s.t. \ 0 \leq \alpha_1 \leq 1$$

$$\alpha_1 \lambda_1 < B_1^w / \mu_1 \tag{3.1}$$

$$(1-\alpha_1)\lambda_1 / N_1 < B_1^v / \mu_1 \tag{3.2}$$

In order to find the candidate minimum points, the average system delay as a function is described as follows:

$$\begin{aligned} D(\alpha_1) &= \alpha_1 D_{OSCNC} + (1-\alpha_1) D_{DSCNB} \\ &= \frac{\alpha_1}{B_1^w/\mu_1 - \alpha_1 \lambda_1} + \frac{1-\alpha_1}{B_1^v/\mu_1 - (1-\alpha_1)\lambda_1/N_1} \end{aligned}$$

$D(\alpha_1)$ is continuous in $(1 - B_1^v N_1/(\lambda_1 \mu_1), B_1^w/(\lambda_1 \mu_1))$. From constraints (3.1) and (3.2), we have $1 - B_1^v N_1/(\lambda_1 \mu_1) < 0$ and $B_1^w/(\lambda_1 \mu_1) > 1$. Hence, $D(\alpha_1)$ is continuous in [0,1]. The derivative of $D(\alpha_1)$ is

$$D'(\alpha_1) = \frac{a\alpha_1^2 + b\alpha_1 + c}{f^2(\alpha_1)}, \text{ where}$$

$$a = \lambda_1^2(B_1^w - B_1^v N_1^2),$$

$$b = \frac{2\lambda_1 B_1^w(B_1^v N_1 - \lambda_1\mu_1 + B_1^v N_1^2)}{\mu_1},$$

$$c = \frac{B_1^w((B_1^v)^2 N_1^2 - 2\lambda_1\mu_1 B_1^v N_1 + \lambda_1^2\mu_1^2 - B_1^w B_1^v N_1^2)}{\mu_1^2},$$

$$f(\alpha_1) = \sqrt{\mu_1}(-\lambda_1\alpha_1 + \frac{B_1^w}{\mu_1})(\frac{\lambda_1\alpha_1}{N_1} + \frac{B_1^v}{\mu_1} - \frac{\lambda_1}{N_1}).$$

Through this paper, it is found that $f^2(\alpha_1) \neq 0$ when α_1 is in [0,1]. Since $a < 0$ and $b^2 - 4ac > 0$, $D'(\alpha_1)$ has two zero points $\alpha_1(1)$ and $\alpha_1(2)$

$$\alpha_1(1) = \frac{\lambda_1\mu_1\sqrt{\gamma}/(B_1^v N_1) + \sqrt{\gamma}(\sqrt{\gamma N_1} - 1)}{\lambda_1\mu_1(\sqrt{\gamma} + \sqrt{N_1})/(B_1^v N_1)} \tag{3.3}$$

$$\alpha_1(2) = \frac{\sqrt{\gamma}[1 - B_1^v N_1(\sqrt{\gamma N_1} + 1)/(\lambda_1\mu_1)]}{\sqrt{\gamma} - \sqrt{N_1}} \tag{3.4}$$

$$\alpha_1(2) - \alpha_1(1) = \frac{2\sqrt{\gamma N_1}[1 - B_1^v N_1(\gamma + 1)/(\lambda_1\mu_1)]}{\gamma - N_1} \tag{3.5}$$

where $\gamma = B_1^w/(B_1^v N_1)$ and $\gamma < 1$. In equation (3.3), the numerator is less than $\lambda_1\mu_1/(B_1^v N_1)$ and the denominator is greater than $\lambda_1\mu_1/(B_1^v N_1)$. Thus, this is a proof that $\alpha_1(1) < 1$. In equation (3.4), the numerator and the denominator are both less than zero. This proves that $\alpha_1(2) > 0$. In equation (3.5), since the numerator and denominator are both less than zero, $\alpha_1(2)$ is greater than $\alpha_1(1)$. This means that i) $D'(\alpha_1) < 0$ when $\alpha_1 < \alpha_1(1)$ or $\alpha_1 > \alpha_1(2)$; ii) $D'(\alpha_1) > 0$ when $\alpha_1(1) < \alpha_1 < \alpha_1(2)$.

The discussion is divided into four cases: i) $0 < \alpha_1(1) < 1$ and $0 < \alpha_1(2) < 1$; ii) $\alpha_1(1) \leq 0$ and $0 < \alpha_1(2) < 1$; iii) $0 < \alpha_1(1) < 1$ and $\alpha_1(2) \leq 0$; iv) $\alpha_1(1) \leq 0$ and $\alpha_1(2) \leq 0$. In case i) and iii), $D_{min}(\alpha_1) = D(\alpha_1(1))$. In case ii) and iv), $D_{min}(\alpha_1) =$

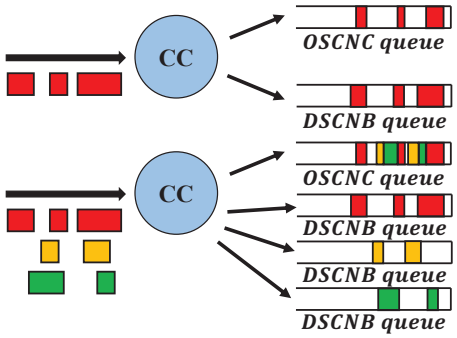

Figure 3.5 Requests distribution in the aggregated scheme for $N_1 = 1$ and $N_1 > 1$.

$D(0)$ because $D(0) < D(1)$. After substituting $\alpha_1 = 0$ and $\alpha_1 = \alpha_1(1)$ into $D(\alpha_1)$, it is found that

$$D(0) = \frac{\mu_1 N_1}{B_1^v N_1 - \lambda_1 \mu_1}$$
$$D(\alpha_1(1)) = \frac{\lambda) 1 \mu_1 (1 + N_1) - B_1^v N_1 (1 - \sqrt{\gamma N_1})^2}{\lambda_1 [B_1^v N_1 (\gamma + 1) - \lambda_1 \mu_1]}$$

Note that $D_{min\_non\_agg} = D(\alpha_1(1))$ iff $\alpha_1(1) > 0$. It means that $\frac{B_1^v N_1}{\lambda_1 \mu_1}(1 - \sqrt{\gamma N_1}) < 1$.

□

3.4.2 The Aggregated Scheme

Let β_1 denote the proportion of the size of each request that is allocated to the OSCNC. The aggregated scheme can be represented by the queuing model shown in Figure 3.4. Assuming that the requests arrival are randomly and evenly distributed to each DSCNB queue, the requests arrival to each DSCNB queue is still a Poisson process. The average requests arrival rates for OSCNC and DSCNB are λ_1 and λ_1/N_1. The average serving rates of OSCNC and DSCNB are $B_1^w/(\beta_1 \mu_1)$ and $B_1^v/[(1 - \beta_1)\mu_1]$. Similar to the non-

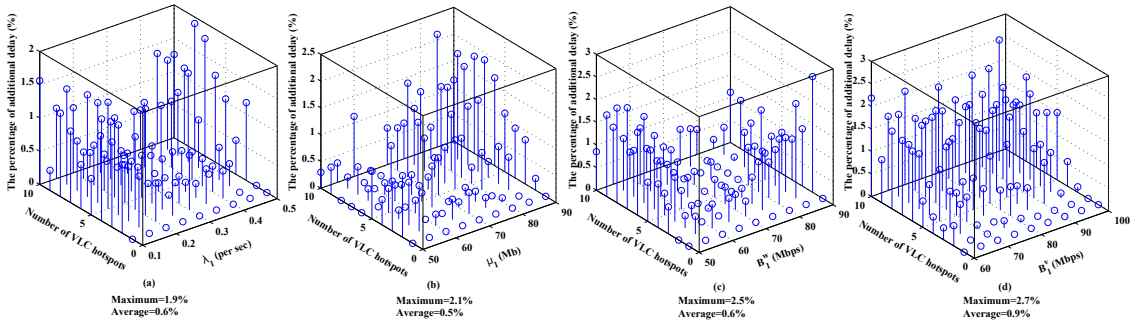

Figure 3.6 The percentages of additional delay caused by approximation in terms of (a) λ_1; (b) μ_1; (c) B_1^w; (d) B_1^v, with N_1 varied from 1 to 10.

aggregated scheme, each OSCNC and DSCNB queue can be characterized by the M/M/1 queuing model. The objective of the optimization problem can be expressed as minimizing $E[\max(D_{OSCNC}, D_{DSCNB})]$.

Figure 3.5 represents the requests distribution to OSCNC and DSCNB queues for $N_1 = 1$ and $N_1 > 1$. In Figure 3.5, it can be seen that when $N_1 = 1$, the delay of the DSCNB queue is fully correlated to that of the OSCNC queue. Therefore, achieving the objective value of minimizing $E[\max(D_{OSCNC}, D_{DSCNB})]$ is equivalent to obtaining the optimal β_1 from $E[D_{OSCNC}] = E[D_{DSCNB}]$. However, when $N_1 > 1$, the OSCNC queue contains different colored pieces of request, which are split from the requests flowing to different DSCNB APs. Each color represents a data stream destined to one DSCNB AP. The arrival times and the sizes of different colored pieces of request are independent while those of the same colored pieces of request are completely correlated. Specifically, due to the existence of yellow and green pieces of request (in Figure 3.5) in the OSCNC queue, the departure times of the red pieces of request in the OSCNC queue and the DSCNB queue are neither independent nor completely correlated. Hence, the complexity of computing the optimal β_1 is severely exacerbated. Instead of searching for the optimal β_1 by minimizing $E[\max(D_{OSCNC}, D_{DSCNB})]$, the objective is simplified

as minimizing $\max(E[D_{OSCNC}], E[D_{DSCNB}])$. For instance, let us assume that the delays of three pieces of request in OSCNC are 1, 2 and 3 seconds respectively, and the delays of the corresponding three pieces of request in DSCNB are 2 seconds for all. As such, the objective value of $E[\max(D_{OSCNC}, D_{DSCNB})]$ will be 2.33 seconds while the objective value of $\max(E[D_{OSCNC}], E[D_{DSCNB}])$ will be 2 seconds, which provides an underestimation of the traffic load. When the OSCNC queue is overwhelmed, approximated $E[D_{OSCNC}]$ will be lower than the real average request delay and vice versa. The error of this approximation approach depends on the congestion level of the OSCNC queue. The error value has been further validated not to exceed 3% by the results simulated in this chapter. To determine the approximated value of the optimal β_1 from the objective of minimizing $\max(E[D_{OSCNC}], E[D_{DSCNB}])$, we make $E[D_{OSCNC}] = E[D_{DSCNB}]$. Therefore, the approximated value of β_1 is, $\beta_1 = (-b - \sqrt{b^2 - 4ac})/(2a)$, where $a = \lambda_1\mu_1(1 - 1/N_1)$, $b = -[B_1^w + B_1^v + \lambda_1\mu_1(1 - 1/N_1)]$, and $c = B_1^w$.

By simulating the aggregated scheme with the approximated β_1, the percentages of additional delay caused by approximation are shown in Figure 3.6. The values of the $\lambda_1, \mu_1, B_1^w, B_1^v$ are initially set as 0.5/s, 90 Mb, 50 Mpbs, 100 Mbps, respectively. In each plot, one of these four parameters is varied while keeping the other three fixed at the initial values. With N_1 varied from 1 to 10, it is noticed that the percentage of the maximum additional delay is 2.7%, which is less than 3%. Figure 3.6 (a)-(c), shows that, as λ_1, μ_1 and B_1^w increase, the percentage of the additional delay decreases initially and increases after reaching the minimum level. However, in Figure 3.6 (d), the percentage of the delay penalty does not change much. Since OSCNC has the smaller bandwidth, maximum system delay of each request is more likely to be the system delay in OSCNC than that

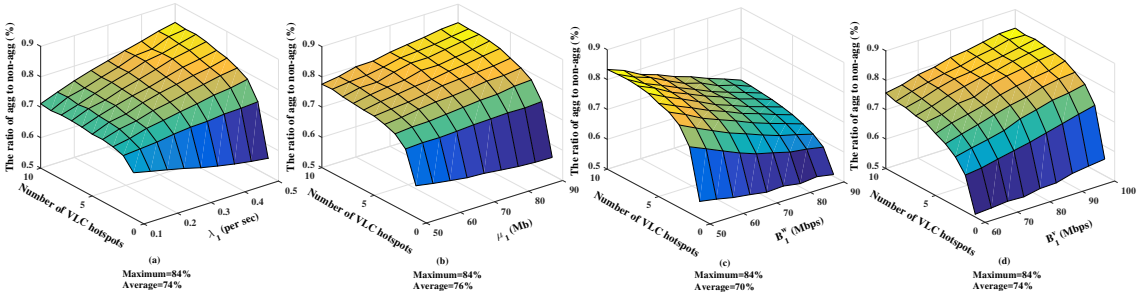

Figure 3.7 The ratio of the approximated minimum average system delay of the aggregated scheme to the minimum average system delay of the non-aggregated scheme in terms of (a) λ_1; (b) μ_1; (c) B_1^w; (d) B_1^v, with N_1 varied from 1 to 10.

in DSCNB. Therefore, the quantity of additional delay mainly depends on the level of congestion in OSCNC queue. Figure 3.6 (a)-(c) shows that the percentage of additional delay has the minimum values when $\lambda_1 \approx 0.33$, $\mu_1 \approx 58$ and $B_1^w \approx 70$, respectively. When $\lambda_1 < 0.33$, $\mu_1 < 58$ and $B_1^w > 70$, the approximation approach overestimates the congestion level of OSCNC and causes additional traffic load allocated to DSCNB, and vice versa. Note that when $N_1 = 1$, the approximated solution proposed here will lead to the exact minimum average system delay of the aggregated scheme because the requests reached in each queue are fully correlated.

3.4.3 Theoretical Analysis

Theorem 3. *Under our heterogeneous OSCNC-DSCNB network model, the aggregated scheme has a lower minimum average system delay than that of the non-aggregated scheme.*

Proof. The average system delays of the non-aggregated and the aggregated schemes are

$$E[D_{non\_agg}] = \frac{\alpha_1}{B_1^w/\mu_1 - \alpha_1\lambda_1} + \frac{1-\alpha_1}{B_1^v/\mu_1 - (1-\alpha_1)\lambda_1/N_1}$$

$$E[D_{agg}] = E[\max(D_{OSCNC}, D_{DSCNB})]$$

$$= E[D_{OSCNC}] + E[D_{DSCNB}] - E[\min(D_{OSCNC}, D_{DSCNB})]$$

Note that, for aggregated scheme,

$$E[D_{OSCNC}] = \frac{1}{\frac{B_1^w}{\beta_1\mu_1} - \lambda_1} = \frac{\beta_1}{\frac{B_1^w}{\mu_1} - \beta_1\lambda_1}$$

$$E[D_{DSCNB}] = \frac{1}{\frac{B_1^v}{(1-\beta_1)\mu_1} - \frac{\lambda_1}{N_1}} = \frac{1-\beta_1}{\frac{B_1^v}{\mu_1} - \frac{(1-\beta_1)\lambda_1}{N_1}}$$

When $\alpha_1 = \beta_1$, since $E[\min(D_{OSCNC}, D_{DSCNB})]$ is greater than zero, we always have $E[D_{non\_agg}] > E[D_{agg}]$. Therefore, the minimum average system delay of the aggregated scheme is lower than that of the non-aggregated scheme.

□

3.4.4 Empirical Analysis

When applying the approximation method, the following question should be addressed: is the resulting minimum average system delay with approximated β_1 of the aggregated scheme still lower than that of the non-aggregated scheme? To further investigate the comparison between the non-aggregated and the aggregated schemes, the analytical results reached when applying the non-aggregated scheme are compared with the simulation results reached when applying the approximated aggregated scheme. The ratio of the approximated minimum average system delay of the aggregated scheme to the

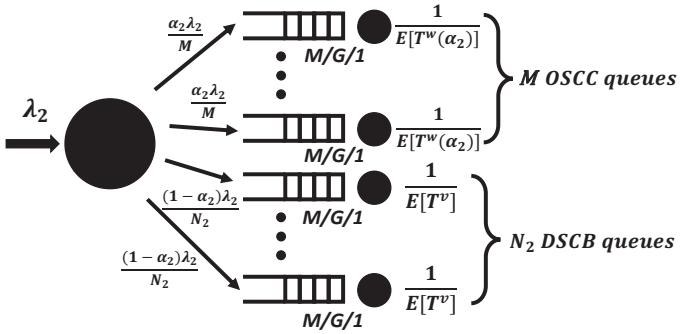

Figure 3.8 Queuing model representing the non-aggregated system model for heterogeneous OSCC-DSCB networks.

minimum average system delay of the non-aggregated scheme is used to demonstrate the practicability of the approximation approach. Figure 3.7 illustrates the comparison. The value settings of $\lambda_1, \mu_1, B_1^w, B_1^v$ and N_1 are the same as those in Figure 3.6. As such, based on the simulation parameters, the approximated minimum average system delay of the aggregated scheme is at least 16% lower than that of the non-aggregated scheme. The aggregation has diminishing gains over the non-aggregated scheme as the number of DSCNB APs increases and the ratio of OSCNC bandwidth to DSCNB bandwidth decreases. This is due to the additional OSCNC capacity which leads to decreasing the effect per DSCNB AP. Besides, the benefit of aggregating OSCNC and DSCNB becomes less evident as λ_1 and μ_1 increases. This is because increasing traffic load reduces the effect of efficient bandwidth utilization provided by aggregation.

3.5 System Delay Analysis for Heterogeneous OSCC-DSCB Network

In this section, we first model the system delay of the non-aggregated and the aggregated schemes for heterogeneous OSCC-DSCB networks. To validate our analytical model, we conduct extensive simulations based on the system model presented in Section 3.2. We

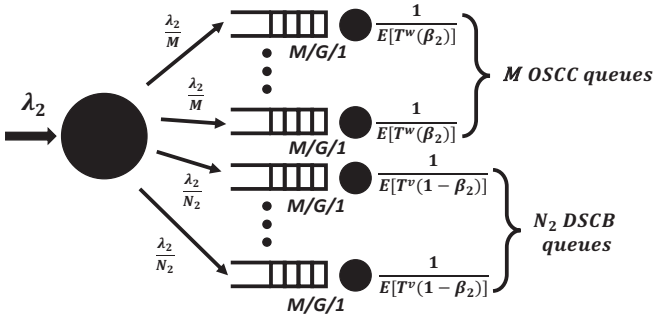

Figure 3.9 Queuing model representing the aggregated system model for heterogeneous OSCC-DSCB networks.

also observe from the simulation results that, under certain conditions, the non-aggregated scheme outperforms the aggregated one in terms of minimum average system delay.

3.5.1 The Non-aggregated Scheme

Let α_2 denote the percentage of requests allocated to OSCC. The non-aggregated scheme can be represented by the queuing model in Figure 3.8. Similar to the analysis for heterogeneous OSCNC-DSCNB networks, the request arrival process to each queue is still a Poisson process. However, since the contention and backoff of 802.11 protocols are considered when modeling the OSCC network, the service time of each OSCC queue $T^w(\alpha_2)$ depends on the traffic load allocated to OSCC. Also, for DSCB queues, due to the consideration of the blockage, the distribution of the service time of each request T^v is not memoryless. Therefore, the M/G/1 queuing model is utilized to characterize each OSCC and DSCB queue. In order to fully characterize the delay of the resulting M/G/1 model, we need to derive the expectation and the second moment of the service time of the resulting M/G/1 model.

The minimum and maximum contention window size associated with backoffs are denoted by CW_{min} and CW_{max}, respectively. The notation $m = \log_2(CW_{max}/CW_{min})$.

For instance, $CW_{min} = 16\ slots$ and $CW_{max} = 1024\ slots$, and thus $m = 6$ for 802.11n protocol. In the following analysis, since RTS/CTS exchange is considered, we denote the probability that an RTS transmission results in a collision by p. Following the same approach in [62], the average number of backoff slots experienced by a request at a OSCC AP can be expressed as

$$\bar{W} = \frac{1 - p - p(2p)^m}{1 - 2p} \frac{CW_{min}}{2}. \tag{3.6}$$

Denote the duration consumed by a collision by $T_c = DIFS + \sigma_{RTS}$, where Distributed Inter-Frame Space (DIFS) is utilized to sense the idle channel and $\sigma_{RTS} = l_{RTS}/B_2^w$ is the transmission delay of an RTS packet. Given the average request arrival rate as $\frac{\alpha_2\lambda_2}{M}$ and the average time to transmit a request in OSCC queue as $\frac{\mu_2}{B_2^w}$, the collision probability can be expressed as follows according to [62]

$$p = 1 - \left(1 - \frac{\frac{\alpha_2\lambda_2}{M}[1 + \frac{1}{\bar{W}}(\frac{\mu_2}{B_2^w} + T_c\frac{p}{2(1-p)})]}{1 - \frac{\alpha_2\lambda_2}{M}(M-1)[\frac{\mu_2}{B_2^w} + T_c\frac{p}{2(1-p)}]}\right)^{M-1}. \tag{3.7}$$

By substitute (3.6) into (3.7), the collision rate p can be obtained by numerical methods.

Denote the queue utilization rate of each OSCC AP as ρ, then according to [62], we have

$$\rho = \frac{\frac{\alpha_2\lambda_2}{M}[\frac{\mu_2}{B_2^w} + T_c\frac{p}{2(1-p)} + \bar{W}]}{1 - \frac{\alpha_2\lambda_2}{M}(M-1)[\frac{\mu_2}{B_2^w} + T_c\frac{p}{2(1-p)}]}.$$

Next, we start deriving the probability density function (pdf) of the request service time, which is from the instant that the request reaches the head to the queue to the instant that the request departs from the queue. The pdf of the backoff slots (BO), following a

successful transmission of a request at a OSCC AP, is represented by

$$P[BO = i] = \rho(1-p)U_{1,CW_{min}}(i) + p(1-p) \times [U_{1,CW_{min}} * U_{1,2CW_{min}}] + ...$$
$$+ (p)^m(1-p)[U_{1,CW_{min}} * U_{1,2CW_{min}} * ... * U_{1,2^mCW_{min}}](i)],$$

where $U_{a,b}$ denotes a uniform distribution between a and b, and $*$ represents the convolution operation.

To evaluate the portion of service time resulted from the successful transmissions and collisions of the contending OSCC APs, we denote q as the probability that one of the remaining $M-1$ OSCC APs attempts to transmit in a given slot, and q_c as the probability that a collision occurs in a slot given that at least one of the $M-1$ OSCC APs attempts to transmit in that slot. According to [62], we have

$$q = 1 - (1 - \frac{\rho}{\bar{W}})^{M-1},$$

and

$$q_c = \frac{1 - (1 - \frac{\rho}{\bar{W}})^{M-1} - \frac{(M-1)\rho}{\bar{W}}(1 - \frac{\rho}{\bar{W}})^{M-1}}{1 - (1 - \frac{\rho}{\bar{W}})^{M-1}}.$$

Assume that in the i backoff slots, j slots are followed by transmission attempts of the $M-1$ OSCC APs and k out of j slots are followed by collisions, then $j-k$ slots are followed by successful transmissions of the $M-1$ OSCC APs. Since the summation of $j-k$ i.i.d. exponential random variables (i.e., transmission time of a request $\frac{\mu_2}{B_2^w}$) is a gamma random variable, the contribution of $j-k$ successful transmissions to the service time can be expressed as a gamma distribution

$$l^{(j-k)}(x) = \frac{1}{(j-k-1)!\,(\frac{B_2^w}{\mu_2})^{j-k}} x^{j-k-1} e^{-\frac{\mu_2 x}{B_2^w}}.$$

Then the pdf of the channel access delay experienced by a request is given by

$$P[Y=s] = \sum_{i}^{\infty}\sum_{j}^{i}\sum_{k}^{j} l^{(j-k)}(x)\binom{i}{j}q^i(1-q)^{i-j} \times \binom{j}{k}q_c^k(1-q_c)^{j-k}P[BO=i]I(s), \tag{3.8}$$

where $\binom{i}{j}q^i(1-q)^{i-j}$ represents the probability that j out of i slots are followed by transmission attempt from the $M-1$ OSCC APs, $\binom{j}{k}q_c^k(1-q_c)^{j-k}$ represents the probability that k out of j slots are followed by collisions, and $I(s)$ is an indicator function which equals 1 when $s = x + i + kT_c$ and 0 otherwise.

Denote the moment generating function (mgf) of the channel access delay by $M_Y(t)$, the mgf of the total service time $M_R(t)$, including the channel access delay and request transmission time, is given by

$$M_R(t) = M_Y(t)(1 - t(\frac{B_2^w}{\mu_2})^{-1})^{-1},$$

where $(1 - t(\frac{B_2^w}{\mu_2})^{-1})^{-1}$ represents the mgf of an exponential random variable with mean $\frac{\mu_2}{B_2^w}$. Then the second moment and the mean of the total service time T^w can be obtained by differentiating $M_R(t)$ with respect to t and setting $t = 0$ as follows

$$E[(T^w)^2] = \frac{\mathrm{d}^2 M_R(t)}{\mathrm{d}t^2}(0),\ E[T^w] = \frac{\mathrm{d}M_R(t)}{\mathrm{d}t}(0).$$

According to Pollaczek-Khinchine formula, the expected system delay of OSCC queues is given by

$$E[D_{OSCC}] = \frac{\frac{\alpha_2\lambda_2}{M}E[(T^w)^2]}{2(1-\rho)} + E[T^w].$$

For DSCB queues, in order to fully characterize the average system delay of requests, we need to derive the expectation and the second moment of the service time of the resulting M/G/1 model. Recall that the probability of successful transmission is denoted by P_{succ} and packet drop due to buffer limitation is not considered. Although in some cases, a packet may be dropped after a certain number of unsuccessful retransmissions, the error caused by this infinite extension is negligible since $P_{succ}(1 - P_{succ})^{n-1} \to 0$ as n increases. Therefore, the expected service time of a request in DSCB queues is

$$\begin{aligned} E[T^v] =& \frac{\mu_2}{B_2^v}[P_{succ} + 2P_{succ}(1 - P_{succ}) + ... + nP_{succ}(1 - P_{succ})^{n-1} + ...] \\ =& \frac{\mu_2}{B_2^v P_{succ}}. \end{aligned}$$

Suppose a request's transmission time is v and unsuccessful transmission times is u, then the total service time of this request is uv. Thus, the second moment of the service time of a request in DSCB queues is

$$E[(T^v)^2] = \sum_{v}^{\infty} \sum_{u}^{\infty} \frac{B_2^v}{\mu_2} e^{-\frac{B_2^v}{\mu_2} v} P_{succ}(1 - P_{succ})^{u-1}(uv)^2.$$

According to Pollaczek-Khinchine formula, the expected system delay of DSCB queues is given by

$$E[D_{DSCB}] = \frac{\frac{(1-\alpha_2)\lambda_2}{N_2} E[(T^v)^2]}{2(1 - \frac{(1-\alpha_2)\lambda_2}{N_2} E[T^v])} + E[T^v].$$

Since α_2 traffics are allocated to OSCC networks and $1 - \alpha_2$ traffics are allocated to DSCB networks, the average system delay of the heterogeneous OSCC-DSCB networks

based on the non-aggregated scheme is given by

$$D_{non\_agg} = \alpha_2 E[D_{OSCC}] + (1 - \alpha_2) E[D_{DSCB}].$$

3.5.2 The Aggregated Scheme

Let β_2 denote the proportion of the size of each request that is allocated to the OSCC. The aggregated scheme can be represented by the queuing model in Figure 3.8. Similar to the non-aggregated scheme for heterogeneous OSCC-DSCB networks, the request arrival process of each OSCC or DSCB queue can be described by a Poisson process, and the distribution of service time are not memoryless for both OSCC and DSCB queues. Therefore, we use the M/G/1 queuing model to characterize each OSCC and DSCB queue.

For the derivation of the system delay for the aggregated scheme, we only describe the parameters p, ρ, $l^{(j-k)}(x)$, $M_R(t)$, $E[D_{OSCC}]$, $E[T^v]$, $E[(T^v)^2]$ and $E[D_{DSCB}]$ with different expressions when comparing them to those of the non-aggregated scheme. Given the average request arrival rate of OSCC queues as $\frac{\lambda_2}{M}$ and the average time to transmit a request in OSCC queue as $\frac{\beta_2 \mu_2}{B_2^w}$, the collision probability, queue utilization and the contribution of $j - k$ successful transmissions to the service time can be expressed as follows

$$p = 1 - \left(1 - \frac{\frac{\lambda_2}{M}[1 + \frac{1}{\bar{W}}(\frac{\beta_2 \mu_2}{B_2^w} + T_c \frac{p}{2(1-p)})]}{1 - \frac{\lambda_2}{M}(M-1)[\frac{\beta_2 \mu_2}{B_2^w} + T_c \frac{p}{2(1-p)}]} \right)^{M-1}, \tag{3.9}$$

$$\rho = \frac{\frac{\lambda_2}{M}[\frac{\beta_2 \mu_2}{B_2^w} + T_c \frac{p}{2(1-p)} + \bar{W}]}{1 - \frac{\lambda_2}{M}(M-1)[\frac{\beta_2 \mu_2}{B_2^w} + T_c \frac{p}{2(1-p)}]}, \tag{3.10}$$

$$l^{(j-k)}(x) = \frac{1}{(j-k-1)!\,(\frac{B_2^w}{\beta_2 \mu_2})^{j-k}} x^{j-k-1} e^{-\frac{\beta_2 \mu_2 x}{B_2^w}}. \tag{3.11}$$

Substitute equations (3.9), (3.10) and (3.11) into (3.8), the pdf of the channel access delay can be obtained. Then the mgf of the total service time is expressed as follows

$$M_R(t) = M_Y(t)(1 - t(\frac{B_2^w}{\beta_2\mu_2})^{-1})^{-1}.$$

Similar to the non-aggregated scheme, the expected service time of a request in OSCC queues is

$$E[D_{OSCC}] = \frac{\frac{\lambda_2}{M}E[(T^w)^2]}{2(1-\rho)} + E[T^w].$$

For DSCB queues, the expectation and the second moment of the service time are

$$E[T^v] = \frac{\beta_2\mu_2}{B_2^v P_{succ}} \text{ and}$$
$$E[(T^v)^2] = \sum_{v}^{\infty}\sum_{u}^{\infty} \frac{B_2^v}{\beta_2\mu_2} e^{-\frac{B_2^v}{\beta_2\mu_2}v} P_{succ}(1-P_{succ})^{u-1}(uv)^2.$$

The expectation of the system delay of the DSCB queues is

$$E[D_{DSCB}] = \frac{\frac{\lambda_2}{N_2}E[(T^v)^2]}{2(1-\frac{\lambda_2}{N_2}E[T^v])} + E[T^v].$$

Similar to the approximation for the aggregated scheme in heterogeneous OSCNC-DSCNB networks, the average system delay of the heterogeneous OSCC-DSCB networks based on the aggregated scheme is estimated by

$$D_{agg} = \begin{cases} E[D_{OSCC}], \text{ if } E[D_{OSCC}] \geq E[D_{DSCB}], \\ E[D_{DSCB}], \text{ otherwise.} \end{cases}$$

3.5.3 Empirical Analysis

To validate our analytical model and compare the system delay performance of heterogeneous OSCC-DSCB networks under non-aggregated and aggregated schemes, we

Table 3.2 System Settings

Number of OSCC APs	10
OSCC bandwidth	20 Mbps
Minimum contention window	16
Maximum contention window	1024
RTS size	44 bytes
CTS size	38 bytes
DIFS	50 μsec
Slot size	20 μsec
Number of DSCB APs	20
DSCB bandwidth	10 Mbps
P_{succ} of DSCB	0.5
request arrival rate	0.05/slot
mean request size	1000 bytes

conducted extensive simulations under the homogeneous traffic assumptions. The final system delay is averaged over the delay of 100,000 simulated requests. All the parameter settings for OSCC and DSCB networks are given in Table 3.2.

In Figure 3.10, we vary the traffic allocation ratio α_2 for the non-aggregated scheme and the request splitting ratio β_2 for the aggregated scheme, and compare the simulation and analytical results for the average system delay. For both schemes, we can see the close match between the analytical and simulation results. As expected, there exist optimal values of α_2 and β_2 that will lead to the minimum average system delay of the heterogeneous OSCC-DSCB network. With α_2 and β_2 lower than the optimal values, the DSCB network will contribute more delay penalty to the average system delay. However, since the contention and backoff mechanism is not considered in DSCB, the average system delay will not approach to infinity even if α_2 and β_2 equal to 0. In contrast, as the α_2 and β_2 increase above the optimal value, the OSCC queues will be saturated quickly, which leads to infinite average system delay.

In Figure 3.11, the values of the $\lambda_2, \mu_2, B_2^w, B_2^v$ are initially set as the values in Table 3.2. In each plot, one of these four parameters is varied while keeping the other three

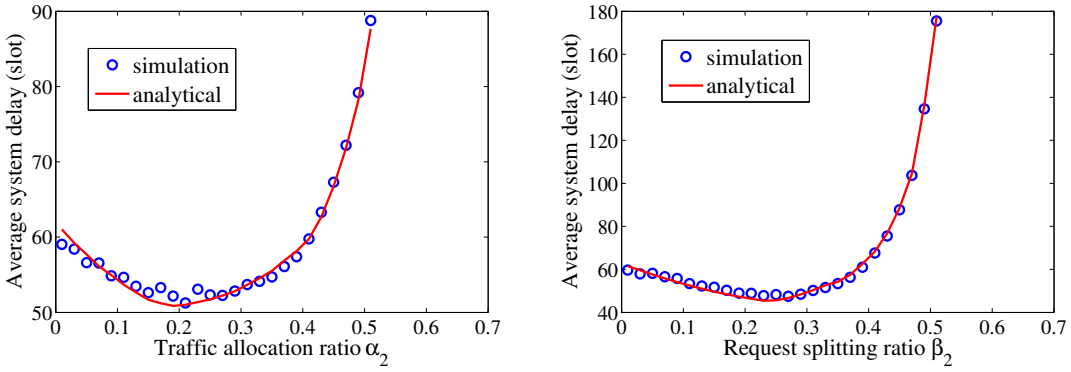

(a) non-aggregated scheme **(b)** aggregated scheme.

Figure 3.10 Comparison of the average system delays for (a) non-aggregated scheme; (b) aggregated scheme.

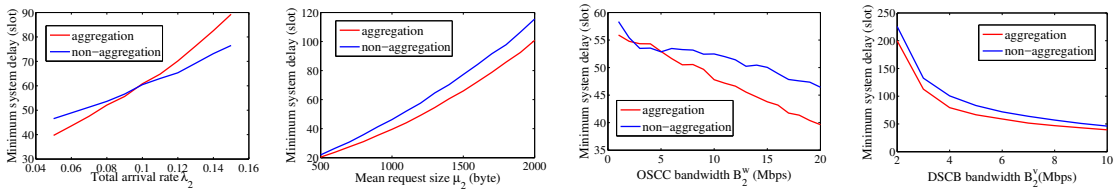

(a) λ_2 **(b)** μ_2 **(c)** B_2^w **(d)** B_2^v

Figure 3.11 Comparison between the average system delays of non-aggregated scheme and aggregated scheme in terms of (a) λ_2; (b) μ_2; (c) B_2^w; (d) B_2^v, when $M = 10$ and $N_2 = 20$.

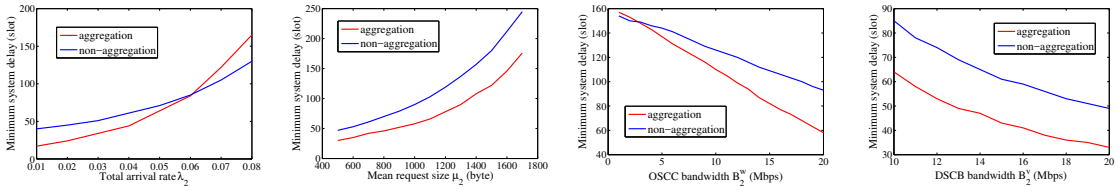

(a) λ_2 **(b)** μ_2 **(c)** B_2^w **(d)** B_2^v

Figure 3.12 Comparison between the average system delays of non-aggregated scheme and aggregated scheme in terms of (a) λ_2; (b) μ_2; (c) B_2^w; (d) B_2^v, when $M = 2$ and $N_2 = 4$.

fixed at the initial values. In Figure 3.11 (a), it is observed that the average system delay of aggregated scheme is not always lower than that of the non-aggregated scheme. This is the major difference from the simulation results of heterogeneous OSCNC-DSCNB networks, where contention and backoff mechanism is not considered. As the request arrival rate increases, the backoff penalty brought by aggregation will surpass the benefit from splitting the requests. Therefore, in heterogeneous networks where contention and backoff mechanism is applied, under certain conditions, the non-aggregated scheme outperforms the aggregated scheme in terms of average system delay. In Figure 3.11 (b), as the mean request size increases, the gap between aggregation and non-aggregation increases. These results are opposite to the results of Figure 3.7 (b). The reason is that as the mean request size decreases, the benefit brought from aggregation becomes less evident than the backoff penalty. In Figure 3.11 (c) and Figure 3.11 (d), the results are consistent to the results of Figure 3.7 (c) and (d). As the OSCC bandwidth increases, the collision probability of the OSCC network is decreasing. Thus, the delay penalty effect brought by aggregation is weakening. As the DSCB bandwidth increases, similar to the heterogeneous OSCNC-DSCNB network, the benefit gain of aggregated scheme is slightly reducing. This is because the incrementing DSCB bandwidth leads to smaller optimal α_2 and β_2, which will reduce the gap between the delay performance of non-aggregated scheme and aggregated scheme.

To evaluate the effect of the number of APs on the system delay performance of the heterogeneous OSCC-DSCB network, we reduce the number of OSCC APs M from 10 to 2 and the number of DSCB APs N_2 from 20 to 4. The comparisons between non-aggregated scheme and aggregated scheme in terms of $\lambda_2, \mu_2, B_2^w, B_2^v$ are performed

again and the simulation results are shown in Figure 3.12. Compared to the simulation results when $M = 10$ and $N_2 = 20$, the average system delays are higher when $M = 2$ and $N_2 = 4$. This is because the total network capacity is reduced when the number of APs decreases. We also observe that when $M = 10$ and $N_2 = 20$, the benefit gain of aggregated scheme over non-aggregated scheme is less than 20%; while this benefit gain increases up to 40% when $M = 2$ and $N_2 = 4$. The reason for this increasing benefit gain of aggregated scheme as the number of APs decreasing is that, with certain value of total request arrival rate, mean request size and OSCC bandwidth, the collision probability of OSCC network is decreasing as the number of OSCC APs decreases. In particular, the backoff penalty of aggregated scheme is decreasing as the number of OSCC APs decreases. Therefore, the benefit gain of aggregated scheme over non-aggregated scheme becomes dominant when the number of OSCC APs is small.

3.6 Related Work

Many current research efforts have been paid towards developing heterogeneous networks incorporating both OSC and DSC. A protocol, considering OFDMA, vertical handover (VHO) and horizontal handover (HHO) mechanisms for mobile terminals (MTs) to enable the mobility of users among different VLC APs and OFDMA system, is proposed in [63]. The authors define a new metric, called spatial density, to evaluate the capacity of the heterogeneous network under the assumption of the Homogenous Poisson Point Process (HPPP) distribution of MTs. In [64], load balancing for hybrid VLC and WiFi system is optimized by both centralized and distributed resource-allocation algorithms while achieving proportional fairness. In [65], different RF-VLC hetero-

geneous network topologies, such as symmetric non-interfering, symmetric with interference and asymmetric, are briefly discussed. In [66], taking the advantage of wide coverage of RF and spatially reuse efficiency of VLC, a hybrid RF and VLC system is proposed to improve per user average and outage throughput.

Regarding the bandwidth aggregation, a thorough survey of approaches in heterogeneous wireless networks has been presented in [11]. The challenges and open research issues in the design of bandwidth aggregation system, ranging from MAC layer to application layer, have been investigated in detail. The benefits of bandwidth aggregation includes increased throughput, improved packet delivery, load balancing and seamless connectivity. This work also validates the feasibility of the heterogeneous OSC-DSC networks proposed here based on bandwidth aggregation. In [67], users connect to WiFi and VLC simultaneously. A parallel transmission MAC (PT-MAC) protocol containing CSMA/CA algorithm and the concept of parallel transmission are proposed. This protocol supports fairness among users in the hybrid VLC and WLAN network.

In [5], delay modeling of a hybrid WiFi-VLC system has been investigated. Each WiFi and VLC queue is observed as an M/D/1 queue, and the capacities with respect to the unstable delay points of WiFi only, asymmetric WiFi-VLC and hybrid WiFi-VLC systems are compared. An analytic model for evaluating the queueing delays and channel access times at nodes in 802.11 based WiFi networks is presented in [62]. The model provides closed form solutions for obtaining the values of the delay and queue length. This is done by modeling each node as a discrete time G/G/1 queue. However, these works do not investigate the delay modeling of a system with bandwidth aggregation. In other words,

most of the existing heterogeneous works only study the networks without bandwidth aggregation (i.e., one request is either forwarded to one access technology or the other).

3.7 Conclusion

In this chapter, two cases of heterogeneous OSC-DSC wireless networks are considered for aggregation and non-aggregation schemes. In the first case, the heterogeneous OSCNC-DSCNB network is investigated. Given the assumptions that requests arrive as a Poisson process and the request size is exponentially distributed, it is proved that the minimum average system delay of the aggregated scheme is always lower than that of the non-aggregated scheme. An efficient method is proposed to approximate the optimal requests splitting ratio in the aggregated scheme. The analytical results when applying the non-aggregated scheme and simulation results when applying the aggregation system are also presented. In the second case, the heterogeneous OSCC-DSCB network is studied. The average system delay is derived for both the non-aggregated and aggregated schemes. Extensive simulation results imply that, when contention and backoff mechanism is considered, the non-aggregated scheme outperforms the aggregated one under certain conditions.

CHAPTER 4

POWER OPTIMIZATION OF VLC-BASED INDOOR ACCESS NETWORKS

4.1 Introduction

In this chapter [1], we investigate the problem of *optimizing total power consumption of a general multi-user VLC indoor network while satisfying the traffic demands and the illumination requirements*. A novel algorithm is proposed to efficiently obtain a practical ϵ-bounded solution. Our contributions are summarized as follows:

- **Minimizing the total power consumption for a general multi-user VLC indoor network:** Taking the users' traffic demand and the illumination requirement of entire horizontal space into account, the total power consumption of a general multi-user VLC indoor network is optimized via a novel efficient and practical algorithm.
- **Effectively model the level of interference among VLC links:** Based on the proposed algorithm, an effective interference management approach is verified by extensive simulation results.
- **Design of a novel structure of light source:** An innovative configuration of light source is proposed and analyzed, and compared with two other common configurations in terms of total power consumption.
- **Validating the power efficiency and illumination satisfaction:** Extensive simulation results reveal that, our proposed link scheduling algorithm can provide around 60% and 80% saving in power consumption compared to two VLC-based solutions, and the illumination distribution obtained by our proposed algorithm can always satisfy the requirements.

[1] The work of this chapter has been published in [49]

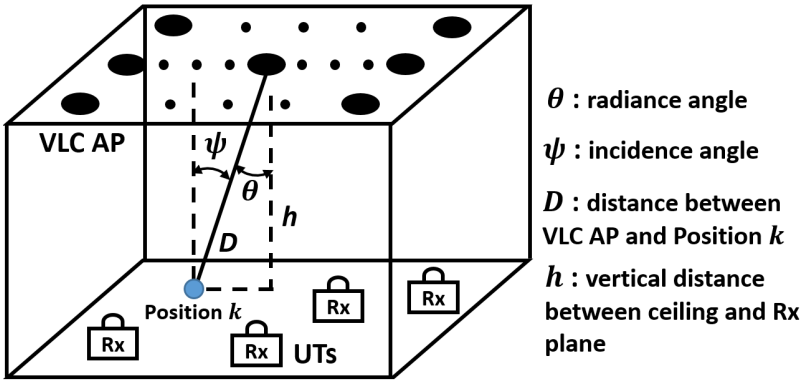

Figure 4.1 System model for multi-user VLC indoor network.

4.2 System Model

4.2.1 Access System Model

Consider a visible light access system model (Figure 4.1) comprising of $\mathcal{V} = \{1, 2, ..., i, ..., V\}$ VLC APs, $\mathcal{M} = \{1, 2, ..., j, ..., M\}$ user terminals (UTs), and $\mathcal{W} = \{1, 2, ..., b, ..., W\}$ available channels with different bandwidths. The bandwidth of channel b is denoted by B^b. We also denote the set of transmitters on VLC AP $i \in \mathcal{V}$ by $Tx_i = \{1, 2, ..., m, ..., |Tx_i|\}$, where $|Tx_i|$ is the number of transmitters on VLC AP i, and the set of receivers on UT $j \in \mathcal{M}$ by $Rx_j = \{1, 2, ..., n, ..., |Rx_j|\}$, where $|Rx_j|$ is the number of receivers on UT j. We assume the UT j has a throughput requirement $\mathcal{R}_j$.

A recent measurement study [51] on traces of 3785 smart phone users from 145 countries over a four-month period shows that the ratio of WiFi download traffic to its upload traffic is 20:1. Therefore, in this chapter, we mainly consider the power consumption for the downlink data transmission. Regarding the uplink issue in VLC network, a hybrid WiFi-VLC Internet access system (VLC downlink and WiFi uplink) is presented in our earlier work [35, 37, 68].

4.2.2 Communication

Optical modulation is performed by varying the forward current of the light source. The output optical power changes proportionally to the modulated forward current. The increase in total power consumption (including the power consumed by modulator) is mainly due to the switching loss in the driver circuitry at high speed (AC current for modulation). Such behavior is observed in our preliminary experimental results and the results in [69]. Here, we denote a peak-to-peak optical signal strength (generated from AC current) by P_{AC} and its average value by $P_{AC,Avg}$.

4.2.3 Illuminance

Consider a horizontal user plane comprising of $\mathcal{K} = \{1, 2, ..., k, ..., K\}$ positions and each position requires an illumination level in the range of E_k^L and E_k^U. The illumination level of ambient light at position k is denoted by E_k^{Am}.

The illumination level at a given location depends on the average optical power received. This can be generated by both the DC and the AC current. We denote an optical DC power (generated from DC current) by P_{DC}, which is responsible for compensating the average AC power in order to meet the illumination demands.

The DC component does not require a current switching process. This switching process reduces the efficiency of the driver circuit and light source by consuming more power. Thus, for the transmitter m of the i^{th} VLC AP, we denote $\eta_{AC}^{i,m}$ and $\eta_{DC}^{i,m}$ as the wall plug efficiency factors (i.e., the ratio of the optical power consumption to the electrical power consumption) for AC and DC optical power, respectively, where $\eta_{AC}^{i,m}$ is generally smaller than $\eta_{DC}^{i,m}$.

The illuminance represents the level of brightness of the illuminated surface. A horizontal illuminance E_k [lux] at position k, can be given [70] as

$$E_k = \sum_{i \in \mathcal{V}} \sum_{m \in Tx_i} (P_{DC}^{i,m} g_{i,k,m}^{DC} + P_{AC,Avg}^{i,m} g_{i,k,m}^{AC}) \rho,$$

where $P_{DC}^{i,m}$ and $P_{AC,Avg}^{i,m}$ denote the generated DC and average AC optical power from the transmitter m of the i^{th} VLC AP, respectively, ρ [lm/W] is the luminosity efficacy, and $g_{i,k,m}^{DC}$ and $g_{i,k,m}^{AC}$ are given as follows

$$g_{i,k,m}^{DC} = \frac{ml_{DC}+1}{2\pi D^2} cos^{ml_{DC}}(\theta_{DC}) cos(\psi)$$
$$g_{i,k,m}^{AC} = \frac{ml_{AC}+1}{2\pi D^2} cos^{ml_{AC}}(\theta_{AC}) cos(\psi)$$

where ml is the Lambertian order ($ml = -ln2/ln(cos\theta_{1/2})$, $\theta_{1/2}$ is the semi-angle at half power), (in Figure 4.1) D is the distance between VLC AP i and position k, θ is the radiance angle, and ψ is the incidence angle. Note that, the ml and θ of the DC and AC powered source could be different, which will be discussed in detail in Section 4.5.

4.2.4 Channel Capacity, Interference and Noise

From [3], the received optical intensity via a line-of-sight (LOS) path is about 30 times higher than that via the first reflective path. Since LOS paths are typically feasible, in this chapter, we only consider the LOS links. The LOS channel gain between VLC AP i, using transmitter m, and UT j, using receiver n, denoted by $H_{ij,mn}$, is illustrated in [3].

It is worth noticing that, the gain of VLC channel highly depends on the strict alignment between VLC transceivers. In contrast to the omnidirectional WiFi channel, the potential motion of users will lead to severe degradation of VLC channel gain.

Nevertheless, according to [71], most of the Internet access traffic will happen indoor at fixed locations. Thus, we focus on scenarios that the users' location are fixed, where the channel gain of VLC is more stable than that of WiFi [72].

The Gaussian noise of the optical wireless channel consists of the shot noise (stems from the received optical power) and the thermal noise (stems from the receiver's circuitry). Increasing the transmitted optical power increases the noise level at the receiver. However, if the modulation bandwidth is large (above 50 MHz) and the optical power level is low (below 20 W) as is the case with most VLC APs and VLC front-ends [73], the thermal noise would dominate the shot noise [3]. With fixed gain of the receiver, the thermal noise is essentially independent of the ambient light and signal strength while the shot noise is not. Our experimental results [35] have validated this behavior even in outdoor settings. Therefore, a constant variance of Gaussian noise can be assumed.

Typically, there are two major interference models for the wireless networks [74]: Physical Model and Protocol Model. Under Physical Model, the link capacity depends on the signal-to-interference-plus-noise ratio (SINR) at the receiver side. It is a very accurate representation of real scenarios, but it is computationally difficult to work with. On the other hand, Protocol Model only considers the pairwise interference relationship among the links. With Protocol Model, the interference among individual VLC links can be modeled through the use of a conflict graph [75]. The approach works as follows. Each receiver on a UT or each transmitter on a VLC AP is represented by a vertex in a graph. If a transmitter can transmit to a receiver on a given channel, an edge is drawn between the two vertices representing the transmitter and the receiver. The conflict graph is then constructed, such that each edge in the original graph is represented by a vertex

in the conflict graph. An edge in the conflict graph is drawn between two vertices, if the corresponding edges in the original graph interfere with each other. An interference constraint (addressed in details in Section 4.4) represents the fact that for a successful transmission (i.e., vertex in the conflict graph), none of those vertices (i.e., links in the original graph) connected by an edge in the conflict graph are active at the same time. Based on this interference constraint, the link capacity depends on the signal-to-noise ratio (SNR) under Protocol Model.

Given a link with bandwidth B^b, based on Shannon-Hartley theorem [76], the maximum link capacity C when VLC AP i, using transmitter m, transmits data to UT j, using receiver n, on channel b, in two interference models are given [77] by

$$C^b_{ij,mn}(Protocol) = B^b \times log_2(1 + \frac{(\gamma H_{ij,mn} P^{i,m}_{AC})^2}{N}) \tag{4.1}$$

$$C^b_{ij,mn}(Physical) = B^b \times log_2(1 + \frac{(\gamma H_{ij,mn} P^{i,m}_{AC})^2}{(\gamma P_I)^2 + N}) \tag{4.2}$$

where γ is the detector responsivity, P_I is the summation of interference optical power and N is the variance of noise.

4.3 Problem Formulation

We investigate the minimum power consumption problem for a multi-user VLC indoor network by joint link scheduling and illuminating. For a conflict graph under Protocol Model, an *independent set* (IS) $\mathcal{I}$ is defined as a set of vertices in the conflict graph (i.e., links in the original graph) such that none of them are connected by an edge [75].

Suppose all the ISs are known and the set of all ISs is denoted as $\mathcal{Q} = \{\mathcal{I}_1, \mathcal{I}_2, ..., \mathcal{I}_q, ..., \mathcal{I}_{|\mathcal{Q}|}\}$. In order to ensure the successful transmissions in each IS, at any

given time, only one IS should be active. We define ω_q as the fraction of the time during which the q^{th} IS is active. Therefore, we have

$$\sum_{1\leq q\leq|\mathcal{Q}|}\omega_q\leq 1,\ \omega_q\geq 0 \tag{4.3}$$

An integer variable is defined as follows: $x_{ij,mn}^{q,b}$ is equal to 1 if VLC AP i, using transmitter m, transmits to UT j, using receiver n, on channel b, in $\mathcal{I}_q$, and equal to 0 otherwise.

Recall that the j^{th} UT's throughput requirement is $\mathcal{R}_j$. In order to meet the traffic demands of users, the following set of constraints need to be satisfied

$$\sum_{1\leq q\leq|\mathcal{Q}|}\omega_q\sum_{i\in\mathcal{V}}\sum_{b\in\mathcal{W}}\sum_{m\in Tx_i}\sum_{n\in Rx_j}\mathcal{C}_{ij,mn}^{b}x_{ij,mn}^{q,b}\geq\mathcal{R}_j\ (\forall j\in\mathcal{M})$$

where $\mathcal{C}_{ij,mn}^{b}$ is calculated by (1).

Denote $P_{DC}^{i,q,m}$ as the i^{th} VLC AP's DC optical power consumption of the transmitter m in the q^{th} IS and $P_{AC}^{i,m}$ as the fixed peak-to-peak signal strength of i^{th} VLC AP's transmitter m. For one VLC transmitter, the summation of P_{AC} and P_{DC} can not exceed the maximum optical power P_{max}. Thus we have

$$P_{DC}^{i,q,m}+\sum_{j\in\mathcal{M}}\sum_{b\in\mathcal{W}}\sum_{n\in Rx_j}P_{AC}^{i,m}x_{ij,mn}^{q,b}\leq P_{max}^{i,m}\ (\forall i\in\mathcal{V},\forall m\in Tx_i,1\leq q\leq|\mathcal{Q}|)$$

Recall that, at position k, the minimum and maximum illuminance thresholds are E_k^L and E_k^U, respectively, and the illuminance level of ambient light is E_k^{Am}. The summation of the LED lighting and the ambient lighting needs to be within the range

$[E_k^L, E_k^U]$. Therefore, we have the following illumination constraints

$$E_k^U \geq \sum_{i\in\mathcal{V}}\sum_{j\in\mathcal{M}}\sum_{b\in\mathcal{W}}\sum_{m\in Tx_i}\sum_{n\in Rx_j}(P_{AC,Avg}^{i,m}x_{ij,mn}^{q,b}g_{i,k,m}^{AC,q} + \quad P_{DC}^{i,q,m}g_{i,k,m}^{DC})\rho + E_k^{Am} \geq E_k^L$$

$$(\forall k \in \mathcal{K}, 1 \leq q \leq |\mathcal{Q}|) \tag{4.4}$$

The reason for adding the superscript q to the AC optical power gain is that, the Lambertian order or the radiance angle of the AC powered source on each VLC transmitter may be varied in different IS. This condition will be demonstrated in details in Section 4.5.

Given the link scheduling in each IS, the illuminance distribution from the average AC optical power can be obtained. Therefore, to satisfy the maximum power constraint (5) and the illumination constraint (6), we can compute the optimal $P_{DC}^{i,q,m}$ for each VLC transmitter in each IS. Denote $P_{AC,Avg}(\mathcal{I}_q)$ and $P_{DC}(\mathcal{I}_q)$ as the total AC and DC power consumption of the q^{th} IS, respectively. The optimal solution of our algorithm might result in $\sum_{1\leq q\leq|\mathcal{Q}|}\omega_q < 1$, this means that the data transmission will be completed within the $\sum_{1\leq q\leq|\mathcal{Q}|}\omega_q$ fraction of time. However, the illumination is always needed. Let P_{illumi}^{min} represent the minimum total power consumption when all the VLC APs only perform illumination. This means that during the $(1 - \sum_{1\leq q\leq|\mathcal{Q}|}\omega_q)$ fraction of time, the power consumption is P_{illumi}^{min}. Therefore, the total power consumption optimization problem can be formulated as follows

$$\min_{\omega_q} \sum_{1\leq q\leq|\mathcal{Q}|}\omega_q[P_{AC,Avg}(\mathcal{I}_q) + P_{DC}(\mathcal{I}_q)] + (1 - \sum_{1\leq q\leq|\mathcal{Q}|}\omega_q)P_{illumi}^{min}$$

$$s.t.\ (3), (4)$$

Given that all the ISs satisfying constraints (5) and (6), the formulated optimization problem is a linear programming problem. We call this problem the *master problem* (MP). The solution to the MP is to find the optimal values of ω_q ($1 \leq q \leq |\mathcal{Q}|$). In Section 4.4, we will introduce the challenges of solving the MP and our solution methodology.

4.4 Solution Methodology

4.4.1 Challenges of Solving MP

To efficiently solve the MP, there are two main challenges: i) Although the MP is a linear programming problem if all the ISs are given, the IS decision problem itself is NP-complete [75] and hence it is believed that there is no efficient algorithm for solving it. ii) Even if all the ISs are given, the number of ISs and corresponding variables increases exponentially as the number of links increases. Therefore, the complexity of solving the MP will be extremely high when the network is very large. We propose a column generation based ϵ-bounded approximation algorithm to resolve these challenges.

4.4.2 Column Generation

Column generation [78] is an efficient algorithm for solving large scale (i.e., the number of variables is large) linear programming problem. Even though the MP has a large number of variables, only a small subset of them will be non-zero (basis variables) in the optimal solution. Based on this observation, rather than adding all the variables in the MP, column generation only generates the variables with the highest potential to enhance the objective function. In particular, the large MP is split into two smaller and simpler problems: *restricted master problem* (RMP) and *pricing problem* (PP). The RMP only includes an

initial subset of variables in the MP, and the PP is a new optimization problem assigned to find a variable or a column (i.e., independent set) that has the most negative reduced cost (i.e., decrease of the objective value). The process works iteratively as follows: the RMP is solved and its optimal and dual optimal solutions are obtained; the PP utilizes the dual optimal solution of the RMP to identify the column with the most negative reduced cost and adds it into RMP to re-optimize RMP. The process continues until the objective value of PP is non-negative. If the PP returns a non-negative solution, the solution of RMP is the optimal solution to the MP.

Instead of considering the set $\mathcal{Q}$ of all the ISs, RMP starts with an initial set $\tilde{\mathcal{Q}}$ of ISs (called observed ISs). A simple method of selecting the initial ISs is to place only one active link in each of them. Hence, the RMP is formulated as follows

$$\min_{\omega_q} \sum_{1\le q\le|\tilde{\mathcal{Q}}|} \omega_q[P_{AC,Avg}(\mathcal{I}_q)+P_{DC}(\mathcal{I}_q)]+(1-\sum_{1\le q\le|\tilde{\mathcal{Q}}|}\omega_q)P_{illumi}^{min}$$

$$s.t. \sum_{1\le q\le|\tilde{\mathcal{Q}}|}\omega_q\sum_{i\in\mathcal{V}}\sum_{b\in\mathcal{W}}\sum_{m\in Tx_i}\sum_{n\in Rx_j}\mathcal{C}_{ij,mn}^{b}x_{ij,mn}^{q,b}\ge R_j\ (\forall j\in\mathcal{M})$$

$$\sum_{1\le q\le|\tilde{\mathcal{Q}}|}\omega_q\le 1,\ \omega_q\ge 0$$

where $P_{DC}(\mathcal{I}_q)$ $(1\le q\le|\tilde{\mathcal{Q}}|)$ can be computed optimally by satisfying the maximum power constraint (5) and the illumination constraint (6).

After solving the RMP, the primal optimal solution and the Lagrangian dual optimal solution can be obtained. Since the ISs in RMP is only a subset of the ISs in MP (i.e., $\tilde{\mathcal{Q}}\subseteq\mathcal{Q}$), the primal optimal solution of RMP can be regarded as an upper bound of the optimal solution of MP. Adding another column, which does not exist in RMP, may reduce

the upper bound and improve the objective function. Therefore, the PP is responsible for generating a column with the most negative reduced cost.

For a IS that has not been observed (i.e., included in the RMP), the PP needs to determine whether the reduced cost of the IS is negative or not. Referring to [78], the reduced cost of $\mathcal{I}_q$ can be calculated as $c_r(\mathcal{I}_q) - P_{illumi}^{min}$, where

$$c_r(\mathcal{I}_q) = \sum_{i\in\mathcal{V}}\sum_{j\in\mathcal{M}}\sum_{b\in\mathcal{W}}\sum_{m\in Tx_i}\sum_{n\in Rx_j}(\frac{1}{\eta_{AC}^{i,m}}P_{AC,Avg}^{i,m}x_{ij,mn}^{b}+ \frac{1}{\eta_{DC}^{i,m}}P_{DC}^{i,m}) - \sum_{j\in\mathcal{M}}\lambda_j\sum_{i\in\mathcal{V}}\sum_{b\in\mathcal{W}}\sum_{m\in Tx_i}\sum_{n\in Rx_j}\mathcal{C}_{ij,mn}x_{ij,mn}^{b}$$

where λ_j is the Lagrangian dual optimal solution for the j^{th} UT. To find the $\mathcal{I}_q$ with the most negative reduced cost, the objective of PP is to minimize $c_r(\mathcal{I}_q) - P_{illumi}^{min}$.

Regarding the constraints of PP, under Protocol Model, we denote $\mathcal{T}_{ij,mn}^{b}$ as the set of links that interfere with the transmission from the i^{th} AP, using transmitter m, to the j^{th} UT, using receiver n, on channel b. Thus, we have

$$x_{ij,mn}^{b} + \sum_{pq,uv\in\mathcal{T}_{ij,mn}} x_{pq,uv}^{b} \leq 1 \ (\forall i \in \mathcal{V}, \forall j \in \mathcal{M}, \forall m \in Tx_i, \forall n \in Rx_j) \tag{4.5}$$

In addition, the total number of transmitting links at VLC AP i and receiving links at UT j should be no larger than $|Tx_i|$ and $|Rx_j|$, respectively, which means

$$\sum_{j\in\mathcal{M}}\sum_{b\in\mathcal{W}}\sum_{m\in Tx_i}\sum_{n\in Rx_j} x_{ij,mn}^{b} \leq |Tx_i| \ (\forall i \in \mathcal{V}) \tag{4.6}$$

$$\sum_{i\in\mathcal{V}}\sum_{b\in\mathcal{W}}\sum_{m\in Tx_i}\sum_{n\in Rx_j} x_{ij,mn}^{b} \leq |Rx_j| \ (\forall j \in \mathcal{M}) \tag{4.7}$$

Besides, a transmitter of a VLC AP can not transmit to multiple UTs and a receiver of a UT can not receive from multiple VLC APs due to interference. Therefore, we get

$$\sum_{j\in\mathcal{M}}\sum_{b\in\mathcal{W}}\sum_{n\in Rx_j} x^b_{ij,mn} \leq 1 \ (\forall i \in \mathcal{V}, \forall m \in Tx_i) \tag{4.8}$$

$$\sum_{i\in\mathcal{V}}\sum_{b\in\mathcal{W}}\sum_{m\in Tx_i} x^b_{ij,mn} \leq 1 \ (\forall j \in \mathcal{M}, \forall n \in Rx_j) \tag{4.9}$$

It is worth noticing that, in contrast to RF communication, the optical signal propagation may not be isotropic from the perspective of UTs plane (e.g., the central luminous flux is not vertical to the horizontal UTs plane), and also the orientation and filed of view (FOV) of VLC receiver can be tuned in order to receive signals from a specific direction and a small range. Thus, using the same channel, a transmitter of a VLC AP can transmit to multiple UTs, and a UT can receive from multiple VLC APs.

Assembling together the constraints of power and brightness control with the above constraints, the PP can be formulated as follows:

$$\min_{\mathcal{I}_q\in\mathcal{Q}\setminus\tilde{\mathcal{Q}}} c_r(\mathcal{I}_q) - P^{min}_{illumi}$$

$$s.t.\ (7), (8), (9), (10), (11)$$

$$P^{i,m}_{DC} + \sum_{j\in\mathcal{M}}\sum_{b\in\mathcal{W}}\sum_{n\in Rx_j} P^{i,m}_{AC} x^b_{ij,mn} \leq P^{i,m}_{max} \ (\forall i \in \mathcal{V}, \forall m \in Tx_i)$$

$$E^U_k \geq \sum_{i\in\mathcal{V}}\sum_{j\in\mathcal{M}}\sum_{b\in\mathcal{W}}\sum_{m\in Tx_i}\sum_{n\in Rx_j} (P^{i,m}_{DC} g^{DC}_{i,k,m} +$$

$$P^{i,m}_{AC,Avg} x^b_{ij,mn} g^{AC}_{i,k,m})\rho + E^{Am}_k \geq E^L_k \ (\forall k \in \mathcal{K})$$

where $P^{i,m}_{DC}$ and $x^b_{ij,mn}$ are the variables.

RMP and PP are solved in an iterative way, until PP returns a non-negative reduced cost. However, since the size of $\mathcal{Q}$ could be huge, it might take long time to reach the

optimal solution. Therefore, instead of finding the optimal solution, we propose an ϵ-bounded approximation approach to find a satisfactory ϵ-bounded solution.

4.4.3 ϵ-Bounded Approximation Approach

Let z^* denote the optimal result of MP and z^u denote the optimal result of RMP (upper bound on z^*), when $\kappa \geq \sum_{1 \leq q \leq |\mathcal{Q}|} \omega_q$ holds for the optimal solution of MP, the z^u can not be reduced more than κ times the most negative reduced cost c_r^* [79] :

$$z^u + \kappa c_r^* \leq z^* \leq z^u$$

Denote $z^l = z^u + \kappa c_r^*$ as the lower bound on z^* and the following lemma can be proved.

Lemma 3. *Define ϵ as $0 \leq \epsilon < 1$. The optimal solution of RMP $z^u \leq (1+\epsilon)z^*$, if $z^u/z^l \leq 1+\epsilon$.*

Proof. If $z^u/z^l \leq 1+\epsilon$, then $z^u \leq (1+\epsilon)z^l \leq (1+\epsilon)z^*$. Hence, z^u is the ϵ-bounded solution of MP. □

Based on the ϵ-bounded approximation approach, the iteration of column generation can be terminated when $c_r^* \geq 0$ or $z^u/z^l \leq 1+\epsilon$.

4.4.4 Reality Check

Although the column generation based ϵ-bounded approximation algorithm is capable of efficiently finding the ϵ-bounded solution of MP, the feasibility of the Protocol Model solution is doubtful. Under the Protocol Model, the impact of some non-zero interfering links are neglected, which may lead to overestimation of the achievable link capacity. Thus the power consumption solution (under the Protocol Model) of MP may be lower

than the real power consumption in practice. To investigate the practical objective value of MP, a validation process called "reality check" is introduced in [80]. Note that, in [80], the "reality check" process is neither integrated with the column generation algorithm nor applied to evaluate the real power consumption.

Since the Protocol Model solution of RMP includes all the ISs with non-zero ω_q, the link scheduling (i.e., which link is active and which link is idle) of each of those ISs can be known. Hence, the actual achievable capacity of each active link can be recomputed by equation (2). The "reality check" process consists of two steps: i) Recompute the actual link capacity by equation (2) for the Protocol Model solution of RMP; ii) Substitute the recomputed link capacity into RMP and re-optimize the RMP to obtain a feasible solution of power consumption. The column generation based ϵ-bounded approximation algorithm with reality check is summarized in Algorithm 2.

Algorithm 2 Column generation based ϵ-bounded approximation algorithm with reality check

Require: Initial independent sets $\tilde{\mathcal{Q}}$, traffic demands $\mathcal{R}_j$, interference set of each link $\mathcal{T}^b_{ij,mn}$, Protocol Model link capacity $\mathcal{C}^b_{ij,mn}$, optical signal strength $P^{i,m}_{AC}$, maximum power consumption $P^{i,m}_{max}$, approximation factor ϵ, gains of AC and DC optical power $g^{AC}_{i,k,m}$ and $g^{DC}_{i,k,m}$, wall plug efficiency factors $\eta^{i,m}_{AC}$ and $\eta^{i,m}_{DC}$, illuminance lower and upper bounds E^l_k and E^u_k, ambient lighting level E^{Am}_k, $c^*_r = -\infty$, $\kappa = 1$, $z^l = -\infty$ and $z^u = \infty$.

Ensure: Time fraction (out of one time unit) ω_q and solution of RMP z^u.

1: Compute $P_{AC,Avg}(\mathcal{I}_q)$ and $P_{DC}(\mathcal{I}_q)$ for $\tilde{\mathcal{Q}}$, and compute P^{min}_{illumi};
2: **while** $z^u/z^l > 1+\epsilon$ and $c^*_r < 0$ **do**
3: Solve RMP and obtain its optimal result z^u and dual optimal solution λ_j;
4: Solve PP with λ_j and obtain a IS $\mathcal{I}_q$ with c^*_r and the corresponding optimal $P^{i,q,m}_{DC}$;
5: Update c^*_r and $\tilde{\mathcal{Q}} = \tilde{\mathcal{Q}} \bigcup \mathcal{I}_q$, and compute the new $P_{AC,Avg}(\mathcal{I}_q)$ and $P_{DC}(\mathcal{I}_q)$;
6: $z_l = z^u + c^*_r$;
7: Update the link capacity in RMP by reality check;
8: Re-optimize RMP and obtain its optimal result z^u;

4.5 Practical Issues

4.5.1 Three Configurations of Light Source

Typically, a light source operates with fixed beamangle (i.e., formed by the central luminous flux and the central vertical line) and beamwidth (i.e., semi-angle at half power $\theta_{1/2}$). This configuration is capable of efficiently providing sufficient illumination. However, its weak competitiveness manifest on the communication functionality, due to the high inter-link interference and non-uniform distribution of optical signal strength, which will lead to severe degradation of channel gain when the transceivers are not strictly aligned. To mitigate the interference and enhance the channel gain, mechanically steering the beamangle and beamwidth is introduced in [81] and [82]. In this chapter, we further explore the impact of tuning the beamangle and beamwidth on the power consumption of multi-user VLC indoor networks. Although adjustable beamangle can be implemented by traditional *mechanical steering* method, the energy cost of tuning the orientation of light source is considerable [83], and even worse, the time it takes to change the direction is inevitable, which will bring a significant negative-impact on the network delay and capacity. To circumvent these problems, a new structure of light source is proposed. Multiple chips with different beamangles and beamwidths are installed on one light source and the diversity of orientation of light source can be implemented by activating any of those chips. This configuration is motivated by the "*electronic steering*" concept introduced in [83]. Since the new structure of light source needs to be specified before being evaluated by the optimization algorithm, we outline an implementable design of such light source based on the assumption of uniformly distributed UTs. In summary,

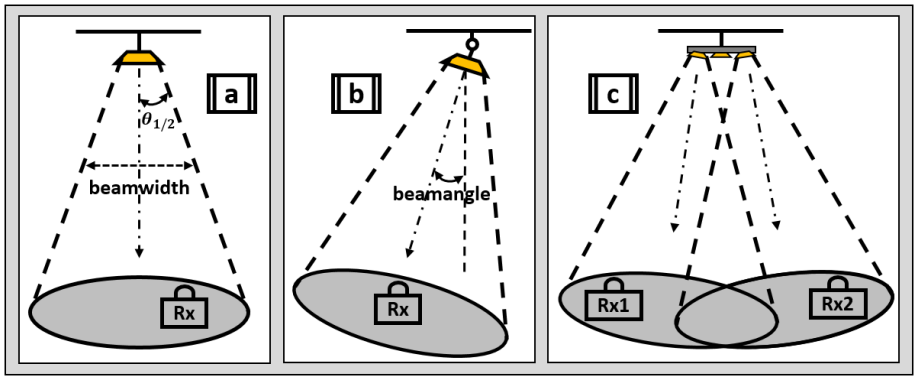

Figure 4.2 Three different configurations: a) fixed beamangle and beamwidth; b) mechanically adjustable beamangle and beamwidth; c) electronically selectable beamangle and beamwidth.

three configurations[2] (shown in Figure 4.2) of light source are investigated: i) fixed beamangle and beamwidth; ii) mechanically adjustable beamangle and beamwidth; iii) electronically selectable beamangle and beamwidth.

As shown in Figure 4.2, for Config. a, the beamwidth and beamangle are fixed regardless of the location of UT. The orientation of all VLC APs are vertical to the horizontal UTs plane. The semi-angle at half power $\theta_{1/2}$ (i.e., beamwidth) of AC and DC powered sources are the same. For Config. b, the beamwith and beamangle are tunable. For the purpose of concentrating the optical signal, the $\theta_{1/2}$ of AC powered source is set to be smaller than that of DC powered source. By adjusting the beamangle, the transmitter can directly point to the receiver. It can be seen that, for Config. b, the radiance angle of each link is always zero. For Config. c, multiple chips are installed on one VLC AP. The beamangle and beamwidth of each chip are fixed. Nevertheless, the VLC AP can selectively activate any of those chips and "electronically steering" the beamangle and beamwidth. Notice that, since the beamangle of each chip (for Config. c) is fixed, the

[2]In order to distinguish the difference among three configurations, it is assumed that, in the first and the second configurations, the beamangle of all the transmitters on one VLC AP are the same.

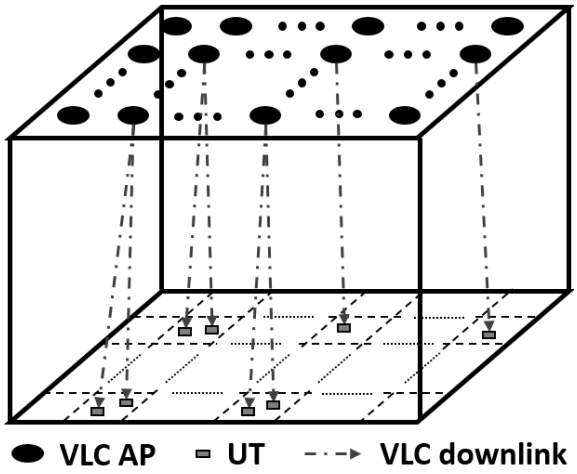

Figure 4.3 Grid structure of multi-user VLC indoor network.

transmitter might not be able to directly point to the receiver, such as for Config. b. Next, we specify the new structure of light source for Config. c.

4.5.2 New Structure of Light Source

As shown in Figure 4.3, the VLC APs are mounted on the ceiling in grid structure. To maximize the capacity of each link, each UT[3] chooses the nearest VLC AP to associate with, thus the served area of each VLC AP can be modeled as a square. In Figure 4.4, a new structure of light source is shown. It can be seen from Figure 4.4 (a) that, one VLC AP is equipped with $(n \times n) + 1$ chips, including $n \times n$ (n is a multiple of 2) peripheral chips and one central chip, which is mainly responsible for illuminating. In Figure 4.4 (c), a square area served by a VLC AP is equally divided into $n \times n$ small square regions. Each peripheral chip is assigned to serve one region. The star (i.e., center of coverage) in each region is the intersection of the central luminous flux of the corresponding peripheral

[3]To focus on the configuration of light source and make it easier to understand, it is assumed here and also in the simulation that, each UT is equipped with only one receiver. It means that each UT can connect to only one VLC AP at a time.

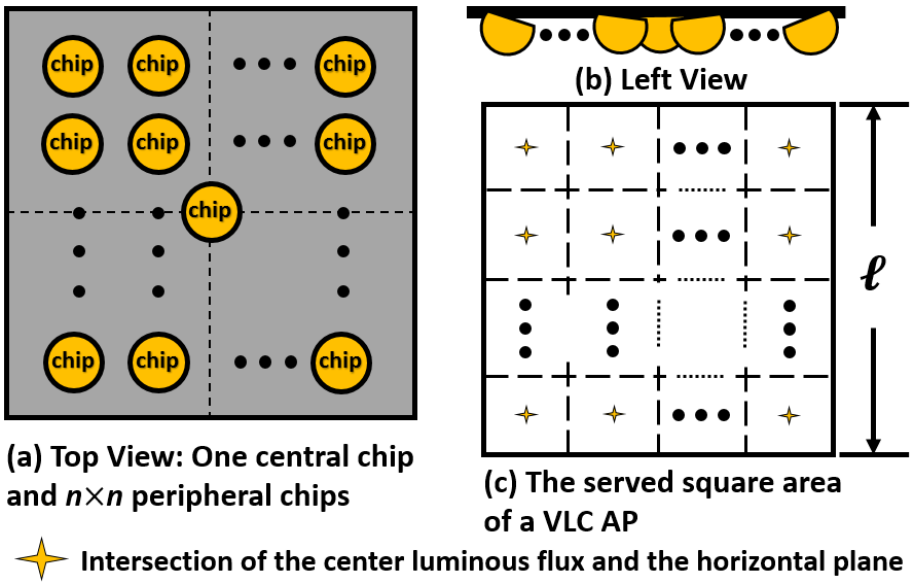

Figure 4.4 New structure of light source.

chip and the horizontal UT plane. Each star is located at the center of each square region. Denote the side length of a square area served by a VLC AP as l, the maximum distance d_{max} between a UT and its corresponding center of coverage satisfy $d_{max} \leq \frac{\sqrt{2}l}{2n}$.

4.5.3 Constructing Conflict Graph

In this section, we also introduce an effective approach to construct the conflict graph for multi-user VLC indoor networks. Traditionally, in Protocol Model, whether or not a transmission is being interfered by another transmission is determined by the distance between the receiver and the non-intended transmitter [74, 80, 84]. In VLC network, this standard is not always applicable, since the optical signal propagation may not be isotropic from the perspective of UTs plane. In [85], the orientation of each VLC AP is fixed and vertical to the horizontal UTs plane, such that the conflict graph, constructed by using the interference range [74] as in RF networks, is valid. However, if the orientation of VLC APs is tunable, then interference range is not a reliable measure to accurately model the

level of interference. As such, we propose a new criterion, according to which, if one of the pairwise signal-to-interference ratio (SIR) measurement of two links is lower than a threshold SIR_{th}, those two links can not be scheduled in the same IS.

Under Protocol Model, we define a maximum SIR threshold as SIR_{th}^{max} such that if $SIR_{th} \geq SIR_{th}^{max}$, then when any link is active, other links on the same channel can not be active. A minimum SIR threshold SIR_{th}^{min} is 1, since if $SIR_{th} < 1$, the interference signal will be stronger than the transmission signal. For a wireless network with high traffic load, there could exist an upper bound SIR_{th}^{U} for SIR threshold such that if $SIR_{th} > SIR_{th}^{U}$, the Protocol Model solution is infeasible (i.e., $\sum_{1 \leq q \leq |\mathcal{Q}|} \omega q > 1$). For a dense wireless network, there could exist a lower bound SIR_{th}^{L} such that if $SIR_{th} < SIR_{th}^{L}$, even though the Protocol Model solution is feasible (i.e., $\sum_{1 \leq q \leq |\mathcal{Q}|} \omega q \leq 1$), the reality check result is infeasible. Therefore, we need to select the SIR_{th} within the range $[SIR_{th}^{L}, SIR_{th}^{U}]$. In Section 4.6, we study the SIR_{th}^{U} and the SIR_{th}^{L} for a VLC indoor network with three different configurations of light source through simulations.

4.6 Numerical Results

In this section, we conduct extensive simulations to evaluate our proposed algorithm integrated with the practical issues. The simulations are conducted under Matlab R2013b and CPLEX 12.6.1 [86] on a computer with 2.0 GHz and 4 GB RAM. We study the cost of solving the MP under different values of ϵ. Our proposed algorithm is compared with two other recent schemes [82, 85] in terms of power consumption and running time. In [82], the VICO framework does not consider the illumination constraints in the algorithm. Let P_{total} represent the total power consumption of a given scheme, since the

illumination is always needed, the power consumption evaluated in the numerical analysis is $P_{total} - P_{illumi}^{min}$.

The room size is 6.0 m $\times$ 6.0 m $\times$ 3.0 m. The height of desk is 0.8 m and the UTs are randomly distributed on the desk according to uniform distribution. There are 36 (6$\times$6) VLC APs in grid structure installed on the ceiling and each VLC AP is equipped with one chip[4] (i.e., transmiter) filled with 625 (25$\times$25) white light LEDs. Note that, for the new structure of light source (Figure 4.5), each VLC AP is equipped with 5 such chips[5]. The distances between two neighboring VLC APs and two neighboring LEDs are 1 m and 1 cm, respectively. The maximum transmitted optical power of each LED is 20 mW. The value of P_{AC} of each VLC AP is set to 0.1 W. $P_{AC,Avg}$ is set to be half of P_{AC}. The channel bandwidth of each VLC link is 100 MHz and we assume all the VLC APs use the same channel in the simulation. The constant Gaussian noise is calculated from the parameters in [3] and set to be 4.7×10^{-14} A^2. The receiver parameters (i.e., FOV of receiver, detector area of a photodiode, gain of optical filter, refractive index of lens and O/E conversion efficiency) are the same with those in [3]. The required illuminance range is 300-500 lux. For Config. a, the semi-angle at half power $\theta_{1/2}$ of AC and DC powered sources are both set to 70°. For Config. b, $\theta_{1/2}$ of AC powered source is set to 30°, while that of DC powered source is set to 70°. For Config. c, as shown in Figure 4.5, $\theta_{1/2}$ of the central chip is set to 70°, and $\theta_{1/2}$ of the peripheral chips are all set to 30°. The wall plug efficiency factors η_{AC} and η_{DC} for all the VLC transmitters are set to 0.02 and 0.1, respectively.

[4]It means that each VLC AP can serve only one UT at a time.

[5]In order to fairly evaluate the three configurations, for Config. c, it is assumed that only one of the peripheral chips can be active for data transmission at a time, and the total optical power generated from one VLC AP can not exceed the P_{max} of a single chip.

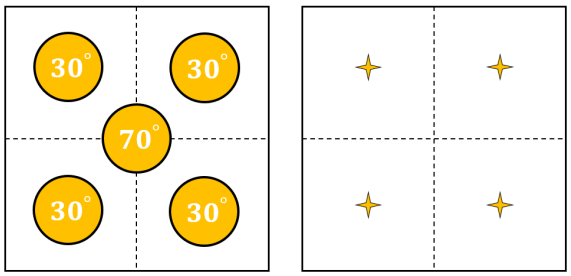

(a) The top view of the sample VLC AP (b) The served square area of the sample VLC AP

Figure 4.5 A sample new structure light source.

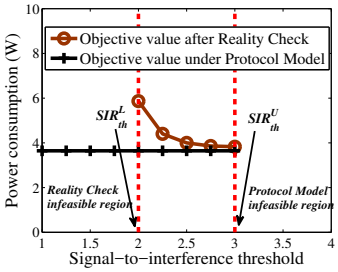

Figure 4.6 Protocol Model solutions and corresponding reality check results.

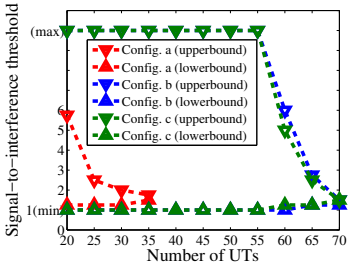

Figure 4.7 SIR_{th}^{L} and SIR_{th}^{U} for three configurations.

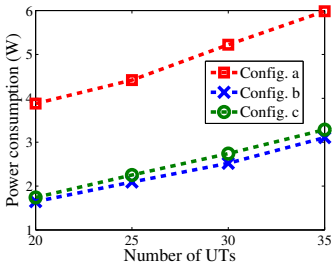

Figure 4.8 Real power consumption under different number of UTs for three configurations.

4.6.1 Cost of Solving MP

For a 30-UTs VLC indoor network, Table 4.1 shows the number of iterations and the total running time needed to achieve an ϵ-bounded solution. It can be seen that, it takes 14 iterations and 9.33 seconds to obtain 1%-bounded results, and 44 iterations and 17.84 seconds to get a near-optimal result (i.e., $\epsilon \approx 0$). For the following numerical results, we use $\epsilon = 0.01$.

Table 4.1 Iteration Number and Running Time for An ϵ-bounded Solution

ϵ	Number of Iterations	Running Time (s)
0.01	14	9.33
0.005	22	11.56
1×10^{-14}	44	17.84

4.6.2 Constructing Conflict Graph

For a 30-UTs VLC indoor network under Config. a, the traffic demand of each UT is 20 Mbps, we show the Protocol Model solutions and the corresponding reality check results in Figure 4.6. The upper bound for SIR threshold SIR_{th}^{U} is 3, and if $SIR_{th} > 3$, the Protocol Model solution will be infeasible. The lower bound for SIR threshold SIR_{th}^{L} is 2, and if $SIR_{th} < 2$, the reality check solution will be infeasible. When $2 \leq SIR_{th} \leq 3$, although the Protocol Model solution is almost the same, a lower SIR_{th} will lead to a higher reality check result, which is due to neglecting the non-zero interference in Protocol Model. Thus, choosing SIR_{th}^{U} as the SIR threshold will minimize the total power consumption while satisfying the traffic demands.

In Figure 4.7, we show the SIR_{th}^{U} and the SIR_{th}^{L} for a VLC indoor network under the three configurations. As the number of UTs increases, the SIR_{th}^{U} will decrease and the SIR_{th}^{L} will increase. And when the SIR_{th}^{U} and the SIR_{th}^{L} converge to one value, this indicates that the traffic load reaches up to the system capacity. From Figure 4.7, we can observe that, the system capacity of Config. b and Config. c is around double that of Config. a. And the feasible region of Config. b and Config. c is larger than that of Config. a, which shows the superiority of the new structure of light source (i.e., Config. c).

4.6.3 Power Consumption Evaluation

In the following, we evaluate the objective value (i.e., power consumption) for the three configurations, in terms of different number of UTs. From Figure 4.8 , it can be observed that, the real power consumption (after reality check) for Config. a is more than double that for Config. b and Config. c. More to the point, the real power consumption for

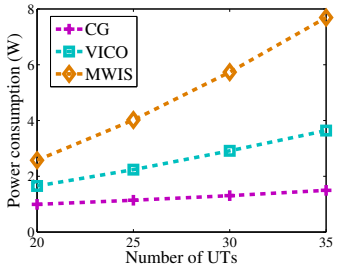

Figure 4.9 Real power consumption under different number of UTs for three algorithms.

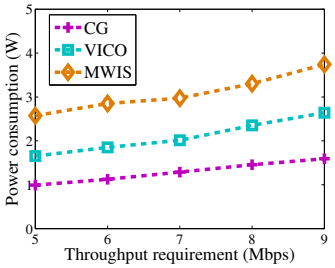

Figure 4.10 Real power consumption under different throughput requirement for three algorithms.

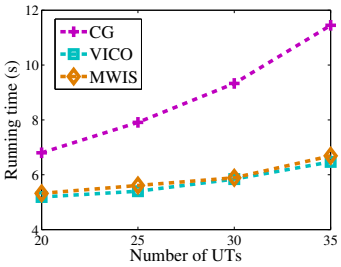

Figure 4.11 Algorithm running time under different number of UTs for three algorithms.

Config. c, which is much more practical than Config. b, is almost the same as that for Config. b. In summary, the new structure of light source (i.e., Config. c) is a practical design and capable to provide excellent power-saving performance.

We also compare the ϵ-bounded solution obtained by column generation (CG) with the results obtained by a random link scheduling introduced in VICO [82] and a link scheduling based on maximum weighted independent set (MWIS) introduced in [85]. The real power consumption under the three algorithms are simulated in terms of different number of UTs and different throughput requirement of each UT. As shown in Figure 4.9, the traffic demand of each UT is 5 Mbps, the real power consumption under VICO and MWIS becomes much higher than that under CG, as the number of UTs increases. For a 35-UTs network, the CG algorithm cuts the power consumption of VICO by 60%. Although the MWIS algorithm can achieve a better objective value under Protocol Model than random scheduling, after reality check its power consumption is much worse than that of VICO due to neglecting the non-zero interference from other links. The results shown in Figure 4.10 are consistent with the above analysis. For a 20-UTs VLC network, as the throughput requirement of each UT increases, there is almost no changes in the gaps between the real power consumption obtained by three algorithms.

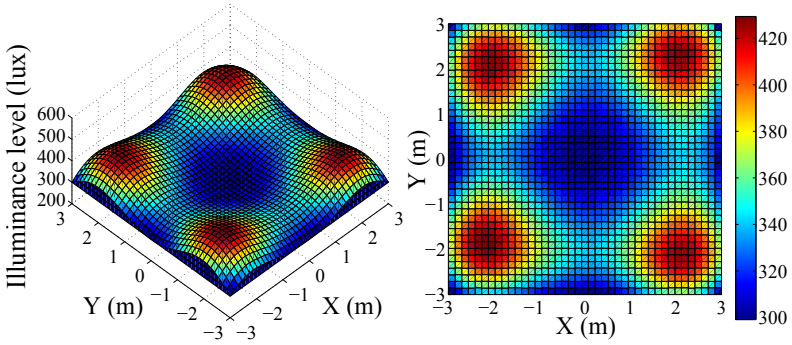

Figure 4.12 A sample distribution of illuminance created by our proposed algorithm with the entire horizontal space illumination constraints.

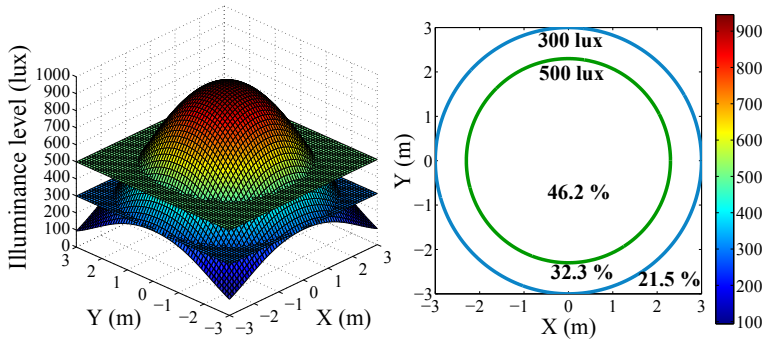

Figure 4.13 A sample distribution of illuminance under the VICO framework.

4.6.4 Illumination Evaluation

Regarding the illuminance satisfaction, in our proposed algorithm, since the illuminance level for the entire horizontal space is conditioned to be within the specified range (300-500 lux), the illuminance distribution always meets the requirements. In Figure 4.12, we show a sample distribution of illuminance under our proposed algorithm. We also show a sample illuminance distribution under VICO framework in Figure 4.13. Around 70% of the horizontal space do not meet the illumination requirements, because VICO framework does not take the illumination constraints into account when performing the optimization algorithm.

4.6.5 Cost of Three Algorithms

The running time costs by minimizing the power consumption under three algorithms are shown in Figure 4.11. We can observe that, the CG algorithm costs around 5.2 seconds more than that of the random link scheduling under VICO. Nevertheless, the optimization algorithm can be run with one-time cost in the centralized controller and no extra operations are needed until the network environment changes. This extra overhead is acceptable, given that our algorithm can achieve a 60% power-saving performance while satisfying the illumination requirements.

4.7 Related Work

Many efforts have been paid on the VLC indoor network, however, most of them do not provide comprehensive consideration on the illumination and communication, or only focus on limited aspects. Even though one of them [82] proposes a framework for configuring the VLC indoor networks with adjustable LEDs beamangle and beamwidth, the link scheduling algorithm has no power efficiency guarantees and the framework relies on a simple impractical assumption to measure the illumination using the average SNR distribution.

The LED angle tuning issue is also studied in [81], which only presents the heuristic simulation results of the average SNR distribution without considering illumination. For the cooperation among VLC cells, the work in [64] presents an elaborate study on the bandwidth efficiency of four different VLC cell formations. However, in the cooperative load balancing approach, the users traffic demand is not considered. The merging VLC cell approach is also studied in [85], which has not taken the illumination into account.

In [87], an optimal Lambertian order algorithm is proposed. To maximize the VLC cell boundary signal strength, an optimal Lambertian order can be found by calculating the first order derivative of the VLC path loss model. Whereas the illumination and multiple users scenario are not considered in this work. The work in [88] introduces the concept of DC and AC optical power without considering overall power consumption optimization and the distribution of illumination. In [70], the authors investigate the energy-efficiency for only optical power with brightness control and data transmission in VLC networks. Three power levels of the sub-carrier pulse position modulation scheme are utilized as the variables to perform the power consumption optimization. Nonetheless, in their optimization constraints, the brightness control is only applied to the location of user, which is not practicable. A multi-transceiver optical wireless spherical structure is proposed in [83]. The spherical optical antenna is tessellated with multiple LEDs, to enable the beamangle diversity. However, this design does not carefully consider the illumination functionality of LEDs. The transverse line-of-sight of the spherical optical antenna may produce glaring in some specific scenarios. Several brightness control methods have been introduced in [89]. The PWM and DC bias are two predominant approaches for dimming control. A room division multiplexing-based VLC network is proposed in [8], while in our work, the concept of space division multiplex is manifested by adjusting the Lambertian order.

4.8 Conclusion

In this chapter, we investigate the problem of minimizing the total power consumption of a general multi-user VLC indoor network while satisfying the traffic demands and providing

acceptable level of illumination. A column generation based -bounded algorithm with reality check is proposed. Regarding the light source, three configurations are considered and one of them (i.e., a new structure of light source) is proposed. For constructing the conflict graph, an effective range of SIR threshold is evaluated by extensive simulation results. The power consumption of the three configurations are evaluated by simulations and the results reveal that the new structure light source is practical and provides power-efficient solutions. Compared to two other VLC link scheduling algorithms, our proposed algorithm can achieve a better performance of power consumption, especially in crowded scenarios, while satisfying the illumination requirements on the entire horizontal plane.

CHAPTER 5

A NOVEL PIXELATED VLC BACKSCATTER

5.1 Introduction

In this chapter [1], we propose and implement a novel VLC backscatter, called pixelated VLC backscatter, which uses multiple smaller reflectors and LCD shutters to form numbers of pixels. Each pixel can switch on or off independently in order to produce multi-level signals. As shown in Figure 5.1, with the same size of single pixel, pixelated backscatter utilizes more pixels by reducing the size of each pixel. Our proposed *pixelated* concept follows a similar concept as in [91] in terms of the contribution of multiple signals to form the effective communication signal. However, the motivation behind the LED based optical domain DAC in [91] is to be able to cover a wider dynamic range for a high peak-to-average-ratio (PAPR) orthogonal frequency division multiplexing (OFDM) signal, thus trading-off the elimination of the electrical digital-to-analog conversion (DAC) with higher complexity at the transmitter circuitry required to derive multiple LEDs. The main motivation of our independently designed work is allowing for the first time advanced modulation schemes in IoT using optical backscattering; multi-level (PAM) and multi-carrier (OFDM). Based on experiments, it is observed that the energy consumption of the pixelated design causes negligible overhead. Based on our testbed, the throughput achieved by the pixelated VLC backscatter is 600 bps at 2 meters, which is highly restricted by the response time of the off-the-shelf LCD shutters (5 ms). By reducing the size of LCD shutter, the capacitance of the LCD shutter is expected to

[1] The work of this chapter has been published in [90]

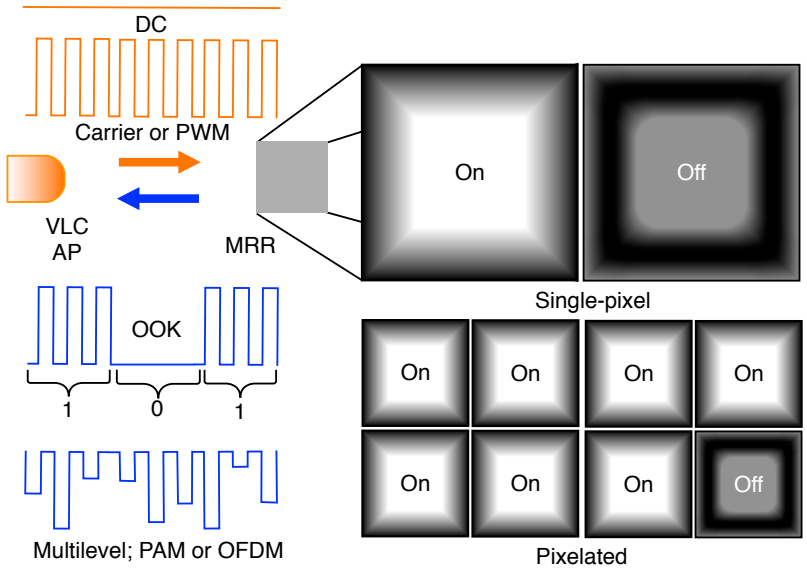

Figure 5.1 The proposed pixelated based system.

decrease. According to [92], reducing the size of LCD shutters can potentially enhance the throughput by increasing the modulation frequency. Here, we do not customize the size of LCD shutters since we use the off-the-shelf samples.

5.2 Theoretical Analysis

In this section, we theoretically evaluate the benefit of adding pixels and the relationship between the maximum communication distance and the target BER. We also evaluate the amount of power that can be harvested for indoor environment.

In order to control the pixelated VLC backscatter while achieving a target backscattered signal quality, our main goal is to investigate the trade-off between the required number and size of pixels, signal-to-noise ratio (SNR) and resolution. Assume that the array, consists of identical pixels, i.e., when switched on, each pixel backscatters the same amount of optical power proportional to incident optical flux on it, then the backscattered light is proportional to the number of pixels that are switched on (Figure 5.2 (a)). In this

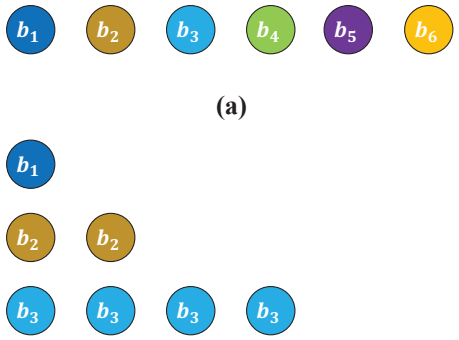

Figure 5.2 Structure of pixels: (a) pixels with the same size; (b) binary-weighted clustering pixels.

case, 2^m optical levels can be achieved by switching 2^m pixels. To reduce the number of pixels with a given resolution, we can try to use a binary-weighted structure (Figure 5.2 (b))(Similar to the concept of Figure 4 in [91]). In this case, the m^{th} cluster contains 2^{m-1} same-size pixels. In the following context, we refer to m instead of 2^{m-1} when we discuss the number of pixels, since the cluster of same-size pixels can be viewed as different-size pixels.

Here, PAM is considered as the modulation scheme. The 2^m optical levels enhance the bit rate by m times, when compared to the OOK, of which the bit rate is 1 bit/symbol. Given the symbol rate and assume the target BER is always satisfied, the throughput of m pixles based pixelated VLC backscatter is m times that of the single pixel. Since the IoT device is conceptually very small, assuming a certain area of VLC backscatter, we investigate the trade-off between the number of pixels and communication distance for a target BER.

Consider the M-PAM, the required number of pixels is $log_2 M$. The relationship between BER and SNR is [93]

$$\text{BER} = \frac{2(M-1)}{M log_2 M} Q(\frac{1}{M-1}\sqrt{SNR}) \tag{5.1}$$

where SNR denotes the square of the ratio of peak-to-peak amplitude and noise. Here we consider the noise as the worst case, which is the case that all the pixels are switched on. Since SNR is inversely proportional to the communication distance, it can be easily found that, given the BER, the number of pixels $log_2 M$ is inversely proportional to the maximum communication distance d. Based on (1), we calculate the required SNR for different modulation schemes when the target BER is 10^{-3} and show the results in Table 5.4.

5.2.1 Power Harvesting

To evaluate the amount of power that can be harvested for indoor environment, we perform the following calculation: $P = E_{lux} \times I \times A \times E_{solar}$, where E_{lux} denotes the conversion ratio from lux to watt/cm^2, I denotes the illumination in unit lux, A represents the solar cell area, and E_{solar} represents the solar cell efficiency factor, we can find the electrical power P that can be generated by solar cell under indoor environment. We have $E_{lux} = 1.46 \times 10^{-7}\ watt/cm^2/lux$ [94], $I = 300\ lux$, and $A = 25\ cm^2$. The solar cell efficiency 20% is generally available for commercialized solar cell products [95]. Substituting these values into the solar power calculation, the output $P = 219\ \mu W$.

5.3 Experimental Results

5.3.1 Testbed Setup

The testbed consists of an 8.5 Watts white LED bulb, a microcontroller MSP430G2553 from Texas Instrument, three LCD shutters from Liquid Crystal Technologies, three super base ball stages, three cage mounted irises with diameter 20.0 mm and Photodetector PDA 36A from Thorlabs, three small mirrors, oscilloscope Tektronix MDO-4034, and a DC power supply.

The response time of the LCD shutters is around 5 ms, thus the maximum modulation frequency is set at 200 Hz. In [26], the response time of their LCD shutter is 2 ms, thus the effective bandwidth of their LCD shutter is larger than that of ours. The super base ball stages are used to control the azimuth and elevation angle of the pixels in order to perform the alignment. Since this testbed works as a proof-of-concept to investigate the performance of pixlated VLC backscatter, manually controlled positioners are used for orientation. The cage mounted irises are installed upon the LCD shutters to manipulate the area of each pixel. For instance, when one pixel is activated, the diameter is set at 20.0 mm; when two pixels are activated, the diameter of the 1st pixel is set at 16.33 mm, and the diameter of the 2nd pixel is set at 11.54 mm, to keep the total reflector area the same as that of one pixel. Note that by customizing the size of each pixel instead of controlling the reflector area through iris, the effective bandwidth of each pixel could be enhanced (i.e., above 200 Hz). Here, we use the off-the-shelf samples instead of customizing the size of the LCD shutters. The transmitted signals are pre-compiled in MSP430G2553 and this microcontroller is powered by a DC power supply with 3 V. The optical signals modulated by LCD shutters are captured by the photodetector and

Table 5.1 MSP430 Using DCO Operates at 3 V

Frequency	Current
10 Hz	337 μA
100 Hz	341 μA
500 Hz	354 μA

Table 5.2 MSP430 Using VLO Operates at 3 V

Frequency	Current
10 Hz	68 μA
100 Hz	69 μA
500 Hz	70 μA

the waveform is displayed on the oscilloscope for further analysis. The VLC backscatter prototype, including the microcontroller MSP430 and three pixels, is shown in Figure 5.3. For each pixel, a LCD shutter is placed upon a reflector (i.e., mirrors), and a circular iris is fixed upon the LCD shutter to control the effective backscatter area.

5.3.2 Power Consumption

First, we measure the power consumption of microcontroller and LCD shutter. The microcontroller consumes power in the order of magnitude 100 μW while the LCD shutter consumes less than 0.2 μW at 200 Hz (i.e., maximum modulation frequency). Therefore, the power consumption of the microcontroller is dominant in the VLC backscatter system.

The default clock module of MSP430G2553 is an internal digitally controlled oscillator (DCO) operating at 1 MHz. When the DC power supply provides 3 V, the current is around 340 μA at 100 Hz (Table 5.1). The required power $\sim$1 mW is usually too high to be harvested from indoor illumination ($\sim$300 lux) by a small solar cell (e.g., 50 mm $\times$ 50 mm). Since the maximum modulation frequency of the LCD shutter is only 200 Hz, the internal very-low-power low-frequency oscillator (VLO) is selected instead, of which the typical frequency is 12 kHz. With 3 V DC supply, the power consumption of the

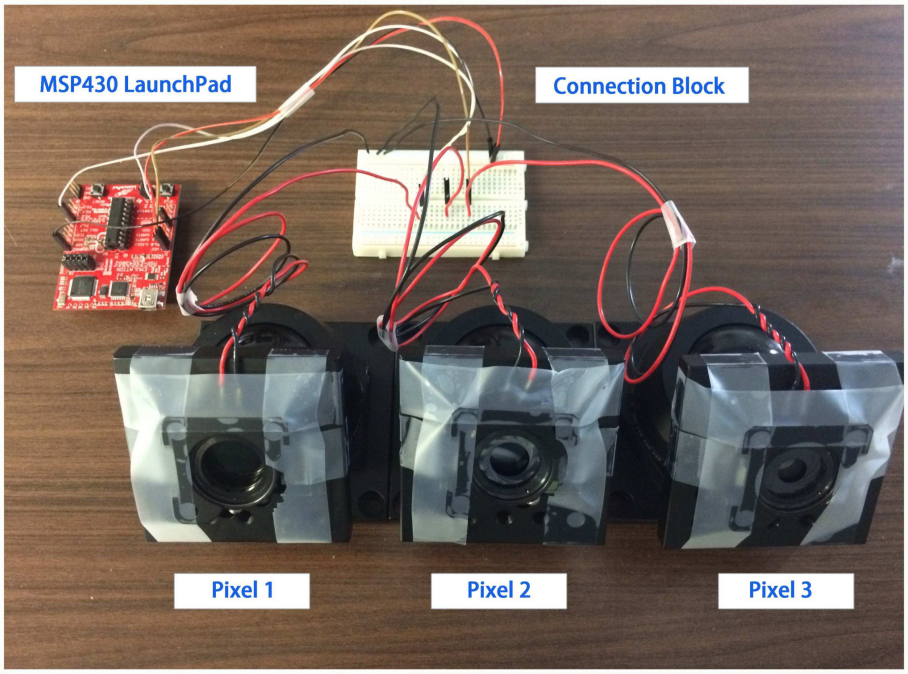

Figure 5.3 Testbed of pixelated VLC backscatter.

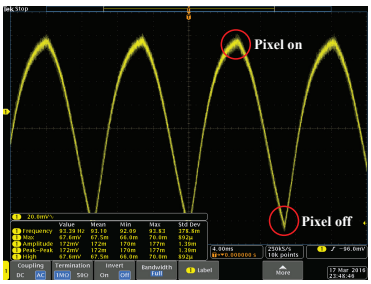

Figure 5.4 Single pixel transmits at the distance of 2 meters.

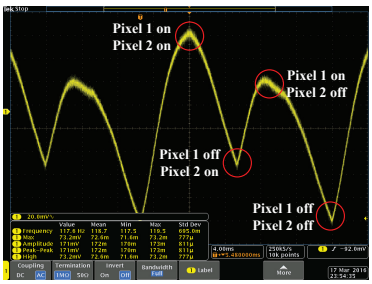

Figure 5.5 Two pixels transmit at the distance of 2 meters.

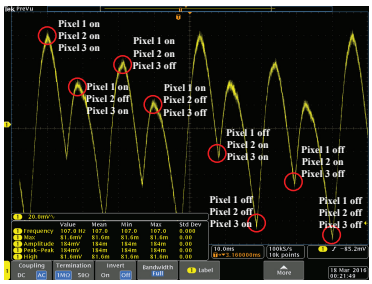

Figure 5.6 Three pixels transmit at the distance of 2 meters.

MSP430G2553 is reduced to around 200 μW (Table 5.2) when VLO is chosen. Compared to theoretical results in Section 5.2.1, the amount of power consumed by microcontroller (i.e., around 200 μW) can be harvested from indoor lighting. Note that, in Table 5.1 and Table 5.2, the impact of changing the frequency on power consumption is negligible.

5.3.3 Throughput vs. Distance

We now start evaluating the trade-off between achievable throughput and the maximum communication distance, as discussed in the Section 5.2. The number of pixels are varied from 1 to 3, corresponding to OOK, 4-PAM, and 8-PAM, respectively. The measurement distance is ranging from 2 meters to 5 meters. And the modulation frequency is set at 200 Hz, which means that the symbol rate is 200 symbols per second. The results for different number of pixels transmitting at 2 meters are shown in Figure 5.4 to Figure 5.6. Different signal levels are marked with the "ON" and "OFF" status of each pixel. Using unmodulated light beam on one end of the link to interrogate the pixelated VLC backscatter, the intensity of the backscattered signal depends on the number of pixels that are turned on or off. The backscattered intensities constructively add up, i.e., the backscattered signals are combined in the optical domain and not in the electrical domain. As it is observed from Figure 5.6, the Euclidean distance of the constellation between different signal levels is still much larger than the noise when 8-PAM is applied. In Figure 5.4, each signal level represents one bit and thus the achievable throughput is 200 bps. In Figure 5.6, each signal level represents three bits and thus the throughput is increased to 600 bps. Therefore, with a relatively short communication distance, the M pixels based pixelated VLC backscatter is able to provide M times of the throughput of

Table 5.3 Distance vs. SNR

2 m	3 m	4 m	5 m
26.55 dB	21.15 dB	18.80 dB	14.98 dB

Table 5.4 Modulation Scheme vs. Required SNR

OOK	4-PAM	8-PAM
9.80 dB	19.10 dB	26.23 dB
200 bps	400 bps	600 bps

the single pixel VLC backscatter with negligible energy overhead and the same reflector area.

To evaluate the trade-off between achievable throughput and the maximum communication distance, we measure the SNR at different distances and show the results in Table 5.3. Note that the SNR values measured at different distances are the same for OOK, 4-PAM, and 8-PAM. Compared to the results shown in Table 5.4, we observe that the OOK modulation scheme can achieve the target BER above 5 meters, while the 8-PAM can only achieve the target BER at around 2 meters. Therefore, we can conclude that, based on our testbed, 600 bps can be achieved at 2 m, 400 bps can be achieved at 3 m, and 200 bps can be achieved at above 5 m. The higher order PAM is beneficial at shorter distance by doubling or even tripling the throughput, but has to sacrifice the maximum communication distance. This fact motivates performing the rate adaptation. Modulation scheme with small Euclidean distance of the constellation is used at short communication distance to enhance the achievable throughput, while modulation scheme with larger Euclidean distance of the constellation is used at longer distance to guarantee the robust connectivity.

5.4 Conclusion

In this chapter, a novel pixelated VLC backscatter system is implemented. With ultra-low power overhead, n pixels can enhance the throughput by n times using the same reflector area when compared to single pixel VLC backscater. Based on our experimental results and using 8-PAM, 600 bps is achieved at 2 meters and this data rate can be still greatly enhanced if customizing the size of each pixel is available. At short distance, high order PAM is preferred to provide high throughput while at longer distance, lower order PAM is needed to maintain the channel quality.

CHAPTER 6

RETROREFLECTOR-BASED VISIBLE LIGHT POSITIONING

6.1 Introduction

In this chapter, we propose and prototype a retroreflector-based visible light localization system that we name RETRO. The retroreflector is a light-weight small device, which is capable of reflecting light back to its source with minimal scattering. Therefore, by mounting small-size light sensors, such as photodiodes (PDs), on infrastructural lamps, we can establish a backward channel from the retroreflector to VLC APs (i.e., lamps). In order to send unique identity information to APs, we add a liquid crystal display (LCD) shutter, which consumes only tens of μW with its driver circuit [26, 90], on the retroreflector to modulate and distinguish the reflected light for different IoT devices. The light-weight retroreflector along with an LCD shutter and its control unit can be installed on a passive IoT device to execute VLC-based real-time localization. The retroreflector can be realized by corner-cube, retroreflective sheeting [96] or even retroreflective spray paint [97]. In this chapter, we mainly study the corner-cube retroreflector. RETRO enjoys not only all the advantages (e.g., especially high location accuracy) provided by conventional VLC-based localization approaches, but also four unique and superior features: 1) RETRO can be implemented on *any single unmodified* light source; 2) immediate feedback from the retroreflector minimizes the latency of a centralized control of IoT devices; 3) RETRO is capable of locating passive IoT devices with ultra-low power and no computational capability at the devices; 4) RETRO establishes a visible light uplink channel, which makes joint localization and communication without an additional uplink RF channel

possible. In this chapter, we utilize the received signal strength indicator (RSSI) and trilateration based localization algorithm (Section 6.4) to locate the retroreflector. The RSSI resulted from the retroreflected light is theoretically analyzed (Section 6.3) and experimentally validated (Section 6.5). Based on experimental evaluation (Section 6.6), our proposed RETRO system can achieve centimeter-level localization accuracy (i.e., location error within 4.5 cm with the height of 1.5 meters) and less than 1° orientation error.

In summary, we make three key contributions:

- To the best of our knowledge, RETRO is the first system that enables real-time tracking using the VLC-based localization approach. Relying on *any single unmodified* light source, RETRO is capable of locating passive IoT devices without requiring computation or specialized hardware on the IoT device with minimum latency.
- We theoretically derive a closed-form expression for estimating retroreflected optical power from retroreflectors under Lambertian light source and experimentally validate the theory. Experimental results match theoretical results very well w.r.t different locations and orientations of the retroreflector.
- Based on the characterization of received optical power from the retroreflector, we develop an RSSI and trilateration based localization algorithm. We perform extensive experiments to evaluate the location and orientation accuracy of our proposed RETRO system and observe centimeter-level location accuracy (i.e., location error within 4.5 cm with the height of 1.5 meters) and up to 1° orientation error.

6.2 Overview of Proposed Localization Approach

In this chapter, RSSI and trilateration based localization approach [29] is used to estimate the position and orientation of an IoT device equipped with a retroreflector in the global frame of reference. Multiple PDs (i.e., landmarks) are mounted on one light source or multiple light sources to sense the reflected optical signal strength from a retroreflector.

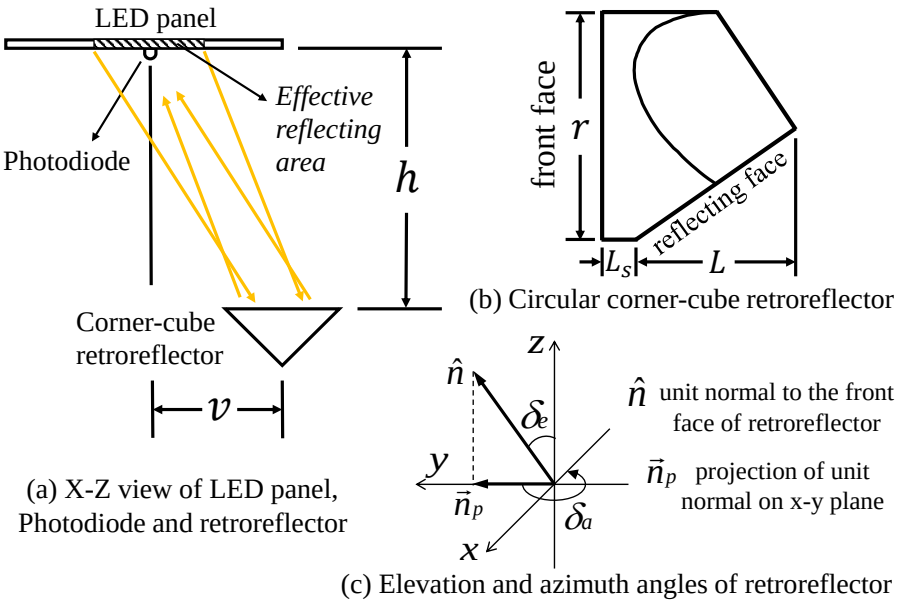

Figure 6.1 Illustration of system parameters.

An LCD shutter (Section 6.6.1) covering the front face of retroreflector produces unique signal frequency for each retroreflector to distinguish the reflected light from multiple IoT devices and from environmental reflections. As the retroreflector changes its location and orientation, the received signal strength of each PD varies correspondingly. In order to investigate the relationship between the location and orientation of the retroreflector and the received signal strength of each PD, we need to not only use the free space optical propagation model, but also characterize the area of light source, from which the light rays are retroreflected back to the corresponding PD. We call this area the *effective reflecting area*. Combining effective reflecting area, which is determined by the location and orientation of retroreflector, and the optical path loss model, we can derive closed-form expression for the received optical power of each PD. In Section 6.3, we theoretically study the effective reflecting area w.r.t different locations and orientations of the retroreflector.

6.3 Analysis for Received Optical Power

6.3.1 System Parameters

To derive the closed-form expression of retroreflected optical power, we define the following system parameters: 1. semi-angle at half power of light source $\psi_{1/2}$. An evenly distributed light source can be viewed as infinite small lighting spots, where all the spots have the same $\psi_{1/2}$. 2. refractive index of coating material of retroreflector n. 3. length of retroreflector L. 4. recessed length of retroreflector L_s. 5. diameter of retroreflector's front face r. 6. effective sensing area of PD A_s. 7. transmitted optical power multiplied by reflector loss (reflector loss includes the transmission loss of the coating material and the reflection loss of each reflection surface) P_t. 8. Lambertian index ml. 9. vertical distance between light source plane and the front face of retroreflector h. 10. horizontal distance between the PD and the retroreflector v. 11. elevation angle of the front face of the retroreflector δ_e. 12. azimuth angle of the front face of the retroreflector δ_a. The parameters are illustrated in Figure 6.1.

To make the derivation clearer, we divide it into two cases: 1) first we consider a special case where the elevation and azimuth angles are both zero, and we analyze the boundary of the effective reflecting area based on the symmetry property of the incident and retroreflected rays; then 2) we study the other case where the elevation and azimuth angles are equal to arbitrary values, and since the derivation in case 1 cannot be simply applied to case 2, we create a virtual light source plane and utilize oblique projection to analyze the boundary of effective reflecting area. Note that the light source we consider here is a flat LED panel with evenly distributed light across the face of the

panel. The derivation can be extended to the case where unevenly distributed light sources are considered.

6.3.2 Zero-value Elevation and Azimuth Angles Case

The distance between the PD and the retroreflector is

$$d = \sqrt{h^2 + v^2}. \tag{6.1}$$

Consider the scenarios when the distance between the light source and the retroreflector is much larger than the size of retrorefelctor, the radiance angles of all rays that are going to be reflected back to the PD can be approximated to be the same. Also, since the rays are reflected back along a vector that is parallel to but opposite in direction from the rays' source, the incidence angle to the PD is the same as the radiance angle. The value of radiance and incidence angles is

$$\theta = tan^{-1}\frac{v}{h}. \tag{6.2}$$

According to Snell's law, the refracted angle is

$$\phi = sin^{-1}\frac{sin\theta}{n}. \tag{6.3}$$

As shown in Figure 6.2, ray A incident on the center of the front face is retroreflected as ray A'. The points of intersection of A and A' with the front face are separated by D. Note that if $\theta = 0$, then $D = 0$. The solid line (circle O), which is the shape of the retroreflector face, is called the input aperture, and the dotted line (circle O'), which is giving the outline of the retroreflected beam, is the output aperture. We have $\overline{OO'} = D$. The intersection of the input and output apertures is the active reflecting area [98]. Assume

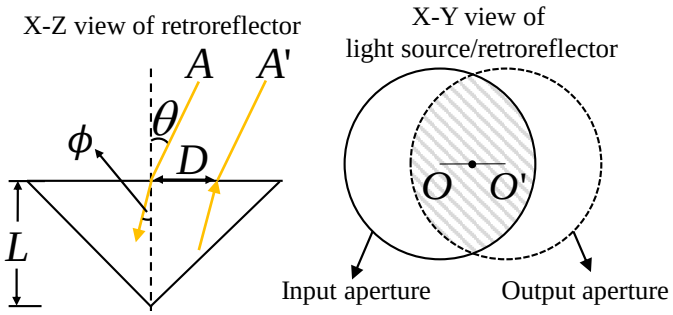

Figure 6.2 Displacement of input and output apertures caused by the oblique angle of incidence to the retroreflector.

a set of parallel rays incident on the front face of the retroreflector with angle θ, due to the symmetry of the incident and reflected rays requiring the last reflection to occur at a point inside the corner cube ([98] Page 9), only those within the active reflecting area are retroreflected. Note that in [98], the active reflecting area is given on the plane of the front face of the retroreflector to analyze the proportion of incident laser beam (i.e., a set of parallel light rays) that can be retroreflected. The theoretical analysis in [98] cannot be directly applied to Lambertian light source, from which the emitted light rays are not parallel. Therefore, In this chapter, we utilize the concept of active reflecting area, as illustrated in Figure 6.2, on the *plane of light source*. Assume a set of parallel rays incident on the front face of retroreflector with angle θ are emitted from the area within circle O on the light source plane, then only the rays from the intersection of circle O and O' are retroreflected. According to [98] (Page 10), the displacement of input and output apertures caused by the incidence angle θ is

$$D = 2Ltan\phi. \tag{6.4}$$

As shown in Figure 6.3, the recession wall shadows the front face of the retroreflector at an oblique incidence angle. The recession leads to additional displacement of

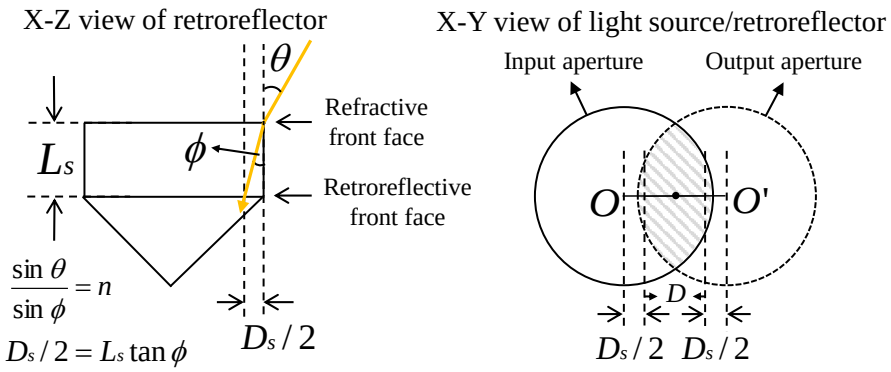

Figure 6.3 Displacement of input and output apertures caused by the recession.

input and output apertures D_s ([98] Page 14). From the top view of the light source, the distance between circle O and circle O' is further increased by D_s. Therefore, the active reflecting area on the plane of the light source is further reduced due to recession. The displacement of input and output apertures caused by recession is ([98] Page 14)

$$D_s = 2L_s tan\phi. \tag{6.5}$$

Given the displacements D and D_s, now we study which light rays are reflected to the PD. As shown in Figure 6.4, V is the midpoint of $\overline{OO'}$, where $\overline{OO'} = D + D_s$. Recall that the shaded area contains a set of parallel rays, of which the incidence angles to the front face of the retroreflector are all θ, and this set of parallel rays can be retroreflected back to the shaded area. Suppose a ray from point P' is one of the parallel rays, the retroreflected ray intersects with the shaded area at point P, which is an equal distance on the other side of vertex V ([98] Page 9). Therefore, if P is where the PD is located at, and considering the parallel rays (radiance angles are all θ) from circle O, the ray from point P' is the one that can be retroreflected to the PD.

On the light source plane, there are uncountable small circles with the same size as that of circle O. Each small circle contains a set of parallel rays, whose radiance

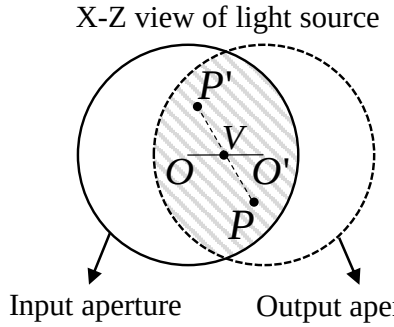

Figure 6.4 Symmetry of incident ray and retroreflected ray.

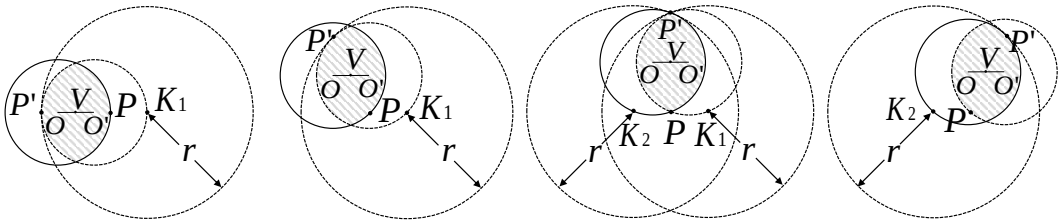

(a) P' is on circle K_1 (b) P' is on circle K_1 (c) P' is on circle K_1 and K_2 (d) P' is on circle K_2

Figure 6.5 Four cases when using symmetry of incident ray and retroreflected ray to analyze the boundary of effective reflecting area.

angle depends on the location of the corresponding small circle. If the PD is located in the shaded area of a small circle, in the corresponding set of parallel radiant rays, there exists a ray that can be reflected back to the PD. Therefore, there is an uncountable set of small circles, in each of them there exists a ray that can be reflected back to the PD. The intersection of the set of rays that can be reflected back to the PD with the *plane of light source* is the *effective reflecting area*.

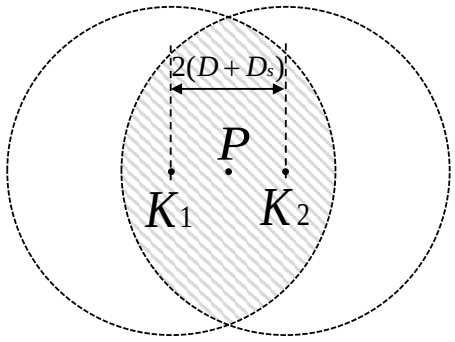

Figure 6.6 Effective reflecting area.

Theorem 4. *If the incidence angles of the light rays that can be retroreflected to the PD are approximated to be the same as the radiance angle θ, given two displacements D and D_s, and the diameter of retroreflector r, the size of effective reflecting area is the intersection of two circles, of which the radii are r and the distance between them is $2(D + D_s)$.*

Proof. In order to evaluate the size of the effective reflecting area, we need to figure out its boundary. Consider a special case in Figure 6.4, where P is on circle O, P' will be located on circle O' due to symmetry. It can be proved that for each point P'_m on $\overline{PP'}$ there exists a circle O and a circle O', where the intersection of two circles includes both P'_m and P, and the symmetry in Figure 6.4 holds. Therefore, for every point on $\overline{PP'}$ there exists a ray that can be retroreflected to P. P' is the furthest point (from which there exists a ray that can be retroreflected to P) away from P along the direction of $\overrightarrow{PP'}$. Since the incidence angles of the light rays that can be retroreflected to the PD are approximated to be the same, the separation distances and directions of circle O' for all the possible locations of circle O are the same. Therefore, if we rotate the intersection of circle O and circle O' (i.e., the shaded area in Figure 6.4) around P and keep P on the boundary of the intersection, considering P as the location of PD, the trajectory of P' will be the boundary of the effective reflecting area.

In Figure 6.5, we use two big circles (K_1 and K_2), of which the radii are r (i.e., diameter of circle O), to analyze the trajectory of P'. The distance $\overline{PK_1}$ and $\overline{PK_2}$ are both equal to $\overline{OO'}$, and both $\overline{PK_1}$ and $\overline{PK_2}$ are parallel to $\overline{OO'}$. In Figure 6.5 (a), $\angle P'K_1P = 0°$, since $\overline{PP'} = r - \overline{OO'}$ and $\overline{PK_1} = \overline{OO'}$, $\overline{P'K_1} = r$ which indicates that P' is on circle K_1. In Figures 6.5 (b), (c) and (d), it can be proved by the similarity between $\triangle P'VO'$ and $\triangle P'PK_1$ (or $\triangle P'VO$ and $\triangle P'PK_2$) that $\overline{P'K_1} = r$ (or $\overline{P'K_2} = r$), which indicates

that P' is either on circle K_1 or on circle K_2 when we rotate the intersection of circle O and O' (i.e., the shaded area in Figure 6.5) around P and keep P on the intersection boundary. Therefore, the trajectory of P' is the boundary of the intersection of circle K_1 and K_2. The effective reflecting area is the shaded area in Figure 6.6. □

Given D and D_s, the ratio of effective reflecting area to the maximum effective reflecting area (i.e., when $D + D_s = 0$) is

$$\alpha = \frac{2r^2(cos^{-1}\frac{D+D_s}{r} - \frac{D+D_s}{r}sin(cos^{-1}\frac{D+D_s}{r}))}{\pi r^2}. \tag{6.6}$$

Since the radiance angle of the effective reflecting area is equal to the incidence angle to the PD and the propagation distance is $2d$, according to the free space optical path loss model in [3], the received optical power is

$$P_r = P_t\frac{(ml+1)A_s}{8\pi d^2}cos^{ml+1}\theta\alpha. \tag{6.7}$$

6.3.3 Arbitrary-value Elevation and Azimuth Angles Case

If the front face of the retroreflector is not parallel to the light source plane, we cannot directly apply the analysis in case 1 (i.e., when $\delta_e = 0$ and $\delta_a = 0$) by simply varying the incidence angle to the front face of retroreflector. This is because the shape of the front face of retroreflector is different from its oblique projection along the direction of retroreflected light rays on the light source plane.

As shown in Figure 6.7, the retroreflector plane is parallel to the light source plane. Point P is where the PD is located at. Point P' is the projection of P on the retroreflector plane. Point O is the center of the front face of retroreflector. We use $\overrightarrow{P'O}$ as the direction of y axis and form the 3D coordinate systems for both the retroreflector and

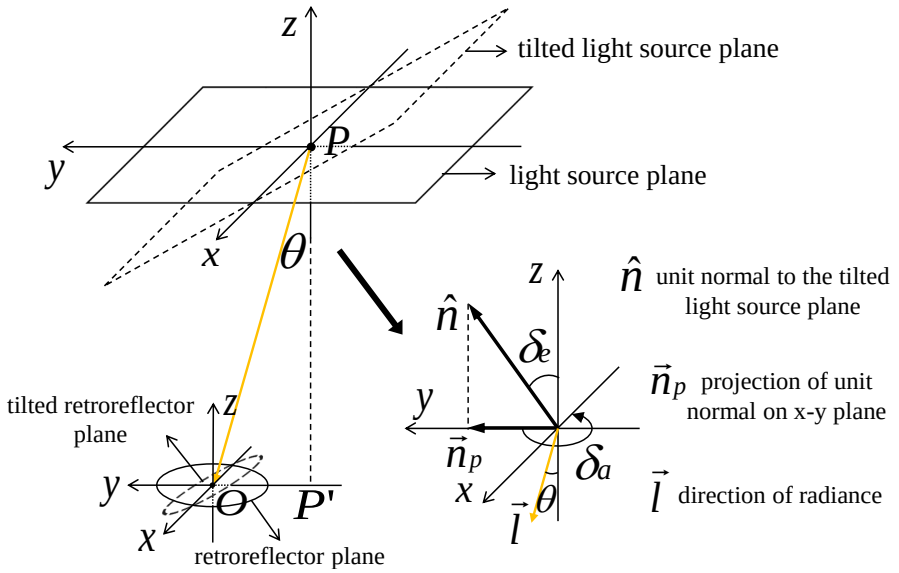

Figure 6.7 A virtual light source plane illustrates Theorem 2.

the light source. If the retroreflector changes its orientation and its front face is on a tilted retroreflector plane, we create a virtual tilted light source plane, which is parallel to the tilted retroreflector plane. The intersection line of the real light source plane and the virtual tilted light source plane crosses point P. Now we can perform the same analysis as that in case 1 (i.e., when $\delta_e = 0$ and $\delta_a = 0$) on the tilted light source plane based on the new incidence angle to the front face of tilted retroreflector, which is formed by the normal $\hat{n}$ to the tilted retroreflector plane and $\overrightarrow{OP}$). Therefore, the size of a virtual effective reflecting area S on the tilted light source plane can be derived from (6.6).

The virtual effective reflecting area S on the tilted light source plane contains a set of rays that can be retroreflected back to the PD. These rays are approximated to be parallel to $\overrightarrow{PO}$. In order to figure out the effective reflecting area S' on the real light source plane, we need to derive the oblique projection of S on the real light source plane along the direction of $\overrightarrow{PO}$. As shown in Figure 6.7, in the coordinate system of light source, $\hat{n}$ is the unit normal to the tilted light source plane, and $\overrightarrow{n_p}$ is the projection of $\hat{n}$ on x-y plane.

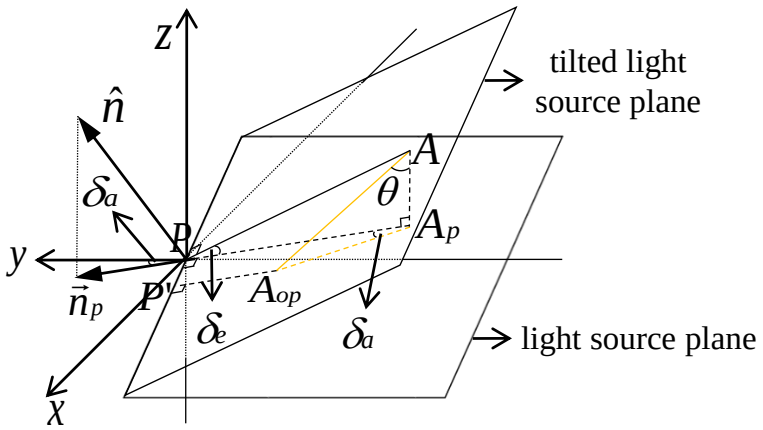

Figure 6.8 Point A is on the tilted light source plane and its oblique projection A_{op} is on the light source plane.

Elevation angle δ_e is formed by $\hat{n}$ and z axis, azimuth angle δ_a is formed by $\overrightarrow{n_p}$ and y axis, $\overrightarrow{l}$ denotes the direction of $\overrightarrow{PO}$, and radiance angle θ is formed by $\overrightarrow{l}$ and z axis.

Theorem 5. *Given θ, δ_e and δ_a, the ratio of S' and S, β, is equal to $cos\delta_e - sin\delta_e tan\theta cos\delta_a$.*

Proof. In Figure 6.8, point A is on the tilted light source plane, point A_p is the projection of point A on the real light source plane, and point A_{op} is the oblique projection of point A on the real light source plane along the direction of $\overrightarrow{l}$. $\overline{AP}$, $\overline{A_pP}$ and $\overline{A_{op}P'}$ are all perpendicular to the intersection line of the real light source plane and the virtual tilted light source plane. The direction of $\overrightarrow{A_pP}$ is the same as that of $\overrightarrow{n_p}$. Therefore, $\angle APA_p = \delta_e$, $\angle A_{op}AA_p = \theta$, $\angle PA_pA_{op} = \delta_a$. It can be proved by the principle of calculus that $\frac{S'}{S} = \frac{\overline{A_{op}P'}}{\overline{AP}}$. Since $\overline{A_pP} = \overline{AP}cos\delta_e$, $\overline{A_pA_{op}} = \overline{AA_p}tan\theta = \overline{AP}sin\delta_e tan\theta$ and $\overline{A_{op}P'} = \overline{A_pP} - \overline{A_pA_{op}}cos\delta_a = \overline{AP}cos\delta_e - \overline{AP}sin\delta_e tan\theta cos\delta_a$, we have

$$\beta = \frac{S'}{S} = \frac{\overline{A_{op}P'}}{\overline{AP}} = \frac{\overline{AP}cos\delta_e - \overline{AP}sin\delta_e tan\theta cos\delta_a}{\overline{AP}}$$
$$= cos\delta_e - sin\delta_e tan\theta cos\delta_a \tag{6.8}$$

□

Substituting the incidence angle to the front face of the tilted retroreflector (i.e., formed by the normal $\hat{n}$ to the tilted retroreflector plane and $\overrightarrow{OP}$ in Figure 6.7) to (6.4) and (6.5), we can find out D and D_s for the tilted retroreflector. Substituting D and D_s for the tilted retroreflector to (6.6), we can find out the ratio of the effective reflecting area and the maximum effective reflecting area α on the virtual tilted light source plane. Therefore, the received optical power can be computed as follows

$$P_r = P_t \frac{(ml+1)A_s}{8\pi d^2} cos^{ml+1}\theta \alpha \beta. \tag{6.9}$$

6.3.4 Some Practical Concern

In practice, the retroreflector may not rotate around the center of its front face. As shown in Figure 6.9, the distance between the front face of the retroreflector and the rotation center is R. Therefore, the new vertical distance between the light source and the retroreflector is $h_{new} = h + R(1 - cos\delta_e)$. The new horizontal distance between the PD and the retroreflector is

$$\begin{aligned} v_{new} = \overline{O'P} &= \sqrt{(\overline{OP} + \overline{OO'}cos\delta_a)^2 + (\overline{OO'}sin\delta_a)^2} \\ &= \sqrt{(v + Rsin\delta_e cos\delta_a)^2 + (Rsin\delta_e sin\delta_a)^2} \end{aligned}$$

In order to recompute P_r in (6.9), we substitute h_{new} and v_{new} to (6.1)-(6.6) and (6.8), and get the new d, θ, α and β.

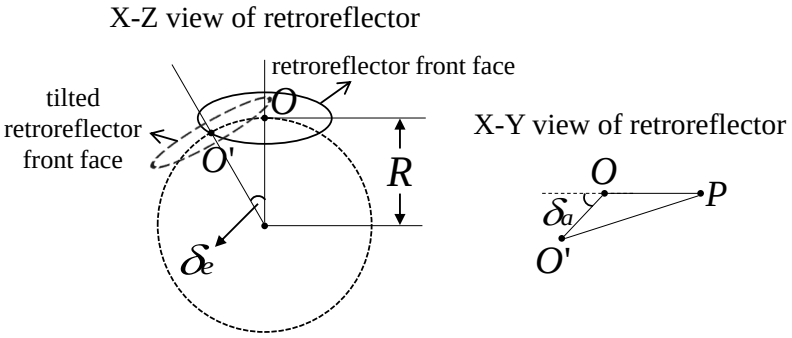

Figure 6.9 When rotation center is not coincident with the center of the front face of retroreflector.

6.4 Localization Algorithm

Given n PDs mounted on the light source plane, we can apply (6.9) to form constraints on measured received optical power and distances between the PDs and the retroreflector, as well as the azimuth and elevation angles of the retroreflector,

$$P_{ri} = P_t \frac{(ml+1)A_{si}}{8\pi {d_i}^2} cos^{ml+1}\theta_i \alpha_i \beta_i, i = 1, 2, ..., n. \tag{6.10}$$

Let the 3D coordinates of the retroreflector and the i-th PD be (x_0, y_0, z_0) and (x_i, y_i, z_i), respectively. We have the horizontal distance between the i-th PD and the retroreflector $v_i = \sqrt{(x_0 - x_i)^2 + (y_0 - y_i)^2}$ and the vertical distance between the light source plane and the front face of the retroreflector $h = |z_0 - z_i|$. Recall that the azimuth and elevation angles of the retroreflector are denoted by δ_a and δ_e, respectively. Therefore, there are five unknowns x_0, y_0, z_0, δ_a and δ_e when we estimate the position and orientation of the retroreflector. With five or more PDs with known 3D coordinates, we can uniquely determine all the five unknowns. Note that since the landmarks in RETRO system are PDs instead of light sources (i.e., landmarks in conventional VLC-based localization approaches), RETRO is able to locate devices with *any single unmodified* light source.

The localization is framed as an optimization process trying to minimize the sum of square errors between the left and right hand sides of each equation in (6.10),

$$\overrightarrow{s}_{opt} = \arg\min_{s} \sum_{i} f_i(\overrightarrow{s})^2,$$

where $\overrightarrow{s} = (x_0, y_0, z_0, \delta_a, \delta_e)$ and

$$f_i(\overrightarrow{s}) = P_{ri} - P_t \frac{(ml+1)A_{si}}{8\pi {d_i}^2} cos^{ml+1}\theta_i \alpha_i \beta_i, i = 1, 2, ..., n.$$

To accelerate the search process for the above non-linear least square optimization problem, the widely-used Levenberg-Marquardt algorithm [31] is adopted. Levenberg-Marquardt algorithm reduces the search space by searching along the direction of the gradient, which moves toward the local minimum. The initial values of unknowns are generated randomly and we run the localization algorithm several times to avoid local minima. The efficiency of the Levenberg-Marquardt algorithm is proved in [31], which can converge to a local minimum in several milliseconds. In our experiments, we show that the localization algorithm can generate very high location and orientation accuracy.

6.5 Experiment Based Validation of the Derivation of Received Optical Power

6.5.1 Testbed Settings

We utilize a flat LED panel with evenly distributed light as the light source, which is a commercial off-the-shelf (COTS) LED Troffer 2x2 FT (35W, 4000K, 3770 Lumens) provided by Hyperikon. To estimate $\psi_{1/2}$ of the LED panel, we manually restrict the effective illumination area to a small spot and find out that $\psi_{1/2} = 33°$, and the Lambertian index $ml = -\frac{ln2}{ln(cos\psi_{1/2})}$. The circular retroreflector PS976 (uncoated) is manufactured by

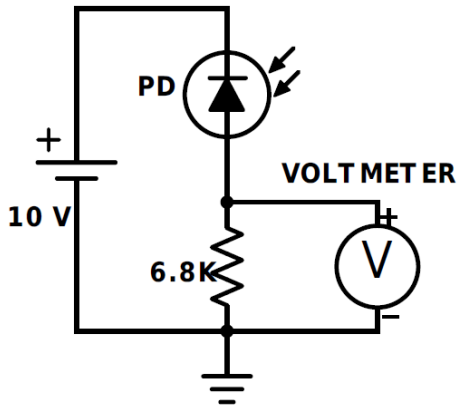

Figure 6.10 Light intensity measurement circuit.

Thorlabs [99]. The substrate material is BK7 grade A, according to [100], with a refractive index $n = 1.51$ for visible light wavelength. According to [99], the length of retroreflector $L = 35.7\ mm$, the length of ressesion $L_s = 6.3\ mm$ and the diameter of the front face of retroreflector $r = 50\ mm$. The PD S6968 is provided by Hamamatsu Photonics [101], and $A_s = 150\ mm^2$. The value of P_t is estimated by fitting the measurements at different heights to the theoretical values.

The PD works in photoconductive mode to measure the light intensity. As shown in Figure 6.10, the PD is driven by a 10 V DC and cascaded with a 6.8kΩ resistor. The received optical power P_r is linearly proportional to the output voltage of the resistor, which is measured by a multimeter. To get rid of the environmental reflection, we use an opaque chip to cover the front face of the retroreflector and measure the output voltage generated by environmental reflection, then we remove the opaque chip to measure the amount of output voltage contributed by the reflection of the retroreflector. We fix the retroreflector on a tripod to perform measurements at different locations and orientations. The testbed is shown in Figure 6.12.

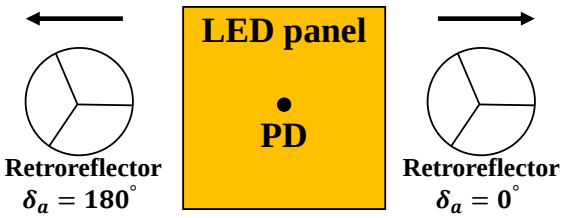

Figure 6.11 Explanation of light leaking problem (only when $\delta_a = 0°$, total internal reflection property stands when v increases).

6.5.2 Experiment Results

When we perform the measurement of the received optical power without changing the orientation (i.e., zero-value elevation and azimuth angles), we keep the retroreflector at certain height and increase the horizontal distance between the PD and the retroreflector. We observe that the output voltage drops suddenly to zero at a certain horizontal distance when the azimuth angle is non-zero. As shown in Figure 6.11, if the azimuth angle is 0°, as the horizontal distance increases, the output voltage decreases smoothly; while if the azimuth angle is 180°, the output voltage suddenly drops to zero when the horizontal distance increases to a certain value. This phenomenon contradicts the isotropic property of circular retroreflectors. After experimentally studying the retroreflector and communicating with the technical support from Thorlabs, we confirm that the reason for the an-isotropic phenomenon is due to the light leaking problem of the three mutually perpendicular reflecting surfaces. If the angle of incidence (AOI) to one of the three reflecting surfaces is too small, light will be leaking out of the surface instead of being reflected; thus, the total internal reflection (TIO) does not stand anymore. However, the light leaking problem is not a fundamental problem of retroreflectors and can be resolved by re-fabricating three reflecting surfaces to let them reflect as mirrors. Therefore, the

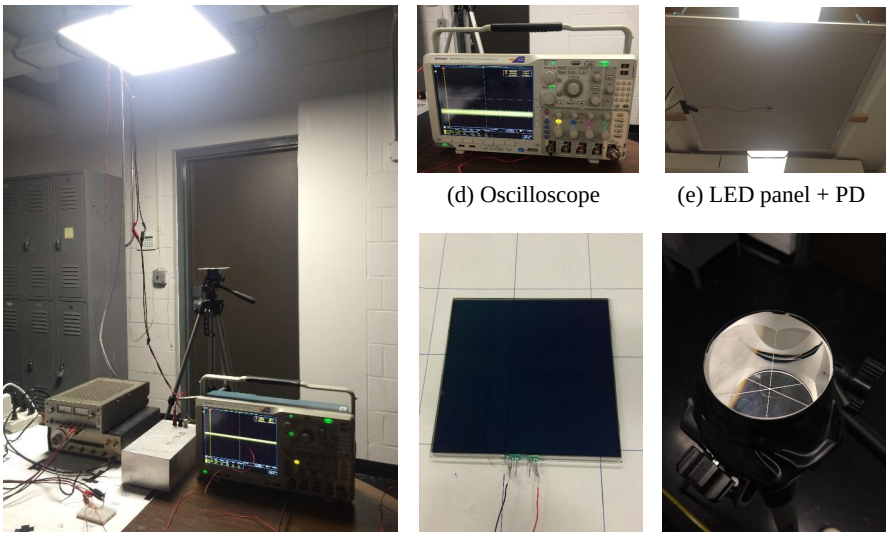

(a) Testbed (b) LCD shutter (c) Retroreflector

(d) Oscilloscope (e) LED panel + PD

Figure 6.12 Testbed.

isotropic property can hold such that the circular retroreflector is suitable for localization.

To circumvent the light leaking problem, we perform all the experiments at zero azimuth angle, in which case the AOI to each reflecting surface will not be small enough to cause light leaking. To validate the theory in case 1 (Equation (6.7)), we measure the output voltage at 4 different heights; namely, 1 meter, 1.18 meters, 1.35 meters and 1.52 meters. For each height, the measurement is performed at horizontal distances from 0 cm to 90 cm at intervals of 2 cm. The results are shown in Figure 6.13. To validate the theory in case 2 (Equation (6.9)), we measure the output voltage at fixed height 1 meter and 4 different horizontal distances; namely, 0 cm, 10 cm, 20 cm and 30 cm. For each horizontal distance, the elevation angle δ_e is varied from 0° to 30° at intervals of 2°. The results are shown in Figure 6.14. Since the experiment results match the theoretical results very well, we can safely conclude that the closed-form expression of received optical power is a very accurate approximation to practical measurements.

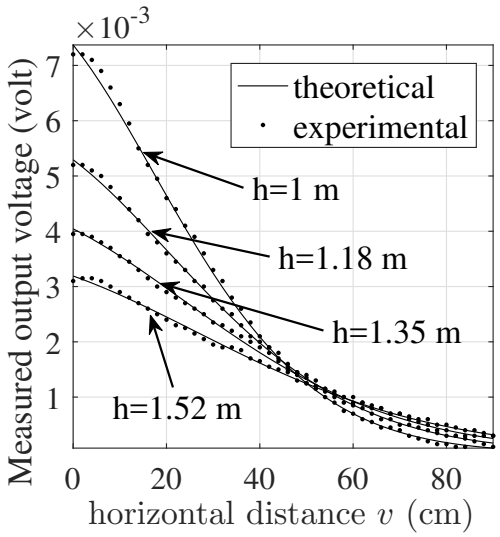

Figure 6.13 Theoretical and experimental results of zero-value elevation and azimuth angles setting.

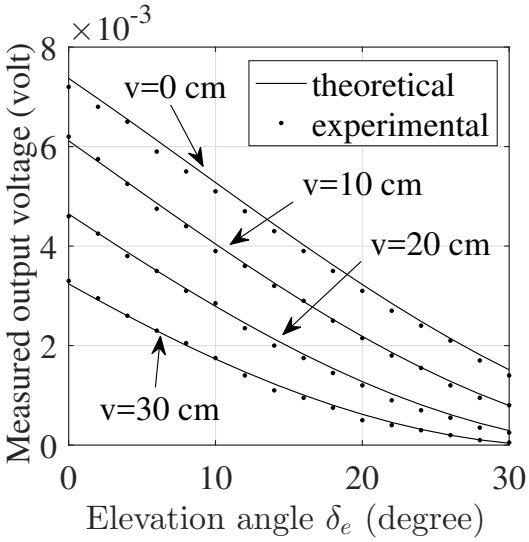

Figure 6.14 Theoretical and experimental results of arbitrary-value elevation and azimuth angles setting.

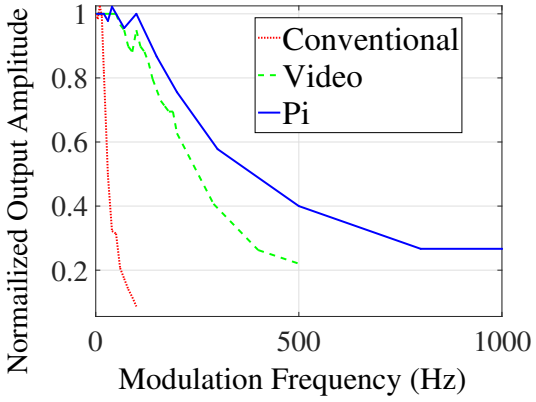

Figure 6.15 Signal amplitude vs. modulation frequency for three types of LCD shutters.

6.6 Experiment Based Evaluation of Localization and Orientation Accuracy

6.6.1 Applying LCD Shutter

In practice, in order to distinguish the reflected light from multiple IoT devices and from environmental reflection, instead of passive opaque chip, an active LCD shutter can be used to cover the front face of retroreflector to modulate the retroreflected light [26, 90]. By transitioning between transparent and opaque states, LCD shutter can generate a square wave signal at low modulation frequency. To investigate the relationship between signal amplitude and modulation frequency, we place three types of LCD shutter (i.e., conventional, video and Pi-cell) between a small LED light bulb and a photodetector (PDA36A from Thorlabs) to measure the signal amplitude. The results are shown in Figure 6.15, it can be seen that the signal amplitude decreases quickly for all three types of LCD shutter. This is due to the long response time (i.e., time cost by transitioning from one state to the other) of LCD shutters. Therefore, we choose a low modulation frequency (20 Hz) to drive the LCD shutter. Different modulation frequencies can be utilized to drive different LCD shutters in order to support multiple access of IoT devices. The capacity of the system and the impact on localization accuracy of mutual interference among different devices will be studied in the future.

In our experiments, Pi-cell is selected as the modulator. It is driven by a function generator. Note that the power consumption of the LCD shutter and its driver circuit is at tens of μW, which is also validated in [26, 90]. Instead of connecting the light intensity measurement circuit to a multimeter, we connect it to an oscilloscope (Tektronix MDO4034-3) and set the sampling rate to 1 MS/s. The recorded data is processed in MATLAB through Fast Fourier Transform (FFT) to compute the signal amplitude. Denote

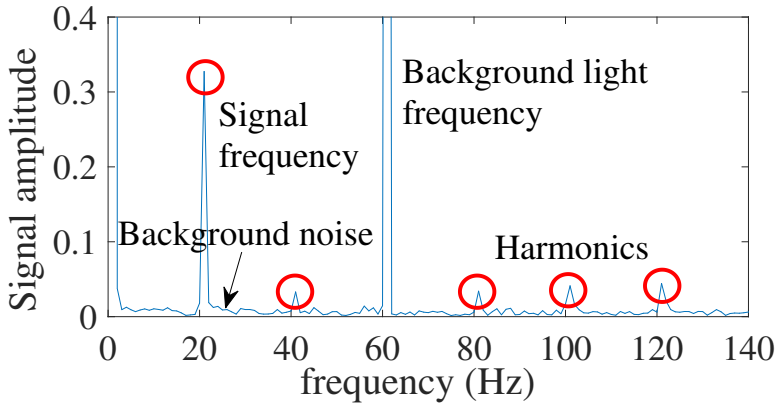

Figure 6.16 FFT plot of received signal (low background noise).

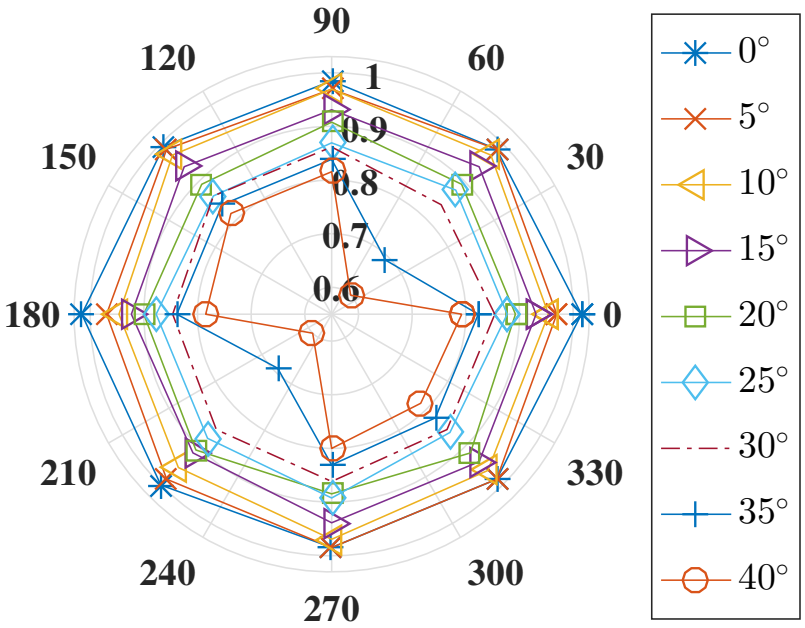

Figure 6.17 Normalized signal amplitude vs. different viewing angles.

the FFT length by N, the amplitude of the 1st harmonics in frequency domain by A_f and the amplitude of the square wave in time domain by A_t, we have $A_f = A_t/(N/2)$. In Figure 6.16, we show the FFT plot including retroreflected optical signal (20 Hz) and background light (60 Hz). We can observe that the background noise is much less than the 20 Hz signal amplitude, which enables reliable signal amplitude estimation at the modulation frequency of LCD shutter.

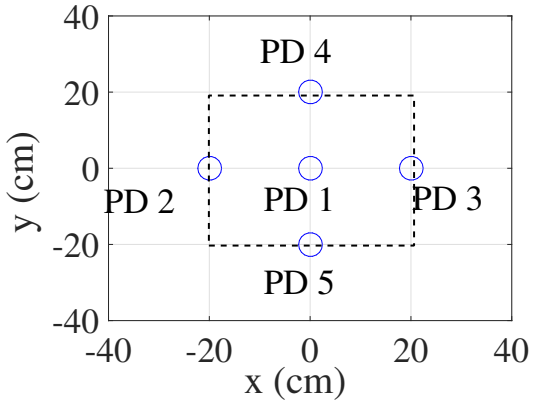

Figure 6.18 XY view (top) of PDs in grid structure.

Besides the modulation frequency, viewing angle also affects the amplitude of the signal produced by LCD shutter. We place the Pi-cell between a small light bulb and a photodetector (PDA36A from Thorlabs) at 8 values of azimuth angles (i.e., 0°, 45°, 90°, 135°, 180°, 225°, 270° and 315°) and 9 values of elevation angles (i.e., 0°, 5°, 10°, 15°, 20°, 25°, 30°, 35° and 40°) to measure the signal amplitude. The results are shown in Figure 6.17. When the elevation angle is not larger than 30°, the variation of signal amplitudes for different azimuth angles is very small. However, when the elevation angle increases above 30°, the signal amplitudes at azimuth angle of 45° and 225° are much lower than those at other azimuth angles. Therefore, the isotropic property of circular retroreflector may not hold when the incidence angle to the front face of retroreflector is larger than 30°. This issue can be resolved by selecting the closest PDs to perform localization, but it still restricts the orientation range to some extent. Another solution might be using dispersion film instead of LCD shutter, such that the viewing angle issue does not exist. However, the properties and limitations of dispersion film need to be studied thoroughly in the future. In Figure 6.17, we can also observe that as the elevation angle of Pi-cell increases from 0° to 30°, the signal amplitude decreases. We use a linear

function $\gamma(\theta) = 1 - 0.005\theta$ to approximate the attenuation caused by the viewing angle of Pi-cell, where θ is the incidence angle to the front face of the retroreflector. To compute the received optical power using (6.9), the right hand side of the equation needs be multiplied by γ^2 since the light rays pass through the Pi-cell twice.

6.6.2 Grid Structure Photodiodes Based Localization Accuracy

Recall that the light leaking problem restricts all the received signal amplitude measurements at zero azimuth angle (Figure 6.11). The problem can be handled by manufacturing a corner-cube with three reflecting surfaces as normal mirrors. However, we are using the COTS corner-cube retroreflector, which is designed for laser based applications. Due to the intrinsically isotropic property of circular corner-cube retroreflectors, the light leaking problem caused by laser application-oriented COTS product manufacturing does not hinder the evaluation of localization accuracy. We apply the measurement results using one PD to a realistic localization system, where multiple PDs are mounted on the LED panel in a grid structure with intervals of 20 cm. A central controller is used to monitor the signal amplitudes from all the PDs. Once the central controller detects the signal at certain frequency (20 Hz in our experiment), it selects the PD, whose output signal amplitude is the largest, as the central one and uses the other 4 PDs around the central one to perform the localization algorithm. As shown in Figure 6.18, the area within the dashed-line square is the region, in which we are evaluating the localization accuracy when the elevation and the azimuth angles of the retroreflector are both zero.

We select 400 positions uniformly within the dashed-line square region and compute the corresponding horizontal distances to each PD. Then we perform the signal amplitude

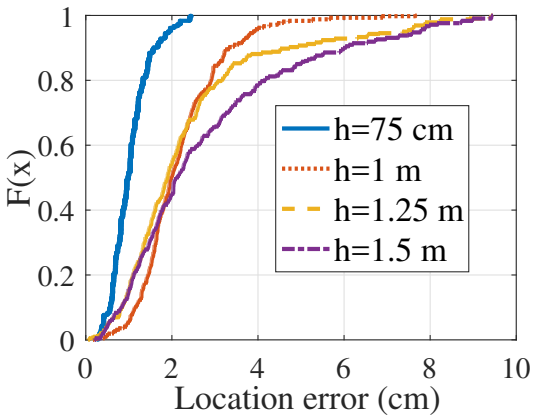

Figure 6.19 Empirical CDF of 3D location error.

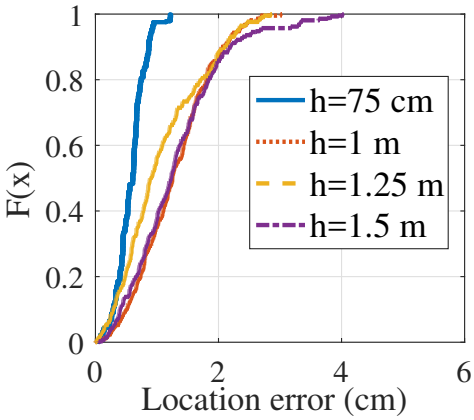

Figure 6.20 Empirical CDF of 2D location error.

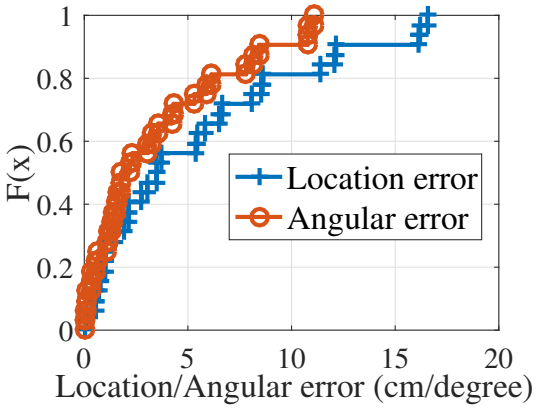

Figure 6.21 Empirical CDF of 3D location and orientation error.

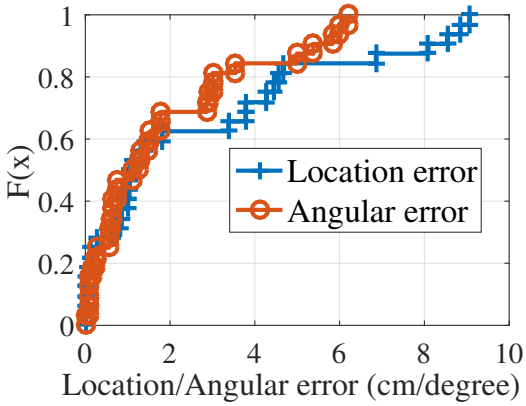

Figure 6.22 Empirical CDF of 2D location and orientation error.

measurement using one PD at all horizontal distances. After we measure the signal amplitudes at four different heights (75 cm, 1 m, 1.25 m and 1.5 m), we input them to the RSSI and trilateration based localization algorithm (Section 6.4) to evaluate the localization accuracy. In Figure 6.19, we apply our algorithm for 3D localization, in which the height is unknown, and we can observe that, at the height of 1.5 m, the location errors are less than 6 cm in 90% of the cases and the median error is only 2 cm. In Figure 6.20, the height is known, at the height of 1.5 m, the location errors are less than 2 cm in 90% of the cases and the median error is only 1 cm.

Table 6.1 Comparison with VLC-based Localization Systems. N/E Stands for Not Evaluated. FP and AoA are Fingerprinting and Angle-of-arrival, respectively.

System	Epsilon	Luxapose	PIXEL	Litell	Navilight	RETRO
Reference	[29]	[30]	[31]	[32]	[33]	[this]
Location accuracy (90%)	0.4 m	0.1 m	0.3 m	0.1 m	1 m	2 cm
Orientation accuracy	N/A	3°	N/E	N/A	N/A	1°
Method	Model	AoA	AoA	FP	FP	Model
Database	No	Yes	Yes	Yes	Yes	No
Unmodified infrastructure	No	No	Yes	Yes	Yes	Yes
Require multiple light sources	Yes	Yes	No	No	No	No
Require camera	No	Yes	Yes	Yes	Yes	No

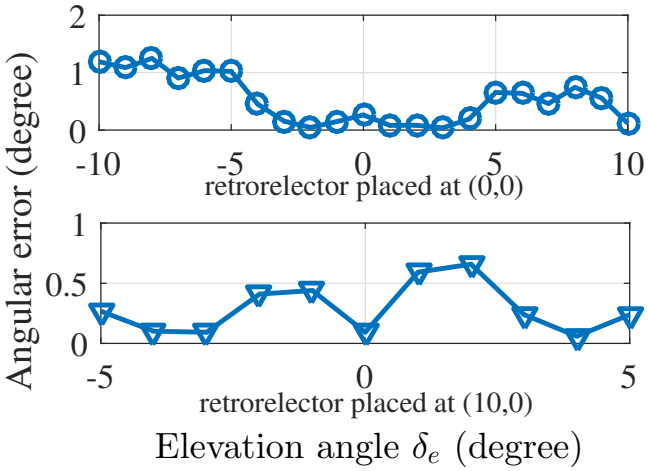

Figure 6.23 Orientation error when the location is known.

To evaluate both the location and the orientation accuracy, due to the light leaking problem and viewing angle restriction, we only consider PD1, PD2 and PD3 in Figure 6.18 to evaluate the elevation angle accuracy when the retroreflector is placed at (0,0) and (10,0) where the height is 1 meter. Note that the viewing angle restriction to valid orientation detection range might be resolved by utilizing dispersion film which needs to be investigated thoroughly, or by leveraging a gyroscope and sending the detected orientation information back to the tracking system via the uplink enabled by the retroreflector. We vary the elevation angle from -10° to 10° when the retrorelector is placed at (0,0) and vary the elevation angle from -5° to 5° when the retroreflector is placed at (10,0). In Figure 6.21, we apply our 3D localization algorithm, in which the height is unknown, 90% of the location errors are less than 12 cm and 80% of the angular errors are less than 6°, the median location and angular errors are 3 cm and 2°, respectively. In Figure 6.22, the height is known, 80% of the location errors are less than 5 cm and 80% of the angular errors are less than 3°, the median location and angular errors are 1 cm and 1°, respectively. As far as we know, in VLC-based localization systems, Luxapose [30] is the only system that both enables the tracking of devices' orientation and evaluates the orientation accuracy. In our 3D location and orientation results (Figure 6.21), using simple and cheap PDs, we are able to achieve parity with the 2D location and orientation results (i.e., height is known) of systems such as Luxapose [30] that requires CMOS imager and heavy computation to obtain angle-of-arrival (AOA) information. In our 2D location and orientation results (Figure 6.22), we are able to achieve 40% improvement in both location and orientation accuracy compared to Luxapose.

In Figure 6.23, we only evaluate the orientation error from localization. Compared to Luxapose [30], in which the angle error falls in 3° when only orientation is evaluated, we are able to achieve 60% improvement in terms of orientation accuracy. In addition, Luxapose [30] requires four or five customized light beacons to be visible for a camera to achieve decimeter-level location accuracy and roughly 3° orientation error. However, by relying on only one *single unmodified* light source, RETRO extends the available localization area, within which centimeter-level location accuracy and 1° orientation error can be achieved without requiring computation and heavy sensing, like camera, on the device.

6.7 Related Work

RF-based localization approaches. The localization accuracy (less than 1 meter) of RFID [102] depends on densely deployed RFID readers, which are very expensive. Utilizing existing infrastructure, WiFi-based localization [103, 104] can locate devices within large range (e.g., 150 meters). Although in the most recent WiFi-based localization works [103, 104], authors claim that the WiFi-based localization approach can achieve decimeter-level accuracy, the location error reaches to 2 meters at the 80th percentile, which can cause destructive outcome for some location error sensitive applications. Bluetooth low energy (BLE), such as iBeacon [105], is intrinsically low frequency radio (i.e., use the same spectrum as WiFi) and therefore, the location error can still reach to meter-level and the interference to WiFi-based user devices is considerable. Ultra-wideband (UWB)-based localization [106] is able to achieve location precision within tens of centimeters. Nevertheless, the high cost of hardware, shorter battery lifetime

than BLE, and lack of interaction with the current devices render UWB-based localization not being used universally.

VLC-based localization approaches. Existing VLC based localization works are not suitable for real-time tracking of passive IoT devices not only because of the absence of backward channel. Epsilon [29] and Luxapose [30] require modified light infrastructure by adding extra driver circuit. Litell [32] requires specific unmodified light source like fluorescent lamp. Luxapose [30] and PIXEL [31] require a power-consuming camera facing upward to keep capturing images containing enough landmarks. Navilight [33] requires the object to move for a certain distance to collect light intensity pattern. Based on existing light infrastructure with any unmodified light source, RETRO is capable of locating the position and detecting the orientation of any passive IoT devices with ultra-low power and no camera, expensive sensor, or computational capability at the devices. Although [31–33] are able to execute localization based on a single light source, they either necessitate camera to enable image processing [31, 32], or cannot locate static objects [33]. Utilizing a single light source, RETRO can achieve centimeter-level location accuracy and single-digit orientation error. For a typical retail setting with ceiling lamps, the localization performance can be achieved every few meters, perhaps with dead reckoning filling in the gaps. A comparison with VLC-based localization systems is summarized in Table 6.1.

6.8 Conclusion

In this chapter, we propose and prototype RETRO, which to the best of our knowledge for the first time enables backward channel from the object to landmarks for VLC-based

localization systems. Embracing all the advantages of VLC-based localization approach, such as high accuracy, orientation sensitivity, no interference to RF-based devices, RETRO is capable of utilizing any single unmodified light source to execute real-time tracking of location and orientation of any passive IoT devices with ultra-low power and no computational capability at the devices. A set of extensive experimental results demonstrate that RETRO achieves remarkably good performance, and centimeter-level location error (i.e., less than 2 cm location error at 90% of the time) as well as up to 1° orientation error.

CHAPTER 7

SUMMARY AND FUTURE DIRECTIONS

7.1 Summary

As an alternative indoor wireless access technology, VLC embraces advantages including wide unlicensed bandwidth, no interruption to RF-based applications, jointly performing illumination and communication, ubiquitous infrastructure, and energy-efficient data transmission. In this dissertation, we study the heterogeneous integration of such directional wireless medium usage into the next generation wireless networks, which requires careful design of PHY and MAC layers to address the challenges of VLC.

One major challenge of VLC is the absence of uplink channel. Ubiquitously deployed lighting infrastructure can only provide downlink data transmission while the uplink VLC requires energy-constrained mobile devices to turn on additional light sources, which may also result in alignment and glaring issues. To overcome the uplink challenge, in Chapter 2, we design and implement a hybrid WiFi-VLC system, in which a WiFi channel is utilized to supplement the uplink data transmission. The asymmetric system design (i.e., the uplink wireless access technology is different from the downlink one) has two main problems that need to be resolved. One problem is the IP traffic flow redirection and the other one is a single duplex communication link operated by two separated network interface card. We rely on IP static routing to address the first problem and devise an operating system spoofing method to tackle the second problem. To further enhance the system capacity in situations where uplink VLC is available, we implement

an aggregated system based on Linux bonding driver that achieves the addition bandwidth of WiFi and VLC links.

System delay is a critical QoS metric in heterogeneous system design. In Chapter 3, we study the optimization of average system delay in heterogeneous RF-VLC networks and evaluate the minimum average system delay under two configurations: i) non-aggregation – any request is either allocated to RF or VLC; ii) aggregation – each request is split into two pieces, one is forwarded to RF, and the other is forwarded to VLC. Different practical network settings are considered, such as contention and backoff based WiFi network, centralized resource allocation based RF femtocells, and VLC with blockage. The main results reveal that aggregation setting may not be beneficial in terms of minimum average system delay in a contention based crowded network.

The dual use nature of VLC allows it to jointly perform illumination and communication, yet given the same emitted optical power, communication consumes additional total power due to the switching loss in driver circuitry. In Chapter 4, we formulate an optimization problem of minimizing the total power consumption in a multi-user VLC indoor network taking into account the constraints of user traffic demands and illumination requirements. Considering the large number of variables and the sparsity of non-zero variables in the optimal solution, we apply the efficient column generation method along with an ϵ-bounded termination condition to resolve the optimization problem.

VLC backscatter is a new reflection based communication approach that enables ultra-low power consumption for IoT applications. Nevertheless, the state-of-the-art VLC backscatter's link capacity is limited by the effective modulation bandwidth of LCD shutter. In Chapter 5, we propose and prototype a novel pixelated VLC backscatter system.

Instead of sending the optical signal by one set of modulator (i.e., LCD shutter) and reflector, multiple sets of modulator and reflector are operated independently to generate multi-level signals, which enables more advanced modulation scheme than the OOK scheme, such as PAM and OFDM, and orthogonal multiple access.

In VLC based localization system, the absence of uplink channel limits the state-of-the-art approaches to client-based localization which leads the heavy computation and sensing burden on the IoT devices. In Chapter 6, we apply the VLC-backscattering concept to VLC localization. Multiple PDs mounted on an unmodified single light source act as landmarks. A circular corn-cube retroreflector along with a LCD shutter are equipped on the IoT device to produce the location and orientation signatures. Based on geometry analysis and mathematical derivation, we model the path loss of retroreflection. Combining the path loss of free space optical propagation and retroreflection, RSSI and trilateration technique is utilized to locate the IoT devices without computation and sensing requirements on the devices.

7.2 Future Direction

The current hybird WiFi-VLC system design either operates in an asymmetric mode (i.e, WiFi uplink and VLC downlink) or in an aggregation mode (i.e., two duplex WiFi and VLC links). One future direction is to integrate these two modes in one system, enhance the flexibility of link capacity usage and simplify the system configuration. Integration of the asymmetric mode and the aggregation mode will allow the client device to fully utilize the available channels and keep VLC in a practical setting. Adjusting the link capacity utilization in an adaptive manner will enable the realistic network level optimization in

a multi-user scenario. The system simplification is also important since it improves the compatibility and makes the system easy to be implemented in other research institutes for measurements and evaluations.

The initial attempt of applying VLC-backscattering concept to localization system is based on a single circular corner-cube retroreflector and a flat LED panel with light evenly distributed on the light emitting surface. Taking into account accuracy of model, reflection factor, weight, size and distinguishability of different locations and orientations, different types of retroreflector (e.g., corner-cube retroreflector array, retroreflective sheet and retroreflective spray paint) will be investigated to understand the pros and the cons of each type of retroreflector and have a clear vision about the appropriate application scenarios of each type of retroreflector. The accuracy of modeling light distribution and light emission pattern will directly affect the accuracy of the RSSI and trilateration based localization. To accurately model these two factors, we will study different types of lamps that are generally used for indoor illumination. The modeling process needs to take into account the placement of original light source (e.g., LED arrays, fluorescent tubes and incandescent bulbs), the internal reflection and the scattering effect of lighting infrastructure frames. If the emission pattern is not isotropic, additional compensation functions need to be applied to correlate the received optical power of PDs and the retroreflector's location coordinates.

LCD shutter is adopted in our prototyped retroreflected based localization system. Although the LCD shutter along with the driver circuitry only consume around 200 μW, it still needs a power harvesting circuit to support the reflected signal modulation. One future direction is to eliminate the electronically driven components on the IoT devices by

utilizing cheap and light-weight dispersers to produce location and orientation signatures. The main operational principle is – the retroreflected unpolarized white light first passes through a polarizer and becomes polarized white light, then a disperer is added to disperse the polarized white light by distributing different colors on different polarization, another polarizer is placed at the received side to capture the chromatic light that can be quantified using a vector in RGB domain (i.e., color). One way to generate location signatures is utilizing grid structure dispersers to project different polarization patterns on the user plane.

REFERENCES

[1] M. Kavehrad, "Optical wireless applications: A solution to ease the wireless airwaves spectrum crunch," in *Broadband Access Communication Technologies Vii*. International Society for Optics and Photonics, 2013, pp. 86 450G–86 450G.

[2] J. M. Kahn and J. R. Barry, "Wireless infrared communications," *Proceedings of the IEEE*, vol. 85, no. 2, pp. 265–298, 1997.

[3] T. Komine and M. Nakagawa, "Fundamental analysis for visible-light communication system using LED lights," *IEEE Transactions on Consumer Electronics*, vol. 50, no. 1, pp. 100–107, 2004.

[4] S. Rajagopal, R. D. Roberts, and S.-K. Lim, "IEEE 802.15. 7 visible light communication: modulation schemes and dimming support," *IEEE Communications Magazine*, vol. 50, no. 3, pp. 72–82, 2012.

[5] M. B. Rahaim, A. M. Vegni, and T. D. Little, "A hybrid radio frequency and broadcast visible light communication system," in *IEEE Global Communications Conference (GLOBECOM) Workshops*, 2011, pp. 792–796.

[6] C. Lee, C. Tan, H. Wong, and M. Yahya, "Performance evaluation of hybrid VLC using device cost and power over data throughput criteria," in *Ultrafast Imaging and Spectroscopy*. International Society for Optics and Photonics, 2013, pp. 88 451A–88 451A.

[7] H. Chowdhury, I. Ashraf, and M. Katz, "Energy-efficient connectivity in hybrid radio-optical wireless systems," in *International Symposium on Wireless Communication Systems (ISWCS)*. VDE, 2013, pp. 1–5.

[8] Z. Huang and Y. Feng, "Design and demonstration of room division multiplexing-based hybrid VLC network," *Chinese Optics Letters*, vol. 11, no. 6, p. 060603, 2013.

[9] S. Schmid, G. Corbellini, S. Mangold, and T. R. Gross, "LED-to-LED visible light communication networks," in *ACM International Symposium on Mobile ad hoc Networking and Computing*, 2013, pp. 1–10.

[10] K.-D. Langer and J. Grubor, "Recent developments in optical wireless communications using infrared and visible light," in *IEEE International Conference on Transparent Optical Networks (ICTON)*, vol. 3, 2007, pp. 146–151.

[11] A. L. Ramaboli, O. E. Falowo, and A. H. Chan, "Bandwidth aggregation in heterogeneous wireless networks: A survey of current approaches and issues," *Journal of Network and Computer Applications*, vol. 35, no. 6, pp. 1674–1690, 2012.

[12] W. C. Jakes and D. C. Cox, *Microwave mobile communications*. New York: Wiley-IEEE Press, 1994.

[13] L. X. Cai, L. Cai, X. S. Shen, and J. W. Mark, "REX: a randomized exclusive region based scheduling scheme for mmWave WPANs with directional antenna," *IEEE Transactions on Wireless Communications*, vol. 9, no. 1, pp. 113–121, 2010.

[14] S. Wu, H. Wang, and C.-H. Youn, "Visible light communications for 5G wireless networking systems: from fixed to mobile communications," *IEEE Network*, vol. 28, no. 6, pp. 41–45, 2014.

[15] L. Wilson, "What are the major uses of electricity?" http://shrinkthatfootprint.com/how-do-we-use-electricity, [Online; accessed 1-April-2015].

[16] Cisco, "Internet of Things (IoT)," http://www.cisco.com/c/en/us/solutions/internet-of-things/overview.html, [Online; accessed 1-May-2015].

[17] D. Hanchard, "FCC chairman forecasts wireless spectrum crunch," https://www.zdnet.com/article/fcc-chairman-forecasts-wireless-spectrum-crunch/, [Online; accessed 1-May-2015].

[18] S. Priya and D. J. Inman, *Energy harvesting technologies*. New York: Springer, 2009, vol. 21.

[19] S. Chia, M. Gasparroni, and P. Brick, "The next challenge for cellular networks: backhaul," *IEEE Microwave Magazine*, vol. 10, no. 5, pp. 54–66, 2009.

[20] B. Kellogg, A. Parks, S. Gollakota, J. R. Smith, and D. Wetherall, "Wi-Fi Backscatter: Internet connectivity for RF-powered devices," in *ACM SIGCOMM Computer Communication Review*, vol. 44, no. 4, 2014, pp. 607–618.

[21] D. Bharadia, K. R. Joshi, M. Kotaru, and S. Katti, "BackFi: High throughput wifi backscatter," *ACM SIGCOMM Computer Communication Review*, vol. 45, no. 4, pp. 283–296, 2015.

[22] V. Liu, A. Parks, V. Talla, S. Gollakota, D. Wetherall, and J. R. Smith, "Ambient backscatter: wireless communication out of thin air," *ACM SIGCOMM Computer Communication Review*, vol. 43, no. 4, pp. 39–50, 2013.

[23] D. N. Mansell, P. S. Durkin, G. N. Whitfield, and D. W. Morley, "Modulated-retroreflector based optical identification system," Dec. 10 2002, US Patent 6,493,123.

[24] T. Komine, S. Haruyama, and M. Nakagawa, "Bidirectional visible-light communication using corner cube modulator," *IEIC Technical Report102*, pp. 41–46, 2003.

[25] E. Rosenkrantz and S. Arnon, "Modulated retro reflector for VLC applications," in *Laser Communication and Propagation through the Atmosphere and Oceans III*. International Society for Optics and Photonics, 2014, pp. 922 414–922 414.

[26] J. Li, A. Liu, G. Shen, L. Li, C. Sun, and F. Zhao, "Retro-VLC: Enabling battery-free duplex visible light communication for mobile and IoT applications," in *ACM International Workshop on Mobile Computing Systems and Applications*, 2015, pp. 21–26.

[27] "Liquid Crystal Technologies," http://www.liquidcrystaltechnologies.com/products/LCDShutters.htm, [Online; accessed 1-May-2015].

[28] Wikipedia, https://en.wikipedia.org/wiki/Real-time_locating_system, [Online; accessed 4-May-2017].

[29] L. Li, P. Hu, C. Peng, G. Shen, and F. Zhao, "Epsilon: A Visible Light Based Positioning System," in *USENIX Symposium on Networked Systems Design and Implementation (NSDI)*, 2014, pp. 331–343.

[30] Y.-S. Kuo, P. Pannuto, K.-J. Hsiao, and P. Dutta, "Luxapose: Indoor positioning with mobile phones and visible light," in *ACM International Conference on Mobile Computing and Networking (MobiCom)*, 2014, pp. 447–458.

[31] Z. Yang, Z. Wang, J. Zhang, C. Huang, and Q. Zhang, "Wearables can afford: Light-weight indoor positioning with visible light," in *ACM International Conference on Mobile Systems, Applications, and Services (MobiSys)*, 2015, pp. 317–330.

[32] C. Zhang and X. Zhang, "LiTell: Robust indoor localization using unmodified light fixtures," in *ACM International Conference on Mobile Computing and Networking (MobiCom)*, 2016, pp. 230–242.

[33] Z. Zhao, J. Wang, X. Zhao, C. Peng, Q. Guo, and B. Wu, "NaviLight: Indoor Localization and Navigation Under Arbitrary Lights," in *IEEE International Conference on Computer Communications (INFOCOM)*, 2017.

[34] T. Li, C. An, Z. Tian, A. T. Campbell, and X. Zhou, "Human sensing using visible light communication," in *ACM International Conference on Mobile Computing and Networking (MobiCom)*, 2015.

[35] S. Shao, A. Khreishah, M. Ayyash, M. B. Rahaim, H. Elgala, V. Jungnickel, D. Schulz, and T. D. Little, "Design and analysis of a visible-light-communication enhanced WiFi system," *IEEE/OSA Journal of Optical Communications and Networking*, vol. 7, no. 10, pp. 960–973, 2015.

[36] D. Senie, "Using the SOCK-PACKET mechanism in Linux to gain complete control of an Ethernet interface," https://www.tldp.org/LDP/khg/HyperNews/get/khg/186/1.html, [Online; accessed 1-April-2015].

[37] S. Shao, A. Khreishah, M. B. Rahaim, H. Elgala, M. Ayyash, T. D. Little, and J. Wu, "An indoor hybrid WiFi-VLC Internet access system," in *IEEE International Conference on Mobile Ad Hoc and Sensor Systems (MASS)*, 2014, pp. 569–574.

[38] "Linux Ethernet bonding driver HOWTO," https://www.kernel.org/doc/Documentation/networking/bonding.txt, [Online; accessed 1-April-2015].

[39] G. Bianchi, L. Fratta, and M. Oliveri, "Performance evaluation and enhancement of the CSMA/CA MAC protocol for 802.11 wireless LANs," in *IEEE International Symposium on Personal, Indoor and Mobile Radio Communications (PIMRC)*, vol. 2, 1996, pp. 392–396.

[40] K.-D. Langer, J. Hilt, D. Shulz, F. Lassak, F. Hartlieb, C. Kottke, L. Grobe, V. Jungnickel, and A. Paraskevopoulos, "Optoelectronics & communications rate-adaptive visible light communication at 500Mb/s arrives at plug and play," *SPIE Newsroom*, 2013.

[41] L. Grobe, A. Paraskevopoulos, J. Hilt, D. Schulz, F. Lassak, F. Hartlieb, C. Kottke, V. Jungnickel, and K.-D. Langer, "High-speed visible light communication systems," *IEEE Communications Magazine*, vol. 51, no. 12, pp. 60–66, 2013.

[42] "Iperf," https://iperf.fr/, [Online; accessed 1-April-2015].

[43] G. P. Koudouridis, R. Agüero, E. Alexandri, J. Choque, K. Dimou, H. Karimi, H. Lederer, J. Sachs, and R. Sigle, "Generic link layer functionality for multi-radio access networks," in *IST Mobile and Wireless Communications Summit*, 2005.

[44] G. P. Koudouridis, H. R. Karimi, and K. Dimou, "Switched multi-radio transmission diversity in future access networks," in *IEEE Vehicular Technology Conference*, 2005, pp. 235–239.

[45] A. Yaver and G. P. Koudouridis, "Performance evaluation of multi-radio transmission diversity: QoS support for delay sensitive services," in *IEEE Vehicular Technology Conference*, 2009, pp. 1–5.

[46] J.-O. Kim, T. Ueda, and S. Obana, "MAC-level measurement based traffic distribution over IEEE 802.11 multi-radio networks," *IEEE Transactions on Consumer Electronics*, vol. 54, no. 3, pp. 1185–1191, 2008.

[47] J.-O. Kim, "Feedback-based traffic splitting for wireless terminals with multi-radio devices," *IEEE Transactions on Consumer Electronics*, vol. 56, no. 2, pp. 476–482, 2010.

[48] J.-O. Kim, P. Davis, T. Ueda, and S. Obana, "Splitting downlink multimedia traffic over WiMax and WiFi heterogeneous links based on airtime-balance," *Wireless Communications and Mobile Computing*, vol. 12, no. 7, pp. 598–614, 2012.

[49] S. Shao, A. Khreishah, and I. Khalil, "Joint link scheduling and brightness control for greening VLC-based indoor access networks," *IEEE/OSA Journal of Optical Communications and Networking*, vol. 8, no. 3, 2016.

[50] S. Shao and A. Khreishah, "Delay analysis of unsaturated heterogeneous omnidirectional-directional small cell wireless networks: The case of RF-VLC coexistence," *IEEE Transactions on Wireless Communications*, vol. 15, no. 12, pp. 8406–8421, 2016.

[51] N. Ding, D. Wagner, X. Chen, A. Pathak, Y. C. Hu, and A. Rice, "Characterizing and modeling the impact of wireless signal strength on smartphone battery drain," in *ACM SIGMETRICS Performance Evaluation Review*, vol. 41, no. 1, 2013, pp. 29–40.

[52] I. C. S. L. M. S. Committee *et al.*, "Wireless LAN medium access control (MAC) and physical layer (PHY) specifications," 1997.

[53] S. K. Nobar, K. A. Mehr, and J. M. Niya, "Comprehensive performance analysis of IEEE 802.15.7 CSMA/CA mechanism for saturated traffic," *IEEE/OSA Journal of Optical Communications and Networking*, vol. 7, no. 2, pp. 62–73, 2015.

[54] D. López-Pérez, A. Valcarce, G. De La Roche, and J. Zhang, "OFDMA femtocells: A roadmap on interference avoidance," *IEEE Communications Magazine*, vol. 47, no. 9, pp. 41–48, 2009.

[55] X. Kang, R. Zhang, and M. Motani, "Price-based resource allocation for spectrum-sharing femtocell networks: A stackelberg game approach," *IEEE Journal on Selected Areas in Communications*, vol. 30, no. 3, pp. 538–549, 2012.

[56] N. Saquib, E. Hossain, L. B. Le, and D. I. Kim, "Interference management in OFDMA femtocell networks: Issues and approaches," *IEEE Wireless Communications*, vol. 19, no. 3, pp. 86–95, 2012.

[57] H. Li, X. Xu, D. Hu, X. Qu, X. Tao, and P. Zhang, "Graph method based clustering strategy for femtocell interference management and spectrum efficiency improvement," in *IEEE International Conference on Wireless Communications Networking and Mobile Computing (WiCOM)*, 2010, pp. 1–5.

[58] H. Widiarti, S.-Y. Pyun, and D.-H. Cho, "Interference mitigation based on femtocells grouping in low duty operation," in *IEEE Vehicular Technology Conference*, 2010, pp. 1–5.

[59] H.-C. Lee, D.-C. Oh, and Y.-H. Lee, "Mitigation of inter-femtocell interference with adaptive fractional frequency reuse," in *IEEE International Conference on Communications (ICC)*, 2010, pp. 1–5.

[60] T.-H. Kim and T.-J. Lee, "Throughput enhancement of macro and femto networks by frequency reuse and pilot sensing," in *IEEE International Performance, Computing and Communications Conference (IPCCC)*, 2008, pp. 390–394.

[61] L. Zhang, L. Yang, and T. Yang, "Cognitive interference management for LTE-A femtocells with distributed carrier selection," in *IEEE Vehicular Technology Conference*, 2010, pp. 1–5.

[62] O. Tickoo and B. Sikdar, "Modeling queueing and channel access delay in unsaturated IEEE 802.11 random access MAC based wireless networks," *IEEE/ACM Transactions on Networking*, vol. 16, no. 4, pp. 878–891, 2008.

[63] X. Bao, X. Zhu, T. Song, and Y. Ou, "Protocol design and capacity analysis in hybrid network of visible light communication and OFDMA systems," *IEEE Transactions on Vehicular Technology*, vol. 63, no. 4, pp. 1770–1778, 2014.

[64] X. Li, R. Zhang, and L. Hanzo, "Cooperative load balancing in hybrid visible light communications and WiFi," *IEEE Transactions on Communications*, vol. 63, no. 4, pp. 1319–1329, 2015.

[65] T. D. Little and M. Rahaim, "Network topologies for mixed RF-VLC HetNets," in *IEEE Summer Topicals Meeting Series (SUM)*, 2015, pp. 163–164.

[66] D. A. Basnayaka and H. Haas, "Hybrid RF and VLC systems: Improving user data rate performance of VLC systems," in *IEEE Vehicular Technology Conference*, 2015, pp. 1–5.

[67] W. Guo, Q. Li, H.-y. Yu, and J.-h. Liu, "A parallel transmission MAC protocol in hybrid VLC-RF network," *Journal of Communications*, vol. 10, no. 1, 2015.

[68] S. Shao, A. Khreishah, M. Ayyash, M. B. Rahaim, H. Elgala, V. Jungnickel, D. Schulz, and T. D. Little, "Design and analysis of a visible-light-communication enhanced WiFi system," *IEEE/OSA Journal of Optical Communications and Networking*, vol. 7, no. 10, 2015.

[69] T.-h. Hsu, "Optimization on color characteristics for LED lighting system," *National Central University, Taiwan, Master thesis*, p. 51, 2005.

[70] I. Din and H. Kim, "Energy-efficient brightness control and data transmission for visible light communication," *IEEE Photonics Technology Letters*, vol. 26, no. 8, pp. 781–784, 2014.

[71] I. Cisco, "Cisco service provider Wi-Fi: A platform for business innovation and revenue generation," *CISCO White paper*, 2015.

[72] J. Zhang, X. Zhang, and G. Wu, "Dancing with light: Predictive in-frame rate selection," in *IEEE International Conference on Computer Communications (INFOCOM)*, 2015, pp. 1–9.

[73] K.-D. Langer, J. Hilt, D. Shulz, F. Lassak, F. Hartlieb, C. Kottke, L. Grobe, V. Jungnickel, and A. Paraskevopoulos, "Optoelectronics & communications rate-adaptive visible light communication at 500Mb/s arrives at plug and play," *SPIE Newsroom*, vol. 14, 2013.

[74] P. Gupta and P. R. Kumar, "The capacity of wireless networks," *IEEE Transactions on Information Theory*, vol. 46, no. 2, pp. 388–404, 2000.

[75] R. Diestel, "Graph theory," *Graduate Texts in Math*, 2005.

[76] T. M. Cover and J. A. Thomas, *Elements of information theory*. Hoboken, NJ: John Wiley & Sons, 2012.

[77] I. Stefan and H. Haas, "Hybrid visible light and radio frequency communication systems," in *IEEE Vehicular Technology Conference*, 2014, pp. 1–5.

[78] D. Bertsimas and J. N. Tsitsiklis, *Introduction to linear optimization*. Belmont, MA: Athena Scientific, 1997, vol. 6.

[79] J. Desrosiers and M. E. Lübbecke, *A primer in column generation*. New York: Springer, 2005.

[80] Y. Shi, Y. T. Hou, J. Liu, and S. Kompella, "Bridging the gap between protocol and physical models for wireless networks," *IEEE Transactions on Mobile Computing*, vol. 12, no. 7, pp. 1404–1416, 2013.

[81] D. Tronghop, J. Hwang, S. Jung, Y. Shin, and M. Yoo, "Modeling and analysis of the wireless channel formed by LED angle in visible light communication," in *IEEE International Conference on Information Networking (ICOIN)*, 2012, pp. 354–357.

[82] Y. Li, L. Wang, J. Ning, K. Pelechrinis, S. V. Krishnamurthy, and Z. Xu, "VICO: A framework for configuring indoor visible light communication networks," in *IEEE International Conference on Mobile Adhoc and Sensor Systems (MASS)*, 2012, pp. 136–144.

[83] B. Nakhkoob, M. Bilgi, M. Yuksel, and M. Hella, "Multi-transceiver optical wireless spherical structures for MANETs," *IEEE Journal on Selected Areas in Communications*, vol. 27, no. 9, pp. 1612–1622, 2009.

[84] Y. Shi and Y. T. Hou, "Optimal power control for multi-hop software defined radio networks," in *IEEE International Conference on Computer Communications (INFOCOM)*, 2007, pp. 1694–1702.

[85] Y. Tao, X. Liang, J. Wang, and C. Zhao, "Scheduling for indoor visible light communication based on graph theory," *OSA Optics Express*, vol. 23, no. 3, pp. 2737–2752, 2015.

[86] I. ILOG, "CPLEX optimizer, version 12.6.1," http://www-03.ibm.com/software/products/de/ibmilogcpleoptistud/, [Online; accessed 1-May-2014].

[87] D. Wu, Z. Ghassemlooy, W.-D. Zhong, and C. Chen, "Cellular indoor OWC systems with an optimal lambertian order and a handover algorithm," in *IEEE International Symposium on Telecommunications (IST)*, 2014, pp. 777–782.

[88] M. Rahaim and T. D. Little, "SINR analysis and cell zooming with constant illumination for indoor VLC networks," in *IEEE International Workshop on Optical Wireless Communications (IWOW)*, 2013, pp. 20–24.

[89] H. Sugiyama, S. Haruyama, and M. Nakagawa, "Brightness control methods for illumination and visible-light communication systems," in *IEEE International Conference on Wireless and Mobile Communications (ICWMC)*, 2007, pp. 78–78.

[90] S. Shao, A. Khreishah, and H. Elgala, "Pixelated VLC-backscattering for self-charging indoor IoT devices," *IEEE Photonics Technology Letters*, vol. 29, no. 2, pp. 177–180, 2017.

[91] J. Armstrong, "Optical domain digital-to-analog converter for visible light communications using led arrays [invited]," *OSA Photonics Research*, vol. 1, no. 2, pp. 92–95, 2013.

[92] K. Y. Ahn, "Method of fabricating integrated circuit wiring with low RC time delay," Mar. 14 2000, US Patent 6,037,248.

[93] S. Hranilovic, *Wireless optical communication systems*. New York: Springer, 2006.

[94] "Lux to Watt/square centimeter Converion," http://www.endmemo.com/sconvert/luxwatt_squarecentimeter.php, [Online; accessed 1-April-2015].

[95] Shawn, "Top 20 most efficient solar panels," http://sroeco.com/solar/top-20-efficient-solar-panels-on-the-market/, [Online; accessed 1-April-2015].

[96] A. Lundvall, F. Nikolajeff, and T. Lindström, "High performing micromachined retroreflector," *OSA Optics express*, 2003.

[97] Reflect-All, https://reflect-all.com/, [Online; accessed 2-May-2017].

[98] D. A. Arnold, "Method of calculating retroreflector-array transfer functions," *SAO Special Report*, vol. 382, 1979.

[99] Thorlabs, https://www.thorlabs.com/newgrouppage9.cfm?objectgroup_id=145, [Online; accessed 1-April-2017].

[100] Rfractive index database, https://refractiveindex.info/?shelf=glass&book=BK7&page=SCHOTT, [Online; accessed 2-May-2017].

[101] Hamamatsu, https://www.hamamatsu.com/resources/pdf/ssd/s6801_etc_kpin1046e.pdf, [Online; accessed 1-April-2017].

[102] B. Alsinglawi, M. Elkhodr, Q. V. Nguyen, U. Gunawardana, A. Maeder, and S. Simoff, "RFID localisation for Internet of Things smart homes: A survey," *International Journal of Computer Networks and Communications (IJCNC)*, vol. 9, no. 1, 2017.

[103] M. Kotaru, K. Joshi, D. Bharadia, and S. Katti, "Spotfi: Decimeter level localization using wifi," in *ACM SIGCOMM*, 2015.

[104] D. Vasisht, S. Kumar, and D. Katabi, "Decimeter-Level Localization with a Single WiFi Access Point," in *USENIX Symposium on Networked Systems Design and Implementation (NSDI)*, 2016.

[105] Apple Inc., https://developer.apple.com/ibeacon/, [Online; accessed 4-May-2017].

[106] Decawave, https://www.decawave.com/, [Online; accessed 4-May-2017].